Stony Brook University

Strong Field Coherent Control

A Dissertation Presented

by

Carlos Alberto Trallero

to

The Graduate School

in Partial Fulfillment of the Requirements

for the Degree of

Doctor of Philosophy

in

Physics

Stony Brook University

August 2007

Stony Brook University

The Graduate School

Carlos Alberto Trallero

We, the dissertation committee for the above candidate for the Doctor of Philosophy degree, hereby recommend acceptance of this dissertation.

Thomas Weinacht
Professor, Department of Physics and Astronomy

Harold Metcalf
Professor, Department of Physics and Astronomy

Philip B. Allen
Professor, Department of Physics and Astronomy

George N. Gibson
Professor, University of Connecticut

This dissertation is accepted by the Graduate School.

Lawrence Martin
Dean of the Graduate School

Abstract of the Dissertation

Strong Field Coherent Control

by

Carlos Alberto Trallero

Doctor of Philosophy

in

Physics

Stony Brook University

2007

The work presented in this thesis is geared towards the understanding of coherent control in molecules and atoms in strong fields. The analysis is done by studying multiphoton transitions. We present a theoretical model that describes multiphoton transitions under strong fields. We show that in order to achieve population inversion a phase-matching condition between the laser and the atom needs to be satisfied. This phase matching condition shows that fields need to be tailored taking into account the presence of the dynamic stark shift (DSS) effect and compensating for it. These findings are corroborated by experimental results and simulations. Experimentally, we used a genetic algorithm (GA) to find pulse shapes that can efficiently excite atomic Na to the $4s$ state by means of a two photon absorption. The solutions found by the GA are used directly to integrate Schrödinger's equations for the amplitudes. The results of using this scheme ratify our theoretical model. We also map how the transition from the weak to the strong field limit occurs for two and three level systems in the presence of multiphoton transitions. Here, we show that the perturbative solutions are a particular case of our model and they are recovered in

the limit where the DSS and the depletion of the ground state can be neglected. Presented in this work is also a study of the response to a strong field of an ensemble of atoms. Numerical simulations and experiments agree in showing a threshold-like behaviour in the response of the ensemble with the single atom excitation. This behaviour drastically differs from the single atom response. Finally, this work shows that the use of learning algorithms is a very plausible way in gaining detailed physical insight of the mechanisms present behind the coherent control of quantum systems.

To all my family, and to the memory of the ones who saw me leave but never come back.

Contents

List of Figures

List of Tables

Acknowledgements

Fortunately for me, I have to thank several people for making this thesis possible and this section is very large. Hopefully I'll remember all of them, from the ones that make my daily life better, to the ones that crossed my path for a brief moment but without whom this thesis wouldn't be possible.

I really need to thank my advisor Tom for all these years. Me being "wanna be" theoretician at the time, I still don't know how he decided to take me as a student, when I didn't even know what a grating was and my experimental expertise was zero at best. In any case, thanks for bearing with me during this transition and your ever forgiveness of my "Cuban" o'clock time. Thanks also for the never dying enthusiasm that made all the hours, drawbacks, and disappointments look minuscule.

My family played a very special role in this thesis. From my closest one in Cuba, to the ones scattered all over. Without their support through good and bad times this wouldn't be possible. Since I know how important this thesis is to all of them, I would like to mention them here: my mother Grisel and father Carlos, Carlos M., Juan, Digna, Andres, Carmen, Teresita, Loly, Juan A, Tony, Angela, Ma. del Carmen, Alex, Russland, Tony A., Ma. Elena, Fina, Ginette, Enrique, Rene, Alicia, Roxana, Nelson, Vickie, Victoria, Miguel Angel, and last, but definitely not least Vina.

A big thanks to the people in the lab. David Cardoza, for introducing me to Tom and the ultrafast world, and from whom I learned a lot in the lab. Sarah Nichols, for keeping things in order all the time, the keys to my office, and remind me so many times of the group meeting time. Florian Langhojer, with whom I spent several late nights "FROGing" pulses. Brendan Keller motivated me a lot by being such a dedicated undergraduate student. Dan Flickinger was crucial in the realization of Chapter 5. Steve Clow really took over in the atomic experiments and some of the results presented in Chapter 6 were done together with him. Brett Pearson, besides a great company, gave us a lot of valuable comments for the results presented in Chapter 5 and a great part of Chpater 7 was done with his collaboration. Thanks also to Jay, Coco, Dominik, and Evan for making my working environment simply more

enjoyable.

The AMO group at Stony Brook has been a constant source of inspiration. From how they interact to each other, to how they always seem to find time to talk about physics, regardless of titles, it is a group of which I'm proud to be a part of. Thanks to Harold Metcalf, Thomas Bergeman, Dominik Schneble, and all the graduate students in the AMO group for such a nice environment. A particular thanks to Peter Koch, who really made me decide to try experimental physics after being one of his students in the graduate lab class.

There is also a special group of people who made it possible for me

to here in the first place. Jacobus Verbaarschot whom I met in Brazil and mentioned the crazy idea, of a Cuban student going to a U.S. university for a Ph.D., Peter Stephens who was the graduate director at the time and supported me coming here despite all the obstacles, and Lazlo Mihaly and his daughter who took my application from Havana to Stony Brook. Finally, ff there is a person I have to thank for being in Stony Brook, it is Pat Peiliker, she really took the task of making possible my presence here and has helped me enormously through these years.

Chapter 1

Introduction and overview

Coherent control of quantum systems is currently a very active area of research in physics and chemistry [3–9]. It is not a surprise then that huge efforts have been carried out in the Atomic, Molecular, and Optical (AMO) community to understand the physics and chemistry behind these ideas. Although the theory behind the interaction of quantum systems with classical fields is well known, it differs with the idea of coherent control. In the case of coherent fields interacting with quantum systems interference plays a big role and this leads to a more detailed control of the interaction and therefore of the final state. It was only after the invention of coherent light sources, like the laser, that these kind of processes became a reality.

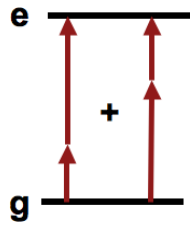

Figure 1.1: Interference between two quantum excitation paths. By changing the relative phase between the photons in each path, the total excitation to the excited state e can be controlled.

A coherent process can be succinctly summarized as the transfer of coherence from a source (in our case an optical field) to atoms or molecules. Control can be achieved by interference between different possible paths for the excitation of the quantum system. In Figure 1.1 for example, by controlling the relative phase between the photons, both paths will "interfere" thus creating a net population transfer to the excited state **e**. This net population transfer or excitation is an example of what we understand by control. Practically, this requires that the phase of the control field and the target be defined. When fields are weak, this interference can be understood in terms of two independent entities that have no effect on each other, but that when combined, give a totally new result. This *weak field limit* is often easy to deal with

and theoretical and experimental approaches can give a lot of insight [10–12]. One down side in this case is that if we want to invert the population to some excited state, the amount of control that can be obtained is not large, i.e. the atoms or molecules can not be 100% excited. One obvious solution is to increase the intensity of the control optical fields. However, for strong fields the quantum state of the target (molecule or atom) changes or is "dressed" by the field [13]. We can expect that phenomena like the AC Stark shift [14] will have a great impact in this *strong field limit*. This fact needs to be taken into account in order to describe how control occurs in quantum systems. It is in this context that this thesis is developed. We want to know if total control can be obtained in the presence of strong fields. and if possible, we then need to understand the underlying physics.

In this thesis we will deal mainly with one class of coherent interaction between atoms or molecules and fields. These are the multiphoton transitions. As the name indicates, an atom can absorb more than one photon. Multiphoton transitions have been extensively studied [15]. Experiments and theory dealt mainly with sequential transitions, where there is a ladder of states and the electronic population gets excited through intermediate, close to resonance, states. Each of these steps requires that the standard selection rule for E1 dipole transitions be satisfied. There is another kind of multiphoton transitions in which two photons are absorbed at the same time and there is no need for intermediate resonances. This is a very exciting excitation process due to the fact that, by means of a multiphoton transition, with the same experimental setup we can target new states that are not accessible when using single photon transitions.

This particular kind of multiphoton transition has been studied particularly in the weak field regime [9–12] and in the case where there are no intermediate resonances, that is, the two photons will get absorbed at the same time. The case where there is an intermediate resonance has also been a topic of interest for the case of two photon absorption [16], and very recently for three photon absorption [17]. Also, some attempts to develop an understanding in the strong field regime have been made [18–20]. One thing that distinguishes the interaction with strong fields is the presence of Stark shifts. These are known to play an important role in the interaction of atoms and molecules with intense lasers [7, 21–30]. However, there is no to our knowledge, a clear "recipe" for how to take into account the Stark shifts for inverting the population in the presence of multiphoton transitions with pulsed, ultrafast, and strong fields. We found that the presence of Stark shifts is of great importance in the understanding of multiphoton transitions. Furthermore, without dynamically compensating for these shifts, population inversion can not be achieved.

Figure 1.2 depicts the quantum interference for a multiphoton transition in the presence of strong fields. Here we need to take into account, not only the interference between the different quantum paths, but also how the quantum system itself is modified by the field. Another degree of complication is added by the fact that the control fields are time dependent and the "distortion" of the quantum levels occurs dynamically. Therefore, in order to achieve an inversion, a constructive interference of the different quantum paths needs to be preserved in time.

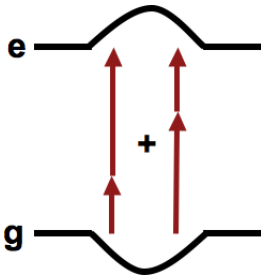

Figure 1.2: Interference between two quantum excitation paths in the presence of strong fields. Here, not only the interference between different paths needs to be considered, but also the "distortion" of the quantum levels by the field.

This thesis is composed of eight chapters and two appendices. The first chapter is this introduction and the final one are the conclusions. In Chapter 2 we show the details of the different experimental setups and detection schemes.

Chapter 3 introduces the theory of multiphoton processes for two and three photon absorption in the weak field limit. In this chapter we also develop a theoretical model for the description of multiphoton transitions with strong fields in the presence of Stark shifts [31]. We also show how the perturbative results obtained in [10–12] are a particular case of our model when the limit to weak fields is taken [32]. In the chapter it is also shown that an intuitive time dependent atom-field phase matching can be used as the condition for efficient (i.e., complete) population transfer [33]. The case of resonance mediated three photon transitions and how they can be described with the aid of our model can also be found here [32]. Finally, we give some details of the numerical methods used.

In Chapter 4 we present the experimental and simulation results for the theoretical model presented in Chapter 3. These results are aimed to prove that the atom-field phase matching picture for describing multiphoton transitions is indeed a valid one [33]. Furthermore, we are able to map how the transition happens when going from the weak to the strong field limit and describe the experimental data using our model [32].

Chapter 5 describes how coherent control of an ensemble of atoms departs from that of a single atom. In this chapter we obtain the polarization for a medium that is two photon absorbent, in the presence of time dependent Stark shifts. Experiments are carried out to show how control, targeted towards

single atoms, can lead to a coherent response of a large ensemble of atoms. The experimental results are explained with the aid of a model that takes into account the response of a single atom to a strong field by means of a multiphoton transition, and how this response can "propagate" to the ensemble in a coherent way [34].

In Chapter 6 we use the three level multiphoton model to study how the transition from weak to strong fields happens in the case of a resonance mediated three photon transition. We also show that efficient control of the population, in a three level system, in the presence of multiphoton transitions, is possible.

Finally, in Chapter 7 we present some of the on-going and future research that has not completely finished at the moment of writing this thesis. These topics include, the use of local control theory [35–38] to understand the mechanisms for control in three level systems, and the use of the phase matching theory for multiphoton transitions to do pulse shaping spectroscopy of molecular dynamics in the presence of strong fields.

We give our final remarks in Chapter 8 followed by two appendices.

Chapter 2

Experimental Apparatus

In this chapter we describe the experimental apparatus used in our experiments. There are two experimental setups used in this thesis. The one that was used most is for single atom experiments in atomic Sodium (Na). This setup, with slight modifications is also used to study the collective response of an ensemble of atoms. The second apparatus is a vacuum chamber with an effusive molecular sample and a time of flight mass spectrometer for detecting molecular ions. Details of each experiment will be given in different sections of this chapter. A general diagram used for all of the experiments is depicted in Figure 2.1.

The basic idea is to shape femtosecond pulses coming out of the laser system and send different pulse shapes to different experiments. The signal produced by the different detectors is then sent to a computer and digitalized for further analysis. The main components in the experiments are, the laser system, the Pulse Shaper (PS), and the Personal Computer (PC) that controls the PS and hosts a digital oscilloscope that serves as digitizer of the signals sent by the different detectors. The PC is also equipped with a Genetic Algorithm that allows for close-loop feedback experiments. The difference between experiments starts after the PS. For the single atom fluorescence measurements we use a spatial filtering system after the PS that is not present when we measure the response of an ensemble of atoms. These two experiments also differ in the detection scheme (see Sections 2.4 and 2.5). In the molecular experiments, the beam coming out of the pulse is simply focused into the interaction region of a molecular chamber.

Much of the detail for the laser generation and characterization used in the lab will be omitted since it was the core of the M. Sc. thesis of P. H. Nürnberger [39]. Also, the molecular setup used for the last section of Chapter 7 will be described in a succint manner as it was described in detail in previous theses by P. H. Nürnberger [39] and D.C. Cardoza [40]. Most of the details of the

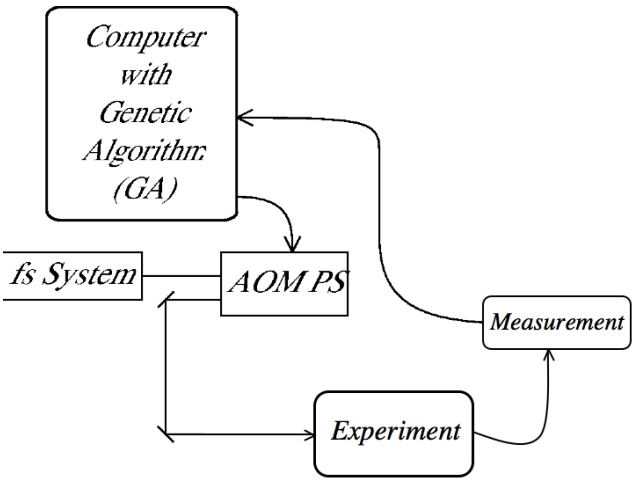

Figure 2.1: General setup used in our experiments.

pulse shaping and Genetic Algorithm techniques can also be found in [40]. Finally, most of the details of the cross correlation mentioned in section 2.5 can also be found in D. A. Flickinger's thesis [41].

2.1 Generation and measurement of strong, ultrafast laser pulses

The heart of our experimental apparatus consists of a laser system that employes the Kerr lens effect, modelocked Titanium:Sapphire oscillator (KM Labs model TS) pumped by a Continuous Wave (CW) laser (Verdi V6 Vanadate laser) [39]. The oscillator seeds a Titanium:Sapphire, chirped-pulse amplified ultrafast laser amplifier (KM Labs HAP-AMP), in a multi-pass configuration [42]. It is capable of producing 30 fs pulses at a repetition rate of 1 kHz. The pulse energies are typically $\sim$ 1 mJ. Figure 2.2 shows the intensity and phase as a function of time for a pulse from our amplifier. It should be noted that although the phase shows quite some structure, the change during the duration of the pulse is less than 1 radian. Pulses coming out of our amplifier or the PS are characterized using a second-harmonic generation frequency resolved optical gating (SHG FROG) [39, 43].

SHG FROG, or simply FROG, allows us to measure the amplitude and phase of the pulses found in the lab.

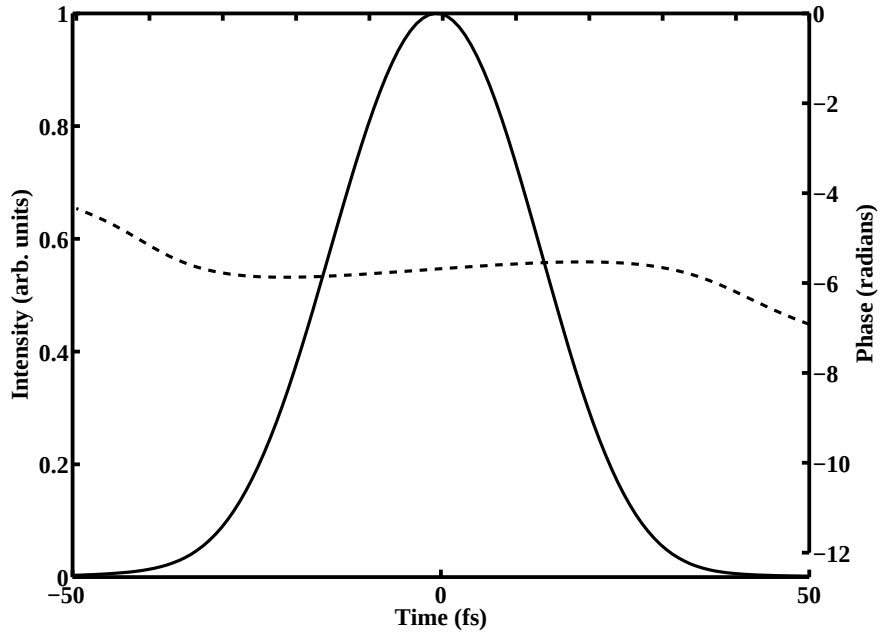

Figure 2.2: Typical $I(t)$ (solid) and $\varphi(t)$ (dashed) from our amplifier. The pulse duration is 30fs FWHM.

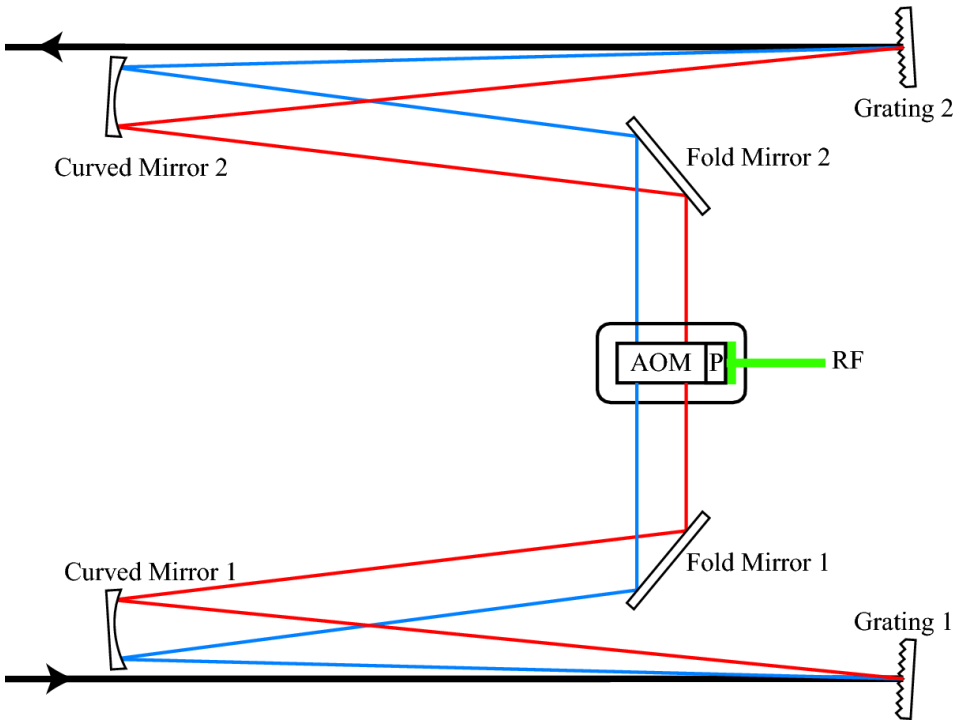

Figure 2.3: Diagram of pulse shaper.

2.2 Pulse shaping

The femtosecond pulses generated by the amplifier are faster, by some orders of magnitude, than any electronics available. It is therefore impossible to shape the laser in real time. To get around this, we use the method developed by Weiner [44].

Figure 2.3 shows a schematic diagram of the pulse shaper used in our lab. The ultrafast laser pulses are dispersed by diffraction Grating 1, causing each color in our spectrum to be mapped to a particular angle. The dispersed light is then collimated by Curved Mirror 1. This collimates the dispersed light, thereby mapping each color in the spectrum to a particular point in space, at the focus or Fourier plane. At the Fourier plane, we place a programmable mask or Spatial Light Modulator (SLM). There is a variety of these devices. In our case, an acousto-optic modulator (AOM) is the method of choice [45]. SLMs allow us to manipulate the phase and amplitude of adjacent frequency components. In an AOM, this mask is created by an acoustic wave in the crystal. The acoustic wave is generated by a piezoelectric component, at one end of the AOM crystal, which is driven by a radio frequency (RF) voltage. If

we have the incoming pulse in frequency, $E(\omega)$, then after the AOM, we have

$$E(\omega)_{shaped} = E(\omega)e^{i\phi(\omega)}M(\omega) \tag{2.1}$$

Where $M(\omega)$ is the frequency dependent transfer function, or *mask*, that represents the AOM, and it's phase and amplitude can be programmed. We manipulate $\varphi(\omega)$ by manipulating the temporal phase of the acoustic wave in the AOM crystal. The AOM behaves like a transmission grating, where the grooves are the compressions and rarefactions of the sound wave in the AOM crystal. By manipulating the phase of the acoustic wave about the central RF frequency, the different optical frequency components of the pulse will see different phases of the acoustic wave, thereby causing the colors to undergo slightly different dispersion. This causes the phase relationship between the different optical frequency components to change. The AOM also allows us to manipulate the amplitude of the spectral components by changing the amplitude of the acoustic wave. The light is then re-focused using Curved Mirror 2 onto Grating 2, where the frequency components are recombined. The result is a temporally shaped laser pulse.

Figure 2.4 shows both the intensity $I(t)$ and phase $\phi(t)$ from a Frequency Resolved Optical Gating (FROG) reconstruction for an unshaped pulse from the AOM pulse shaper.

The AOM crystal used in our lab is designed to work at a RF of 150MHz. At this frequency, the diffraction efficiency of the AOM is $\sim$ 65% and the overall efficiency of the pulse shaper is of $\sim$ 40%. We can manipulate the phase of the acoustic wave about this central frequency by using an arbitrary waveform generator. The waveforms are generated using a single waveform generator board (GAGE Compugen 11G), which can generate points at a rate of 1 GHz. This board allow us to create a 150 MHz waveform. With this method, we program the complete waveform as a function of time which can be translated to space since we know the speed of sound in the AOM. With this technique we are able to have pulses with a high degree of fidelity as well as a larger phase difference across the pulse shaper.

2.3 Closed loop feedback with learning algorithms

The ideal scenario in the coherent control of quantum systems is to know the total Hamiltonian and design a field that takes the system to the desired state. Control can be, for example, to excite an atom to a given level, or to control the fragmentation yield of a molecule. Unfortunately, the complete

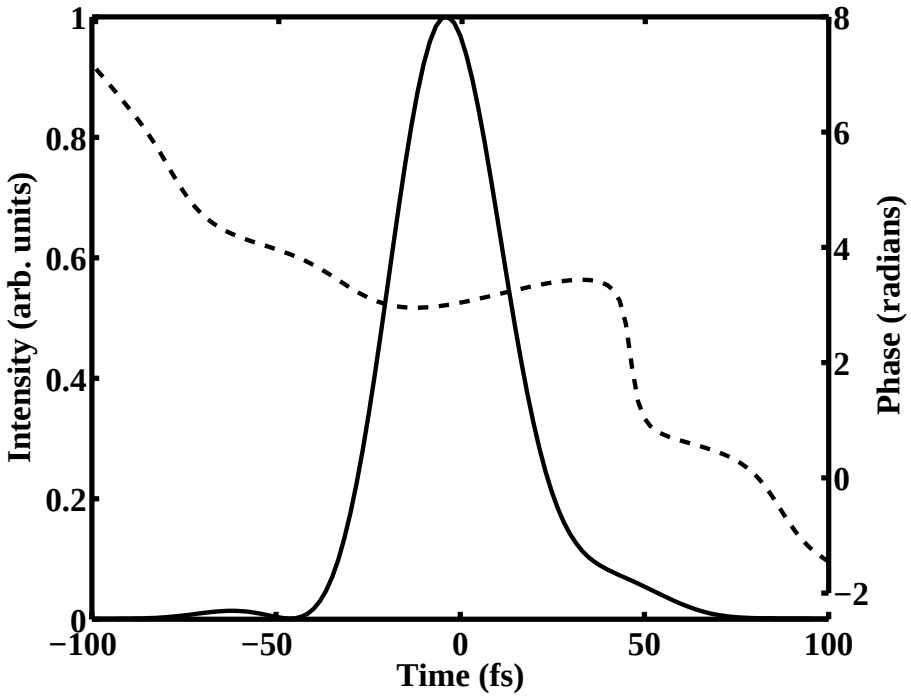

Figure 2.4: $I(t)$ and phase for an unshaped pulse from our pulse shaper.

Hamiltonian is rarely known, particularly in molecules. But even in simple atoms, where a lot of information exists about the different lines (lifetimes, Einstein coefficients, etc), it is extremely hard to build pulse shapes from the ground up that target a desired process. One solution to this problem is to use a closed-loop feedback technique. The general idea in this scheme is to try a pulse shape and measure how well it does in controlling the particular system. Then, repeat the process until reaching the maximum control attainable. At the end of this iteration, we have an electric field (or fields) that give us the desired final state.

Closed-loop schemes using pulse shaping are a great tool for control [46, 47]. However, it creates another daunting task. The number of parameters we can change, in order to achieve some experimental goal, are too many. To have an idea, for our pulse shaper, we have a maximum of 210 points in the AOM that can be independently adjusted and each one can change over some range of values. One solution to this problem is to use an algorithm capable of searching for extrema in a large space of variables. The genetic algorithm [48] (GA) is a very successful algorithm in such cases [8, 46, 47, 49, 50]. Details of our implementation of the GA can be found in [40, 49].

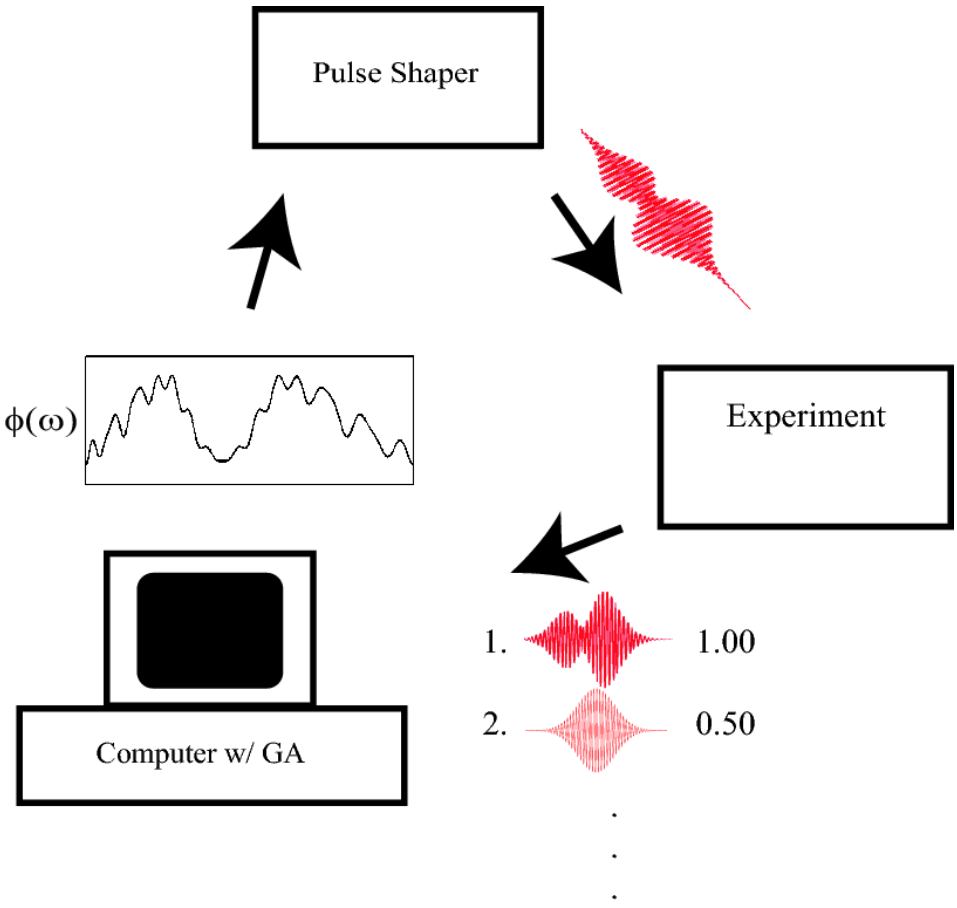

Figure 2.5: Diagram depicting the feedback system used to find optimal pulse shapes. A set of pulse shapes are generated in the computer and sent into the PS. The corresponding fields are then used in the particular experiment. The results of the interaction with the sample are measured and used as feedback. A GA is used to direct the closed-loop.

Figure 2.5 shows a diagram depicting the learning feedback loop. The GA is a global search algorithm that uses strategies adapted from natural selection. Following the language usually used in this context, the elements of the RF waveform that define a pulse shape are called *genes*, a pulse shape is called *individual*, and a group of individuals is called a *generation* The basic idea is to group pulse shapes into generations, modify these pulse shapes following operators that resemble the natural selection process, and create a new generation. This process is repeated until convergence is obtained. Typically, 50-100 generations are needed for convergence, which is defined as zero change in the overall fitness with generation, i.e., zero slope. One exception is when we use the forward generated light in Chapter 5. Here, more generations were

needed for a full convergence. Also, for the work described in Chapter 6, we found that the usual 20 genes were not enough to give the maximum control in a three level system. In this case, by using 40 genes, the fitness improved by $\sim 20\%$ with respect to when we used 20 genes. We can monitor the optimization process by looking at the average fitness of the best N pulse shapes from each generation. Figure 2.6 shows a typical fitness graph which is seen during the GA optimization process. It can be seen from Fig. 2.6 that the fitness

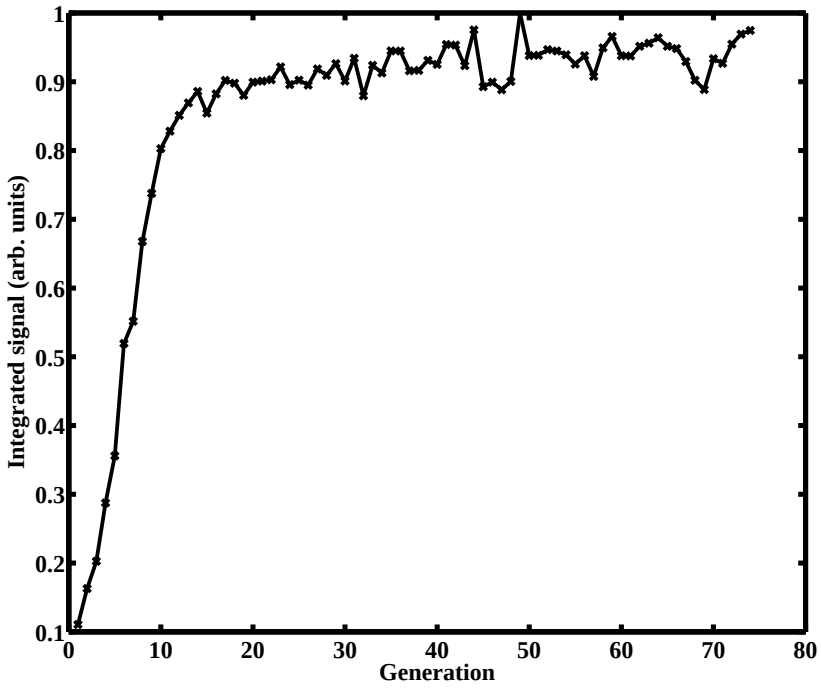

Figure 2.6: Average of the fitness over the best 8 individuals as a function of generation from a typical GA optimization.

initially starts out poor, but then undergoes rapid growth. At the end of the optimization, the fitness growth begins to slow down and eventually end. This zero slope in the fitness curve is the criteria for convergence to an optimal solution. It is at this point that we stop the optimization process. It should be noted that what we see in this graph is an average of the fitness generated by several pulses, and also, that the starting value of the fitness is not the one for an unshaped pulse since the initial generation has a normal distribution centered around an unshaped pulse (transform limited or zero phase).

In this thesis we will focus on understanding the solutions found by ou GA with the aid of detailed calculations. In this sense, the GA will be for most of

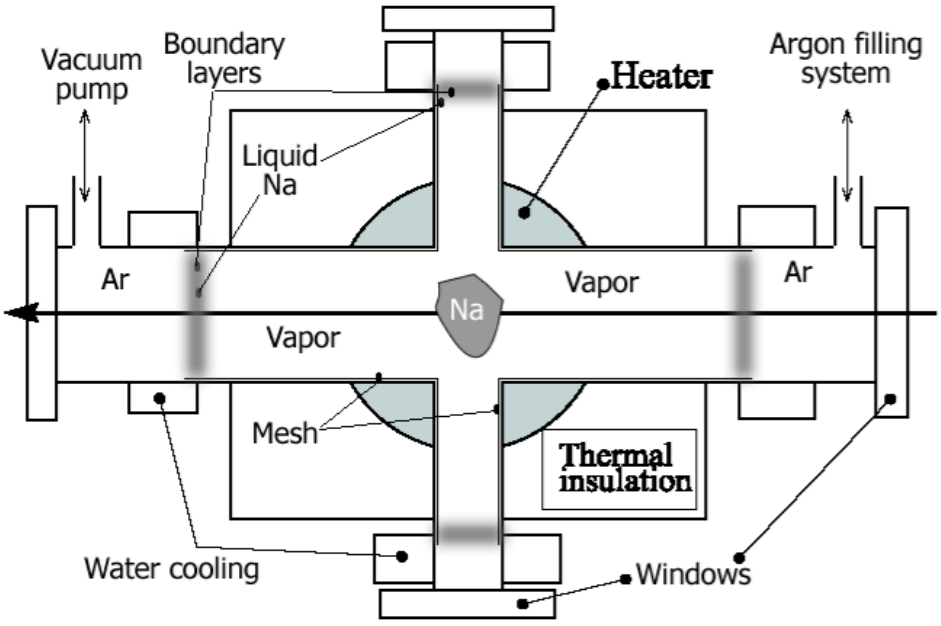

Figure 2.7: Diagram of the crossed heat pipe oven showing all of it's active elements.

this work, a tool, and the only thing we will assume is that it is able to find optimal solutions to the problem of finding pulse shapes for a given control goal [51]. We need to keep in mind that there can be more than one solution to the same control problem and the GA might be able to find any one of them.

2.4 Experimental setup for fluorescence measurements in atomic Sodium

All the atomic experiments presented in this thesis were carried out in Na (Sodium). Initially we designed an oven with a glass cell containing the Na, but after some time the Na reacted with the glass. After this, we built a heat pipe oven [52–54], using a crossed heat pipe design [55]. The heat pipe oven design allows us to have high pressures of Na while preventing the Na from reaching the optical windows. The cross design allows for fluorescence measurements at 90^o from the laser beam. A schematic design of the heat pipe is shown in Figure 2.7.

The crossed pipes were made out of stainless steel using standard ISO KF 50 and ISO KF 40 pipes welded as a cross. We used Argon as the inert gas in our oven and Aluminum water jackets for cooling. The center was heated

using high current electric disc heaters. The electric heaters were attached to the pipes by using a thermally conductive, electrically insulating cement (Aremco-Bond 568). We used a fine stainless steel mesh with holes $\sim 500\mu$m for returning the Na to the center of the heat pipe after condensing at the water cooled jackets. The way the heat pipe works is as follows. The high temperature (200 C to ∼400C in our case) in the center creates a vapor of Na atoms that tends to expand. As they reach the cooling elements, they encounter cool Ar atoms with whom they interchange kinetic energy until the condensation point. Once they condense, Na atoms get deposited in the steel mesh and by means of capillary effect they are transported to the center of the oven. This process is repeated in a steady state manner once thermal equilibrium is reached. Before filling the heat pipe with Ar, it is pumped to high vacuum ($\sim 10^{-7} Torr$) using a turbo pump. Once high vacuum is reached, the oven is isolated by closing a valve and Ar is injected into the system using a flow control valve. The working pressures of Ar we used are about 25mTorr. After being sealed, the heat pipe oven can be used for a few months. After this time, we have found that it needs to be re-pumped and refilled with Ar gas for optimum performance

We estimate the Na pressure inside the oven by using the solid phase vapor pressure empirical formula [56, 57],

$$\log_{10} P_v = 133.42927 - \frac{9302.868}{T} + 0.03114431T - 49.376 \log_{10} T \qquad (2.2)$$

where P_v is the vapor pressure in Torr, and T is the temperature in Kelvin. The temperature was controlled by changing the voltage in two variable AC power supplies which supplied the current (5A each) to the heating disks. The temperature was measured with heavy duty thermocouples.

As mentioned in the Introduction, we are interested in studying multiphoton transitions. In the case of atomic Sodium, with our laser, we can excite the atoms from the ground state $3s$ to the $4s$ state by means of two photon absorption (TPA). After the atoms are in the $4s$ (lifetime $\tau = 38ns$) they will decay to the $3p$ level (lifetime $\tau = 16ns$) [58] and from there back to the ground state. Since we are interested in the behaviour of atoms interacting with strong fields, it is important that the field have a uniform distribution of intensities in the interacting region. Because our laser has a Gaussian transverse spatial profile [59], we need to spatially filter the laser beam.

In Figure 2.8 we show the complete experimental setup for measuring the fluorescence of atoms excited to the $4s$ level (see Chapters 3 and 4). The laser beam coming out of the amplifier is sent into the PS. From there it goes through

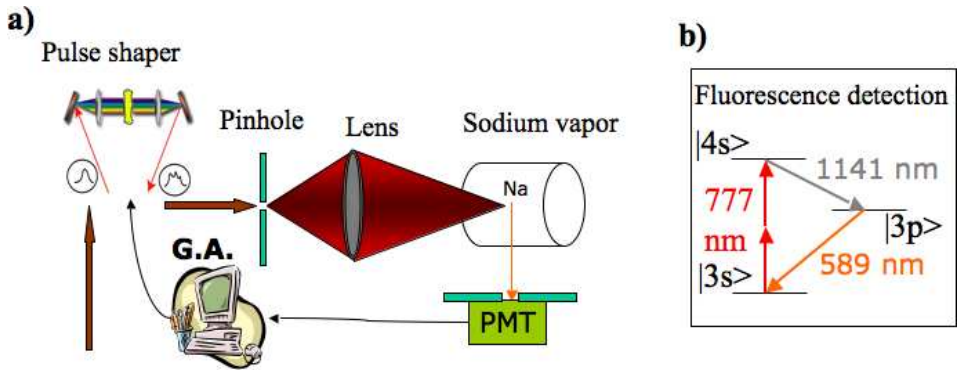

Figure 2.8: a) Diagram of the experimental setup for measuring fluorescence after exciting the atoms to the $4s$ level. b) Relevant energy levels for measuring the population in the $4s$ level.

the spatial filtering consisting of a lens and a pinhole. A subsequent lens images the filtered focus into the heat pipe and fluorescence is collected at 90^o degrees from the propagation direction. The fluorescence generated in the focus is also imaged into a small aperture in front of a photo multiplier tube (PMT). Finally the measured fluorescence is sent to a PC based oscilloscope. The pinhole allows only intensities that are 80% or larger than the peak intensity at the focus, $I > 0.8I_{max}$. The beam is focused onto the pinhole using a very long focal length lens ($f = 1m$). The pinhole however, will produce a diffraction pattern. To avoid this, we image the pinhole into the heat pipe oven using a $f = 0.6m$ focal length lens with a magnification of ~ 3.6. The reason for using magnification here is two-fold. The first is that by doing this we increase the interaction region and therefore the number of atoms from which we collect fluorescence. The second reason is that it allows us to measure with a CCD camera the actual mode of the laser. If the mode were small compared to the pixel size in the CCD camera, we would not be able to resolve any structure in the image. Figure 2.9 shows the two dimensional picture of the laser mode at the image of the pinhole.

Once the atoms are excited to the $4s$ state, they will decay to the $3p$, which is the only available state the $4s$ can decay to. The wavelength associated with this transition is $\lambda = 1141$nm. Ideally we would like to measure this transition, but detection technology for such wavelengths is very expensive. Instead we measure the two sodium D lines at $\lambda = 589$nm. For this we use an interference filter centered at 590nm with a width of 10nm FWHM, and an optical density for the 777nm pump laser greater than 10^4. After the filter, we place an aperture that limits the collection of fluorescence in the propagating direction to less than 1mm.

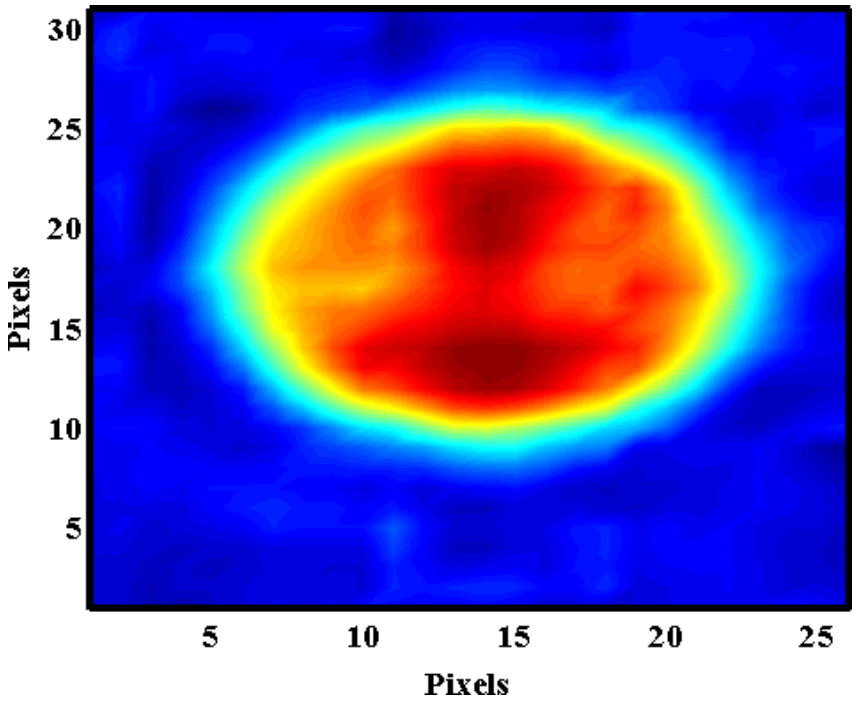

Figure 2.9: CCD picture of the laser mode at the interacting region.

The same setup is also used to study three level systems in Chapter 6. The only difference is that instead of targeting the $3s \rightarrow 4s$ transition we try to excite the atoms to the $7p$ level. The life time of this state is extremely long (of the order of μ seconds) and using a detection scheme using a direct transition from the $7p$ would be challenging. Instead, we make use of the fact that the $7p$ is energetically high and the density of states is large around it. Since we have a relatively high density of atoms in the heat pipe and there are some states within kT of the $7p$, collisions from this state to nearly lying levels are possible. The collision induced transitions to the $7s$, $6d$, and $6f$ are be a very strong relaxation mechanism for atoms in the $7p$ state. Furthermore, these collisional processes occur in a pico-second time scale, faster than any atomic decay. We measured the transitions $7s \rightarrow 3p$ and $6d \rightarrow 3p$ using a $\lambda = 470$nm interference filter. After the atoms relax to the $6f$ state, they can decay further to the $4d$ (500nm) or to the $3d$ (570nm). We measured these transitions as well using the appropiate interference filters. We also checked for ionization, by measuring transitions from higher states (like the $8s$) and we found no evidence of ionization. This is in agreement with previous measurements [29, 30] and the fact that we a small peak intensity relative to that required for ionization.

2.5 Experimental setup for stimulated emission measurements in atomic Sodium

In Chapter 5 we study stimulated emission processes that arise from collective atomic behaviour. The experimental setup in this case differs from the one used for measuring fluorescence in several ways. The first and most important difference is that instead of measuring the fluorescence at 90^o with respect to the incident laser beam, we measure the forward scattered light coming from the heat pipe in the same direction as the excitation beam. Figure 2.10 shows the experimental setup used to measure the forward light. Note that we use the infrared ($\lambda_0 \approx 780$ nm) pump laser beam for further measurements and that we also use a photodiode instead of a PMT. It should also be noted that we no longer use the pinhole since we want to target as many atoms as possible inside the laser beam and the mode obtained when using the pinhole is quite smaller than the unfiltered gaussian mode. Also, there is a large Rayleigh range [59] so that the intensity has small variations transverse to the propagation direction.

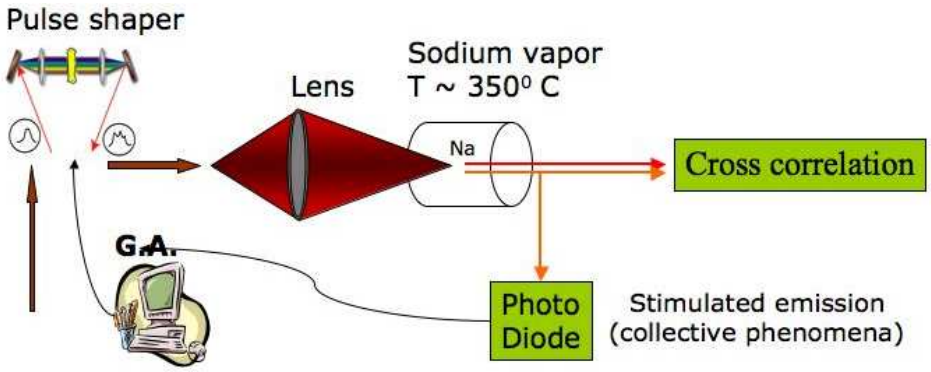

Figure 2.10: Experimental setup for the measurement of forward scattered 589nm light. Note that we also use the laser beam for further measurements.

In order to characterize the temporal properties of the forward scattered light at 589nm, we used a bichromatic prism pair interferometer [41, 60]. This allows us to spatially separate the pump and forward light beams and delay one respect to the other. Here we use it to cross-correlate the forward scattered light with the pump pulse. A sketch of this scheme can be seen in Figure 2.11.

In order to do this, both beams were first collimated. After this, both beams go into a prism so that we can spatially separate them. Once they are separated, each beam goes through a second prism to make both prisms parallel and then they are reflected from a mirror. We delay the infrared beam by using a delay stage with a stepper motor controlled by a computer. The

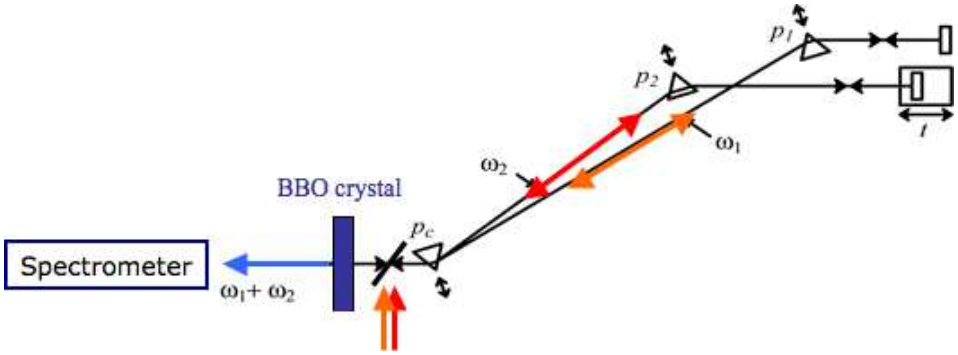

Figure 2.11: Setup for the cross correlation between the 780nm (red arrows) pump beam and the 589nm forward light (orange arrows).

beams are now retroflected but with a small tilt so that they are picked up by a mirror, after the first prism, and then focused into a Type I non-linear BBO crystal. This crystal is cut such that the non-linear polarization creates a third field with a frequency equal to the sum of the two incident frequencies [61]. In order for this to happen the two incident beams need to be overlapped in space and time inside the crystal. Therefore, as soon as one of the incoming pulses is delayed respect to the other the non-linear response of the crystal at this particular frequency stops. This sum frequency pulse is then sent to a spectrometer to record it's spectrum as function of delay between the input pulses. Since we are interested in the temporal characterization of the forward scattered light, a non-spectrally resolved measurement is enough. The use of a spectrometer is just for reassurance that the measured light is the one coming from the frequency sum of 780nm and 589nm.

2.6 Molecular setup

The last section of Chapter 7 makes use of an apparatus to study molecular fragmentation as a function of pulse shape. Details of this can be found in [39, 40], so we only offer a brief description. The pulses coming out of the pulse shaper are sent through a 150 mm lens and focused into an effusive molecular source underneath a time-of-flight mass spectrometer (TOFMS) inside a high vacuum chamber (pressure $\sim 1\times10^{-6}$ torr). It is here where the laser pulses dissociatively ionize molecules in the beam.

Figure 2.12 shows a diagram of the chamber used for the molecular experiments. Liquid samples are placed into a sample holder or reservoir. To ensure that the sample was not contaminated by air, we performed freeze-pump cycles by submerging the sample holder into liquid nitrogen. After the

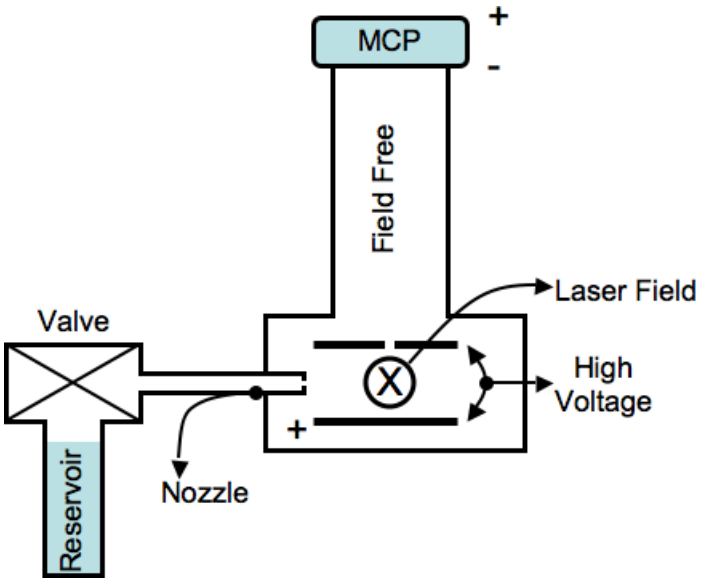

Figure 2.12: TOFMS working principle. The molecules get ionized in the interacting region and get accelerated upwards by a static electric field.

sample is frozen, the valve is open until the pressure in the chamber reaches $\sim 1.5 \times 10^{-5}$Torr, due to the boiling of the liquid sample as it reaches atmospheric temperature. Since the interaction region (where the laser field is present) is pumped constantly by a turbo pump, the pressure differential guarantees a constant flow of molecules into the interaction region. Molecules travel to the interaction region through a nozzle which has a very small hole at one end. This ensures an almost constant pressure in the chamber for a few hours, allowing us to carry out the experiments.

The laser field interacts with the molecules in the interaction region. The ionized fragments feel a force due to the electric field potential applied to the plates inside the chamber. This is a high voltage of 750 V since we need to give the molecules a considerable "kick". This force pushes the molecules through a hole in the upper plate. On the other side of the high voltage plates there is a field-free region. As the molecules fly through the vacuum, lighter molecules will arrive at the detector sooner. We can measure the time these molecules take to reach the detector, and this will give us their mass/charge ratio. The detector is a pair of microchannel plates (MCP) assembled in Chevron configuration. In order to have a field free region, we placed a grounded mesh at the bottom of the MCP. The signal generated by the detector is amplified by a pre-amplifier (Stanford Research Systems SIM914), and sent to the PC-based

oscilloscope. By using the digital oscilloscope, we can choose a particular fragment to analyze after the traces are taken.

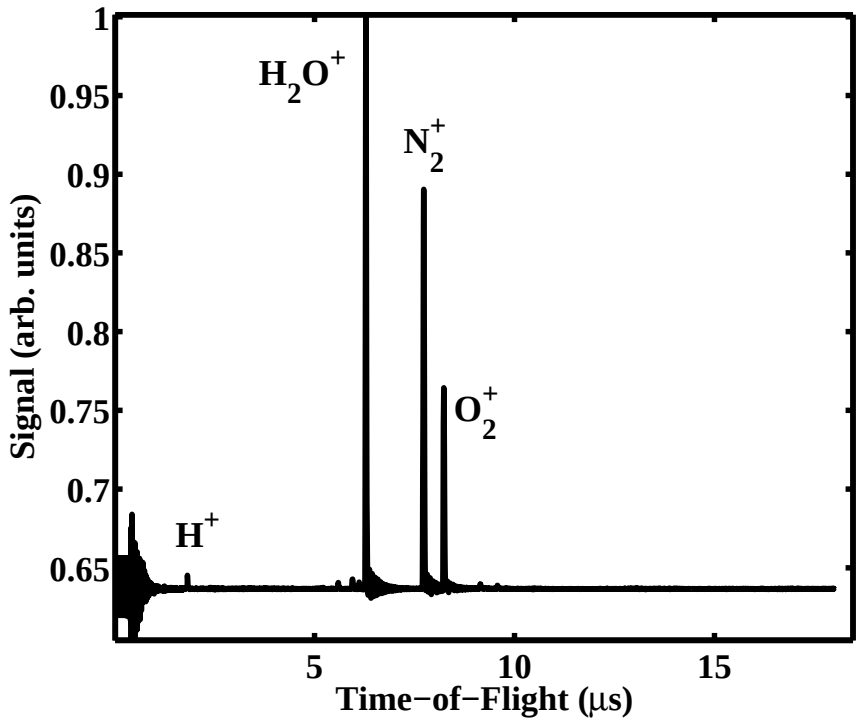

Figure 2.13: Example of a TOF spectrum for the background gas (no molecules in the manifold) of the chamber.

In Figure 2.13 we show a TOF spectrum taken with an "empty" chamber, that is, with no liquid sample in the reservoir. By using the mass of the elements most common in the atmosphere we can do an initial calibration of the TOF detector.

Chapter 3

Theoretical background and simulations details.

This chapter will lay down most of the theoretical framework that will be used throughout this thesis. Results found here will be used later on as a starting point for each specific topic.

3.1 Two level systems in electric fields revisited.

After the harmonic oscillator the interaction of an electric field with a dipole coupled two level system is probably the most studied problem in quantum mechanics. Due to the relevance it carries to problems discussed in this chapter, we will use it as an illustration of some techniques used later on for more sophisticated problems. In our case we will parametrize a pulsed laser field as,

$$\mathbf{E}(t) = \frac{1}{2}\varepsilon(t)e^{-\imath w_o t}\hat{\varepsilon} + c.c., \tag{3.1}$$

where

$$\varepsilon(t) = \varepsilon_0\sqrt{g(t)}e^{\imath\varphi(t)/2}, \tag{3.2}$$

ε_o is the field strength, w_o is the laser frequency, $\varphi(t)/2$ is the temporal phase of the field, $\hat{\varepsilon}$ is the polarization vector, $g(t)$ is the temporal intensity profile and c.c. stands for complex conjugate. The Hamiltonian for the atom plus field is

$$\hat{H}_{2l} = \hat{H}_{Atom} + \hat{H}_{AF}. \tag{3.3}$$

$\hat{H}_{Atom}$ represents the field-free atomic Hamiltonian, which satisfies

$$\hat{H}_{Atom}|i\rangle = \hbar\omega_i|i\rangle. \tag{3.4}$$

Here, $\hbar\omega_i$ are the energies of atomic levels represented by the state vectors $|i\rangle$. For convinience, the quasi-stationary part of these state vectors will be explicitly removed. The interaction Hamiltonian, $\hat{H}_{AF} = -\boldsymbol{\mu}\cdot\boldsymbol{E(t)}$, describes the atom-field coupling in the dipole approximation for atomic dipole-moment μ. For linearly polarized light, in the field-free basis set $\hat{H}_{AF}$ has matrix elements, $\mu_{ji} = \langle j|\mu E(t)|i\rangle$ and therefore,

$$\langle j|\hat{H}_{AF}|i\rangle = -\frac{\hbar}{2}\mu_{ji}\left(\varepsilon(t)e^{-\imath w_o t} + c.c\right). \tag{3.5}$$

This latter result is very convenient since it allows us to use the energy representation of the interaction Hamiltonian. By doing this, the only information we need in order to expand the wave function in terms of the atomic eigenvectors are the dipole moments μ_{ji} which are extensively tabulated [1]. The wave function of the system consisting of states $|i\rangle$ and $|j\rangle$ can be expressed as,

$$\Psi(t) = a_i(t)e^{-i\omega_i t}|i\rangle + a_j(t)e^{-i\omega_j t}|j\rangle \tag{3.6}$$

and it evolves according Schrödinger's equation,

$$i\hbar\frac{\partial}{\partial t}\Psi(t) = \hat{\mathbf{H}}_{\mathbf{2l}}(t)\Psi(t). \tag{3.7}$$

The problem can now be reduced to finding the amplitudes $a_i(t)$ and $a_j(t)$. This can be achieved using the orthogonality of the atomic eigenvectors and the fact that they are time independent. After the Rotating Wave Approximation (RWA see Appendix A.1), Eq. 3.7 for the amplitudes becomes,

$$i\hbar\dot{a}_i(t) = -\frac{1}{2}\mu_{ij}\varepsilon(t)e^{-i\Delta t}a_j(t) \tag{3.8}$$

$$i\hbar\dot{a}_j(t) = -\frac{1}{2}\mu_{ji}\varepsilon^*(t)e^{i\Delta t}a_i(t), \tag{3.9}$$

with $\Delta = \omega_o - \omega_j - \omega_i$ being the detuning of the laser respect to the field-free atomic transition. In matrix notation,

$$i\hbar\dot{\mathbf{a}} = \hat{\mathbf{H}}_{\mathbf{2l}}(t)\mathbf{a}, \quad \mathbf{a} = \begin{pmatrix} a_i \\ a_j \end{pmatrix}, \tag{3.10}$$

and $\hat{\mathbf{H}}_{\mathbf{2l}}(t)$ is the two-level dipole Hamiltonian,

$$\hat{\mathbf{H}}_{2l}(t) = \hbar \begin{pmatrix} 0 & -\frac{1}{2}\mu_{ij}\varepsilon(t)e^{-i\Delta t} \\ -\frac{1}{2}\mu_{ji}\varepsilon^*(t)e^{i\Delta t} & 0 \end{pmatrix}. \tag{3.11}$$

In order to have all the population transferred (at zero detuning, $\Delta = 0$) to the excited state the electric field needs to have enough energy. Fields that fulfill this condition are called π pulses (see Appendix A.2).

3.2 Two photons transitions in weak fields

The previous section dealt with the standard two level problem of an atom-field interaction. However, If the intensity of photons is high enough, there is a finite probability that two photons get absorbed at the same time. This is known as a multiphoton transition, and in this section we will treat them initially from a perturbative point of view. One remarkable feature of multiphoton transitions is that they don't obey electric dipole selection rules. This means that, for example, it is possible to couple two states with the same angular momentum. Another big difference with single photon transitions is that, as will be clear later on this chapter, the relative phase of the different frequencies in the field is extremely important. Although perturbation theory has inherent limitations, it is usually a very straightforward procedure and more importantly, it often gives lots of insight into the problem at hand. The theory of two photon absorption (TPA) for weak fields, was developed in a set of papers in Silberberg's group [10, 11]. In this section we outline these results. We first consider a two photon transition with no intermediate resonances. This is depicted in Figure 3.1. If the detuning of the intermediate states is large, they will not be populated by the pulse and the process can be described by a simple two level Hamiltonian. Under the RWA, a second order perturbation theory calculation yields the following result for the excited state amplitude $a_e(t)$ [10]:

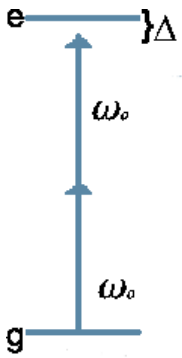

Figure 3.1: Non resonant two photon transition. Δ is the detuning from the bare state transition frequency.

$$a_e(t) = -\frac{1}{\hbar^2}\sum_m \mu_{em}\mu_{mg}\int_{-\infty}^{t}\int_{-\infty}^{t_1}\varepsilon(t_1)\varepsilon(t_2)\exp(-i\Delta_{em}t_1)\exp(-i\Delta_{mg}t_2)dt_1dt_2, \tag{3.12}$$

where $\Delta_{ij} = \omega_0 - \omega_{ij}$, $\omega_{ij} = \omega_i - \omega_j$, $\hbar\omega_i$ is the i state energy. μ_{ij} is the dipole moment as defined in the previous section. Performing the inner integral for large detuning of intermediate states, where $\exp(-i\Delta_{mg}t_2)$ varies rapidly compared to $\varepsilon(t_2)$, and taking the limit $t \to \infty$ [10], we obtain the two photon absorption (TPA) probability,

$$P_{g\to e} = \left|\frac{< e|\mu^2|g >}{\bar{\omega}\hbar^2}\right|^2 \left|\int_{-\infty}^{\infty}\varepsilon^2(t)\exp(-i\Delta t)dt\right|^2. \tag{3.13}$$

Here $\Delta = 2\omega_0 - \omega_{eg}$, $\hbar\omega_e$ and $\hbar\omega_g$ are the excited and ground states energies respectively, $\hbar\bar{\omega}$ is an appropriately weighted average energy of parity allowed far detuned intermediate states, and $< e|\mu^2|g >$ is the effective two photon coupling [11]. In the field parametrization above, $\varepsilon(t)$ is assumed to have a Gaussian intensity envelope. This result can easily be generalized to an Nth order process [11]. In the frequency domain, Eq.3.13 can be rewritten as,

$$\begin{aligned} P_{g\to e} &\propto \left|\int_{-\infty}^{\infty}\tilde{\varepsilon}(\omega_{eg}/2+\Omega)\tilde{\varepsilon}(\omega_{eg}/2-\Omega)d\Omega\right|^2 \\ &\propto \left|\int_{-\infty}^{\infty}A(\omega_{eg}/2+\Omega)A(\omega_{eg}/2-\Omega)\right. \\ &\times \left. e^{i\{\Phi(\omega_{eg}/2+\Omega)+\Phi(\omega_{eg}/2-\Omega)\}}d\Omega\right|^2, \end{aligned} \tag{3.14}$$

where $\tilde{\varepsilon}(\omega) = A(\omega)e^{\Phi(\omega)}$ is the Fourier transform of $\varepsilon(t)$. $A(\omega)$ and $\Phi(\omega)$ are the spectral amplitude and phase respectively. From this last expression, the transition probability can be interpreted in terms of a sum over photon pairs that fulfill the resonance condition $(\omega_{eg}/2+\Omega) + (\omega_{eg}/2-\Omega) = \omega_{eg}$. There are two important points to note regarding the weak field limit in the context of this work. First, the resonance condition governing the transition probability is static (time independent) and a frequency domain interpretation of control is natural. Second, while there are an infinite number of optimal pulse shapes (those with antisymmetric spectral phase), pulse shaping is not required to optimize population transfer. This last point can clearly be seen in Eq. 3.14 where the maximum possible value of the integral is achieved when the angular part of the integrand is zero. This is possible only when $\Phi(\omega_{eg}/2+\Omega) + \Phi(\omega_{eg}/2-\Omega) = 0$. By contrast, if there is an intermediate

resonance en route to the final state, then pulse shaping is required to optimize population transfer to the final state [16].

3.3 Two-photon transitions in the strong field limit

As already mentioned, a perturbative model has intrinsic limitations in terms of the situations it can describe. One such limitation is that the ground state is not depleted. This means that, using this formalism, we won't be able to describe population inversion. Also, since for strong fields the atomic structure changes, we can expect that for larger intensities the expansion breaks down. In this section we will derive a model for two-photon transitions driven by strong fields. The starting point is the same as in the simple single photon, two level case; the expansion of the atom's wave function in terms of the field-free eigenvectors,

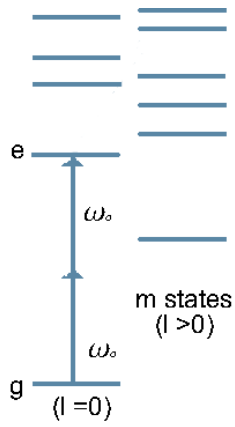

Figure 3.2: Non resonant two photon transition. Ground and excited states have $l = 0$. Off resonant m levels are p (l=1) states.

$$|\Psi(t)\rangle = \sum_{i=e,g,m} a_i(t) e^{-\imath\omega_i t} |i\rangle, \qquad (3.15)$$

where $a_i(t)$ are state amplitudes. The Schrödinger equation can be written as

$$\imath\hbar\dot{a}_j = \sum_{i=e,g,m} a_i(t) e^{-\imath\omega_{ij} t} \langle j|\hat{H}_{AF}|i\rangle, \qquad (3.16)$$

$j = e, g, \{m\}$ and $\omega_{ij} = \omega_i - \omega_j$. The sum over the $i = m$ contains all states that are one-photon coupled to either the i or j states.

Again, the m states are considered far off-resonance. Furthermore, these states have dipole allowed couplings to the ground and excited states, but since the detuning is so large, there will be no effective transfer to any of them. This was checked by integrating the Schrödinger equation for the most relevant levels (up to 16). For simplicity we will consider the ground and excited states to have zero angular momentum ($l = 0$). Thus, the m quantum

numbers refer to the p states ($l = 1$). Dividing the equations into ground ($j = g$), excited ($j = e$), and off-resonant ($j = m$) states,

$$
\begin{aligned}
i\hbar\dot{a}_g &= \sum_m a_m(t) e^{i\omega_{gm}t} \langle g|\hat{H}_{AF}|m\rangle && \text{(3.17a)}\\
i\hbar\dot{a}_e &= \sum_m a_m(t) e^{i\omega_{em}t} \langle e|\hat{H}_{AF}|m\rangle && \text{(3.17b)}\\
i\hbar\dot{a}_m &= a_g(t) e^{-i\omega_{gm}t} \langle m|\hat{H}_{AF}|g\rangle + \\
&\quad + a_e(t) e^{-i\omega_{em}t} \langle m|\hat{H}_{AF}|e\rangle. && \text{(3.17c)}
\end{aligned}
$$

The form of the above equations is convenient since we can now integrate explicitly for the m-state amplitudes. Since higher angular momentum states won't be significantly populated, the couplings from the intermediate states ($j = m$) to those other states are not relevant,

$$
\imath\hbar\dot{a}_m = a_g(t) e^{-\imath\omega_{gm}t} \langle m|\hat{H}_{AF}|g\rangle + a_e(t) e^{-\imath\omega_{em}t} \langle m|\hat{H}_{AF}|e\rangle. \tag{3.18}
$$

Adiabatic elimination of the rapidly oscillating, off-resonant amplitudes $a_m(t)$ involves formally integrating the equations for $\dot{a}_m$,

$$
\begin{aligned}
a_m(t) &= \frac{\imath}{2\hbar} \int_{-\infty}^{t} dt' \left[\mu_{me} a_e(t') e^{-\imath\omega_{em}t'} + \mu_{mg} a_g(t') e^{-\imath\omega_{gm}t'} \right] \\
&\times \left(\varepsilon_o \sqrt{g(t')} e^{\imath\varphi(t')/2} e^{-\imath\omega_0 t'} + c.c. \right). && \text{(3.19)}
\end{aligned}
$$

Eq. (3.19) can be integrated by parts using an approximation similar to the slowly varying envelope approximation. This approximation is justified since the field's envelope $\sqrt{g(t)}$ evolves slower ($\approx 30fs$) than the optical frequency ($2.5fs$). Formally, this *adiabatic* approximation reads,

$$
\frac{\partial}{\partial t}\varepsilon(t) \ll \left| \omega_{\{e,g\}i} - \omega_0 \right|. \tag{3.20}
$$

Following the above procedure we arrive to the following expression for the

intermediate state amplitudes,

$$a_m(t) = \frac{\mu_{mg}}{2\hbar} a_g(t) e^{\imath\omega_m t}\left[\frac{\varepsilon(t)e^{-i(\omega_g+\omega_0 t)}}{\omega_{mg}-\omega_0}+\frac{\varepsilon^*(t)e^{-i(\omega_g-\omega_0 t)}}{\omega_{mg}+\omega_0}\right]+ \frac{\mu_{me}}{2\hbar} a_e(t) e^{\imath\omega_m t}\left[\frac{\varepsilon(t)e^{-i(\omega_e+\omega_0 t)}}{\omega_{me}-\omega_0}+\frac{\varepsilon^*(t)e^{-i(\omega_e-\omega_0 t)}}{\omega_{me}+\omega_0}\right]. \quad (3.21)$$

After the integration above, we can substitute this expression for a_m into Eqs. 3.17a) and b),

$$i\hbar\dot{a}_g = \sum_m \left\{\frac{\mu_{mg}}{2\hbar} a_g(t)\left[\frac{\varepsilon(t)e^{-i\omega_0 t}}{\omega_{mg}-\omega_0}+\frac{\varepsilon^*(t)e^{i\omega_0 t}}{\omega_{mg}+\omega_0}\right]+ \frac{\mu_{me}}{2\hbar} a_e(t)\left[\frac{\varepsilon(t)e^{-i(\omega_e-\omega_g+\omega_0 t)}}{\omega_{me}-\omega_0}+\frac{\varepsilon^*(t)e^{-i(\omega_e-\omega_g-\omega_0 t)}}{\omega_{me}+\omega_0}\right]\right\}\langle g|\hat{H}_{AF}|m\rangle \quad (3.22a)$$

$$i\hbar\dot{a}_e = \sum_m \left\{\frac{\mu_{mg}}{2\hbar} a_g(t)\left[\frac{\varepsilon(t)e^{-i(\omega_g-\omega_e+\omega_0 t)}}{\omega_{mg}-\omega_0}+\frac{\varepsilon^*(t)e^{-i(\omega_g-\omega_e-\omega_0 t)}}{\omega_{mg}+\omega_0}\right]+ \frac{\mu_{me}}{2\hbar} a_e(t)\left[\frac{\varepsilon(t)e^{-i\omega_0 t}}{\omega_{me}-\omega_0}+\frac{\varepsilon^*(t)e^{i\omega_0 t}}{\omega_{me}+\omega_0}\right]\right\}\langle e|\hat{H}_{AF}|m\rangle \quad (3.22b)$$

Using the matrix elements for interacting Hamiltonian H_{AF} Eq. 3.5,

$$i\hbar\dot{a}_g = -\sum_m \left\{\frac{\mu_{mg}}{4\hbar} a_g(t)\left[\frac{\varepsilon(t)e^{-i\omega_0 t}}{\omega_{mg}-\omega_0}+\frac{\varepsilon^*(t)e^{i\omega_0 t}}{\omega_{mg}+\omega_0}\right]+ \frac{\mu_{me}}{4\hbar} a_e(t)\left[\frac{\varepsilon(t)e^{-i(\omega_e-\omega_g+\omega_0 t)}}{\omega_{me}-\omega_0}+\frac{\varepsilon^*(t)e^{-i(\omega_e-\omega_g-\omega_0 t)}}{\omega_{me}+\omega_0}\right]\right\}\mu_{mg}\left(\varepsilon(t)e^{-\imath w_o t}+c.c\right) \quad (3.23a)$$

$$i\hbar\dot{a}_e = -\sum_m \left\{\frac{\mu_{mg}}{4\hbar} a_g(t)\left[\frac{\varepsilon(t)e^{-i(\omega_g-\omega_e+\omega_0 t)}}{\omega_{mg}-\omega_0}+\frac{\varepsilon^*(t)e^{-i(\omega_g-\omega_e-\omega_0 t)}}{\omega_{mg}+\omega_0}\right]+ \frac{\mu_{me}}{4\hbar} a_e(t)\left[\frac{\varepsilon(t)e^{-i\omega_0 t}}{\omega_{me}-\omega_0}+\frac{\varepsilon^*(t)e^{i\omega_0 t}}{\omega_{me}+\omega_0}\right]\right\}\mu_{me}\left(\varepsilon(t)e^{-\imath w_o t}+c.c\right), \quad (3.23b)$$

we define,

$$\Delta = \omega_e - \omega_g - 2\omega_0 = \omega_{eg} - 2\omega_0,$$

to get,

$$
\begin{aligned}
i\hbar\dot{a}_g &= -\sum_m \left\{ \frac{\mu_{mg}}{4\hbar} a_g(t) \left[\frac{\varepsilon(t)e^{-i\omega_0 t}}{\omega_{mg}-\omega_0} + \frac{\varepsilon^*(t)e^{i\omega_0 t}}{\omega_{mg}+\omega_0} \right] + \right. \\
&\left. \frac{\mu_{me}}{4\hbar} a_e(t) \left[\frac{\varepsilon(t)e^{-i(\Delta+3\omega_0 t)}}{\omega_{me}-\omega_0} + \frac{\varepsilon^*(t)e^{-i(\Delta+\omega_0 t)}}{\omega_{me}+\omega_0} \right] \right\} \mu_{mg} \left(\varepsilon(t)e^{-\imath w_o t} + c.c \right) \qquad (3.24a) \\
i\hbar\dot{a}_e &= -\sum_m \left\{ \frac{\mu_{mg}}{4\hbar} a_g(t) \left[\frac{\varepsilon(t)e^{-i(-\Delta-\omega_0 t)}}{\omega_{mg}-\omega_0} + \frac{\varepsilon^*(t)e^{-i(-\Delta-3\omega_0 t)}}{\omega_{mg}+\omega_0} \right] + \right. \\
&\left. \frac{\mu_{me}}{4\hbar} a_e(t) \left[\frac{\varepsilon(t)e^{-i\omega_0 t}}{\omega_{me}-\omega_0} + \frac{\varepsilon^*(t)e^{i\omega_0 t}}{\omega_{me}+\omega_0} \right] \right\} \mu_{me} \left(\varepsilon(t)e^{-\imath w_o t} + c.c \right) \qquad (3.24b)
\end{aligned}
$$

Applying the two photon RWA, so that we keep terms that oscillate at Δ or less, simplifies the above expressions greatly,

$$
\begin{aligned}
i\hbar\dot{a}_g &= -\sum_m \left\{ \frac{\mu_{mg}}{4\hbar} a_g(t) \left[\frac{|\varepsilon(t)|^2}{\omega_{mg}-\omega_0} + \frac{|\varepsilon(t)|^2}{\omega_{mg}+\omega_0} \right] + \right. \\
&\left. \frac{\mu_{me}}{4\hbar} a_e(t) \left[\frac{\varepsilon(t)^{*2}(t)e^{-i\Delta t}}{\omega_{me}+\omega_0} \right] \right\} \mu_{mg} \qquad (3.25a) \\
i\hbar\dot{a}_e &= -\sum_m \left\{ \frac{\mu_{mg}}{4\hbar} a_g(t) \left[\frac{\varepsilon(t)^2 e^{i\Delta t}}{\omega_{mg}-\omega_0} \right] + \right. \\
&\left. \frac{\mu_{me}}{4\hbar} a_e(t) \left[\frac{|\varepsilon(t)|^2}{\omega_{me}-\omega_0} + \frac{|\varepsilon(t)|^2}{\omega_{me}+\omega_0} \right] \right\} \mu_{me} \qquad (3.25b)
\end{aligned}
$$

The term proportional to a_g in 3.25a and to a_e in 3.25b is very similar to the AC Stark shift found in the case single photon interactions in two level systems [14]. The shift in this case is time dependent since it scales with the field's intensity envelope $g(t)$. For this reason it is called Dynamic Stark Shift (DSS). We will define the DSS for the ground and excited states $\omega^{(s)}_{\{e,g\}}(t)$ as,

$$
\omega^{(s)}_{\{e,g\}}(t) = -\sum_m \frac{\mu^2_{\{e,g\}m}}{2\hbar^2} |\varepsilon(t)|^2 \frac{\omega_{m\{e,g\}}}{\omega^2_{m\{e,g\}} - \omega_0^2} = \omega^{(s)}_{\{e,g\}} |\varepsilon(t)|^2. \qquad (3.26)
$$

The two photon Rabi frequency, $\chi(t)$, is similarly defined,

$$\begin{aligned}\chi(t) &= -\sum_m \frac{\mu_{em}\mu_{mg}}{(2\hbar)^2}\frac{\varepsilon(t)^2}{\omega_{mg}-\omega_0} = \chi_0\varepsilon(t)^2 \\ \chi^*(t) &\simeq -\sum_m \frac{\mu_{gm}\mu_{me}}{(2\hbar)^2}\frac{\varepsilon(t)^{*2}}{\omega_{me}+\omega_0} = \chi_0\varepsilon(t)^{*2}.\end{aligned} \tag{3.27}$$

Note that when the time dependence is removed from $\omega^{(s)}_{\{e,g\}}(t)$ and $\chi(t)$, we are explicitly removing the field dependence from the atomic coupling constants.

With these convenient definitions Eqs. 3.25 become,

$$\begin{aligned}\dot{a}_g(t) &= -i\omega^{(s)}_g(t)a_g(t) - i\chi^*(t)e^{-\imath\Delta t}a_e(t), \\ \dot{a}_e(t) &= -i\omega^{(s)}_e(t)a_e(t) - i\chi(t)e^{\imath\Delta t}a_g(t).\end{aligned} \tag{3.28}$$

In Hamiltonian form,

$$i\hbar\dot{\mathbf{a}} = \hat{\mathbf{H}}(t)\mathbf{a}, \quad \mathbf{a} = \begin{pmatrix} a_g \\ a_e \end{pmatrix}, \tag{3.29}$$

and

$$\hat{\mathbf{H}}(t) = \hbar\begin{pmatrix} \omega^{(s)}_g(t) & \chi^*(t)e^{-\imath\Delta t} \\ \chi(t)e^{\imath\Delta t} & \omega^{(s)}_e(t) \end{pmatrix}. \tag{3.30}$$

An important thing that distinguishes this Hamiltonian from that for a single photon coupled two level Hamiltonian in Eq. 3.11, is that the diagonal terms are time dependent as well as the off diagonal. Furthermore they both scale with the field's intensity. This means that the energy of both levels will follow the intensity envelope. The direction in which they move (closer or further apart) will depend on the detuning of all the off-resonant states. More specifically, the direction is determined by the relative displacement of the ground $\omega^{(s)}_g(t)$ and excited $\omega^{(s)}_e(t)$ Stark shifts.

3.4 Phase matching as a mechanism for population transfer

Physical insight can be gained by transforming the Hamiltonian, in Eq. 3.30, into a slowly varying reference frame [62]. This field-interaction frame, in which the state amplitudes are given by $b_g(t)$ and $b_e(t)$, rotates at twice the

laser frequency and takes into account the temporal field phase and the average Stark shift of the states,

$$\begin{aligned} a_g(t) &= b_g(t)e^{i(\Delta t-\varphi)/2}e^{-i/2\int_{-\infty}^{t}[\omega_e^{(s)}(t')+\omega_g^{(s)}(t')]dt'} \\ a_e(t) &= b_e(t)e^{-i(\Delta t-\varphi)/2}e^{-i/2\int_{-\infty}^{t}[\omega_e^{(s)}(t')+\omega_g^{(s)}(t')]dt'}. \end{aligned} \tag{3.31}$$

After the transformation we get for $\hat{\mathbf{H}} \rightarrow \hat{\mathbf{H}}'$,

$$\hat{\mathbf{H}}' = \begin{pmatrix} -\frac{1}{2}(\delta_\omega^{(s)}(t) - \Delta + \dot{\varphi}(t)) & \chi(t) \\ \chi(t) & \frac{1}{2}(\delta_\omega^{(s)}(t) - \Delta + \dot{\varphi}(t)) \end{pmatrix}, \tag{3.32}$$

where the physically relevant differential Stark shift is defined as

$$\delta_\omega^{(s)}(t) = \omega_e^{(s)}(t) - \omega_g^{(s)}(t). \tag{3.33}$$

This form of the Hamiltonian highlights the fact that in strong fields, DSS's ($\delta_\omega^{(s)}(t)$) of the ground and excited states result in a changing resonance condition as the intensity of the laser pulse rises and falls since $\omega_{e,g}^{(s)} \propto I(t)$. The diagonal elements in the Hamiltonian Eq.3.32, lead us to define the quantity,

$$\alpha(t) = -\left[\int_{-\infty}^{t} \delta_\omega^{(s)}(t')dt' - \Delta t + \varphi(t)\right], \tag{3.34}$$

which is particularly useful for describing optimal excitation conditions in the strong field limit. $\alpha(t)$ can be interpreted in terms of an 'atom-field phase'. Keeping this phase constant (i.e. 'phaselocking') is equivalent to maintaining resonance despite movement of the atomic levels in the strong field of the laser. In order to arrive at an explicit expression for the optimal pulse shape in this general case, we transform the Hamiltonian of Eq.3.32 once more:

$$\begin{aligned} b_g(t) &= c_g(t)e^{-i\frac{1}{2}\alpha(t)} \\ b_e(t) &= c_e(t)e^{i\frac{1}{2}\alpha(t)}. \end{aligned} \tag{3.35}$$

We arrive at:

$$\hat{\mathbf{H}}'' = \begin{pmatrix} 0 & \chi(t)e^{i\alpha(t)} \\ \chi(t)e^{-i\alpha(t)} & 0 \end{pmatrix}, \tag{3.36}$$

from which the strong field π pulse condition is evident [63]:

$$\int_{-\infty}^{\infty} \chi(t)\exp[i\alpha(t)]dt = \frac{\pi}{2}. \tag{3.37}$$

This last equation makes the role of $\alpha(t)$ (Eq. 3.34) in determining the

population transfer for a given pulse shape clear. If $\alpha(t)$ evolves rapidly while the coupling $\chi(t)$ is significant, then the integral given in equation 3.37 will vanish as the atom-laser phase oscillates. Oscillation of the atom-laser phase corresponds to an oscillation between stimulated emission and absorption and they can cancel each other out to result in essentially zero net population transfer. Controlling the laser phase, $\varphi(t)$, allows for minimizing the variation of $\alpha(t)$ during the pulse, and therefore maximizing the population transfer. This is equivalent to maintaining resonance by dynamically following the instantaneous energy separation of the ground and excited state levels.

3.5 The weak field limit of the phase matching condition

From a theoretical perspective, one way of proving the validity of our model is to show that it contains, in the weak field limit, the perturbation model presented before. This model has been studied extensively [10–12] and modifications to it have also been proposed [18]. Our starting point is Hamiltonian Eq. 3.36,

$$\hat{\mathbf{H}}'' = \begin{pmatrix} 0 & \chi(t)e^{i\alpha(t)} \\ \chi(t)e^{-i\alpha(t)} & 0 \end{pmatrix}. \tag{3.38}$$

Clearly, the weak field limit of this general case imposes conditions, not only on the excited state amplitude, but also on the DSS of the ground and excited states. To illustrate this, we start with the Hamiltonian of Eq.3.36 and show that only in the limit of vanishing excited state amplitude *and* dynamic Stark shift,

$$\begin{aligned} \delta_{\omega}^{(s)} &\approx 0 \\ |a_g(t)| &\simeq 1, \end{aligned} \tag{3.39}$$

does one recover the perturbative limit Eq.3.13. For simplicity, we consider the case of zero two photon detuning $\Delta = 0$. Using Hamiltonian Eq. 3.36, the Schrödinger equation for amplitude c_e is,

$$\dot{c}_e(t) = i\chi_0 \int_{-\infty}^{\infty} \varepsilon(t)^2 e^{-i\int_{-\infty}^{t} \delta_{\omega}^{(s)}(t')} dt' c_g(t) dt, \tag{3.40}$$

with (see [31])

$$\chi_0 \quad = \quad -\sum_m \frac{\mu_{em}\mu_{mg}}{(2\hbar)^2}\frac{1}{\omega_{mg}-\omega_0}. \tag{3.41}$$

Only by taking the limit of a vanishing differential Stark shift and excited state population (Eq.3.39) can we arrive at the following result which agrees with the perturbation theory results given by Eq.3.13:

$$|a_e(t)|^2 = |c_e(t)|^2 = P_{g\to e} = |\chi_0|^2 \left| \int_{-\infty}^{\infty} \varepsilon(t)^2 \exp(i\Delta t) dt \right|^2 . \tag{3.42}$$

This derivation shows that the phase matching picture contains, as a limiting case, the weak field perturbative results. From this conclusion we can state that at weak fields, multiphoton transitions can be treated either in the frequency or time domain but, for strong fields, a time domain picture is more appropiate.

3.6 Three level systems in weak fields

An extension of the perturbative expression above describes the case of $2+1$ resonance mediated three photon absorption. This is a natural case to examine as an extension to the non-resonant two photon case because it combines the simplest non-resonant multiphoton case with a resonance enhancement involving the minimum number of states. Figure 3.3 shows a diagram of such transitions. Recent work has focused on control of resonance mediated three photon $(2+1)$ absorption in the weak field limit [17].

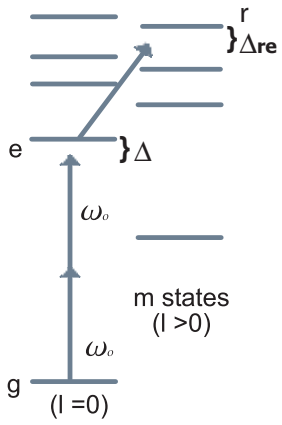

Figure 3.3: Resonant mediated three photon absorption. Indicated in the graph are the two relevant detunings Δ for the TPA, and Δ_{re} for the single photon transition.

Using again the RWA, third order perturbation theory yields the following expression for the probability amplitude, a_r, of the

third state, resonantly coupled to the intermediate level (the excited state, a_e, in the discussion above),

$$\begin{aligned} a_r(t) &= -\frac{1}{i\hbar^3}\sum_m \mu_{re}\mu_{em}\mu_{mg}\int_{-\infty}^{t}\int_{-\infty}^{t_1}\int_{-\infty}^{t_2}\varepsilon(t_1)\varepsilon(t_2)\varepsilon(t_3)\times \\ &\times \exp(-i\Delta_{re}t_1)\exp(-i\Delta_{em}t_2)\exp(-i\Delta_{mg}t_3)dt_1dt_2dt_3. \end{aligned} \quad (3.43)$$

Note the similarity between Eq. 3.12 and Eq. 3.43. As in the TPA case, the innermost integral can be performed explicitly assuming large detuning of the intermediate states for the two photon transition. We separate different contributions for excitation to the r state based on whether or not they involve a resonance enhancement from the intermediate state e. Details are given in references [16] and [17]. The final state amplitude in terms of resonant and near resonant contributions is,

$$\begin{aligned} a_r &\propto \left[a_r^{on-res} + a_r^{near-res}\right] \\ a_r^{on-res} &= i\pi\varepsilon(\omega)\int_{-\infty}^{\infty}\varepsilon(\omega)\varepsilon(\omega_{eg}-\omega)d\omega, \\ a_r^{near-res} &= \int_{-\infty}^{\infty}\varepsilon(\omega)\times\wp\int_{-\infty}^{\infty}\frac{\varepsilon(\omega')\varepsilon(\omega_{rg}-\omega-\omega')}{\omega_{eg}-(\omega+\omega')}d\omega'd\omega, \end{aligned} \quad (3.44)$$

with $\wp$ being the Cauchy principal value operator [17]. a_r^{on-res} contains the contribution to a_r from frequency combinations that are on resonant with the intermediate level and $a_r^{near-res}$ contains all other contributions.

Each on-resonant pathway corresponds to a combination of three photons of frequencies ω_{re}, ω, and ω' where $\omega+\omega'=\omega_{eg}$. Each near-resonant pathway corresponds to a combination of three photons of frequencies ω, ω', and ω'' where $\omega+\omega'+\omega''=\omega_{rg}$ and $\omega+\omega'-\omega_{eg}=\Delta\neq 0$ (i.e., non-zero detuning for the transition $g\rightarrow$ e)

3.7 Three levels in strong fields

The extension of the two level Hamiltonian to the case of a three level system where the third level is resonantly coupled to the excited state and dipole

allowed is simple:

$$\hat{\mathbf{H_3}}(t) = \begin{pmatrix} \omega_g^{(s)}(t) & \chi^*(t)e^{i(\Delta t-\varphi(t))} & 0 \\ \chi(t)e^{-i(\Delta t-\varphi(t))} & \omega_e^{(s)}(t) & \chi_{er}^*(t)e^{-i[\varphi(t)/2-\Delta_{er}t]} \\ 0 & \chi_{er}(t)e^{i[\varphi(t)/2-\Delta_{er}t]} & \omega_r^{(s)}(t) \end{pmatrix}. \tag{3.45}$$

with

$$\chi_{er}(t) = \frac{\mu_{re}}{2\hbar}\varepsilon(t). \tag{3.46}$$

Here, μ_{re} and Δ_{er} are the one photon coupling between the excited and resonant state, and the detuning. $\omega_r^{(s)}(t)$ is the DSS of the final (r) state. It can be noticed that Eq. 3.45 is obtained by combining Eq. 3.30 and Eq. 3.11. With this Hamiltonian we arrive at the equations of motion for the three state amplitudes that will be used in the simulations,

$$\begin{aligned} \dot{a}_g(t) &= -i\omega_g^{(s)}a_g(t) - i\chi(t)e^{\imath(\Delta t-\varphi(t))}a_e(t), \\ \dot{a}_e(t) &= -i\omega_e^{(s)}a_e(t) - i\chi(t)e^{-\imath(\Delta t-\varphi(t))}a_g(t) \\ &\quad + \frac{\imath}{2\hbar}\mu_{er}\varepsilon_0\sqrt{g(t)}e^{-\imath[\varphi(t)/2-\Delta_{er}t]}a_r(t), \\ \dot{a}_r(t) &= \frac{\imath}{2\hbar}\mu_{re}\varepsilon_0\sqrt{g(t)}e^{\imath[\varphi(t)/2-\Delta_{er}t]}a_e(t) - i\omega_r^{(s)}(t)a_r(t), \end{aligned} \tag{3.47}$$

As in the two level case, the perturbative solution Eq. 3.44 can be recovered from the general Hamiltonian Eq.3.45 in the same limit that the ground state is not depleted ($|a_g(t)| \simeq 1$) and the Stark shifts vanish ($\delta_\omega^{(s)} \approx 0, \omega_r^{(s)}(t) \approx 0$). The evolution of the intermediate and final state amplitudes, a_e and a_r, in this limit are given by

$$\dot{a}_e(t) = i\chi(t)e^{-i(\Delta t-\varphi(t))} \tag{3.48}$$

$$\dot{a}_r(t) = i\chi_{er}(t)e^{i(\varphi(t)/2-\Delta_{er}t)}a_e(t). \tag{3.49}$$

We can integrate these two equations explicitly, giving:

$$a_r(t) = -\int_{-\infty}^{t} dt' \int_{-\infty}^{t'} dt'' \chi_{er}(t')e^{i(\varphi(t')/2-\Delta_{er}t')}\chi(t'')e^{-i(\Delta t''-\varphi(t''))}. \tag{3.50}$$

Taking the limit $t \to \infty$, substituting for the Rabi frequencies and expressing the fields in terms of Fourier integrals, we recover the weak limit Eq.

3.44[16, 17]:

$$\begin{aligned} a_r^{on-res} &= i\pi\varepsilon(\omega)\int_{-\infty}^{\infty}\varepsilon(\omega)\varepsilon(\omega_{eg}-\omega)d\omega, \\ a_r^{near-res} &= \int_{-\infty}^{\infty}\varepsilon(\omega)\times\wp\int_{-\infty}^{\infty}\frac{\varepsilon(\omega')\varepsilon(\omega_{eg}-\omega-\omega')}{\omega_{eg}-(\omega+\omega')}d\omega' d\omega. \end{aligned} \quad (3.51)$$

This results is another confirmation that the proposed phase matching model for TPA in strong fields is valid.

3.8 Multiphoton transitions in atomic sodium

To study these transitions experimentally we choose atomic Sodium. Figure 3.4 shows the levels of atomic sodium and some transition frequencies.

The ground state of sodium is the $3s$, followed by the $3p$ and the $4s$. The transition from the ground state to the $4s$ requires two photons with wavelengths of 777 nm, which is close to the center wavelength of our femtosecond laser. The $3p$ transition to the ground state has a wavelength of 589 nm and is therefore very far from our laser center frequency. Also, since the $7p$ is resonant with the $4s$ state at 781.2 nm, we can target this transition as well. This means that using a single laser source we can study multiphoton transitions for the two and three level cases mentioned before. The latter includes going to the $7p$ through the $4s$ since other transitions are not possible at the available frequencies. Also a direct three photon transition to the $7p$ is very unlikely due to the fact that the coupling of the ground state to the 4s is very strong. We need to point out that we have neglected the atomic fine structure. For the intermediate, off-resonant levels it is justified because the detuning to the laser is much larger than the fine (and therefore hyperfine) splittings. The fine structure of the $3s$, $4s$, and $7p$ can be ignored since the bandwidth of our laser is much larger than the fine structure splitting.

Theoretical work with atomic Sodium is nice in the sense that it is one of the most studied elements. This means that quantum properties such as lifetimes and dipole moments are very well documented and tabulated. One such table can be found online at the National Institute of Standards and Technology (NIST) [1]. By using the measured Einstein A_{ki}, coefficients we can calculate the dipole moments for the relevant transitions (see also Appendix A.4). With the dipole moments, following Eqs. 3.26 and 3.27 we can calculate the DSS and the two photon coupling. The results of these calculations are shown in Table 3.1.

The table shows the most relevant levels to calculate the DSS and couplings.

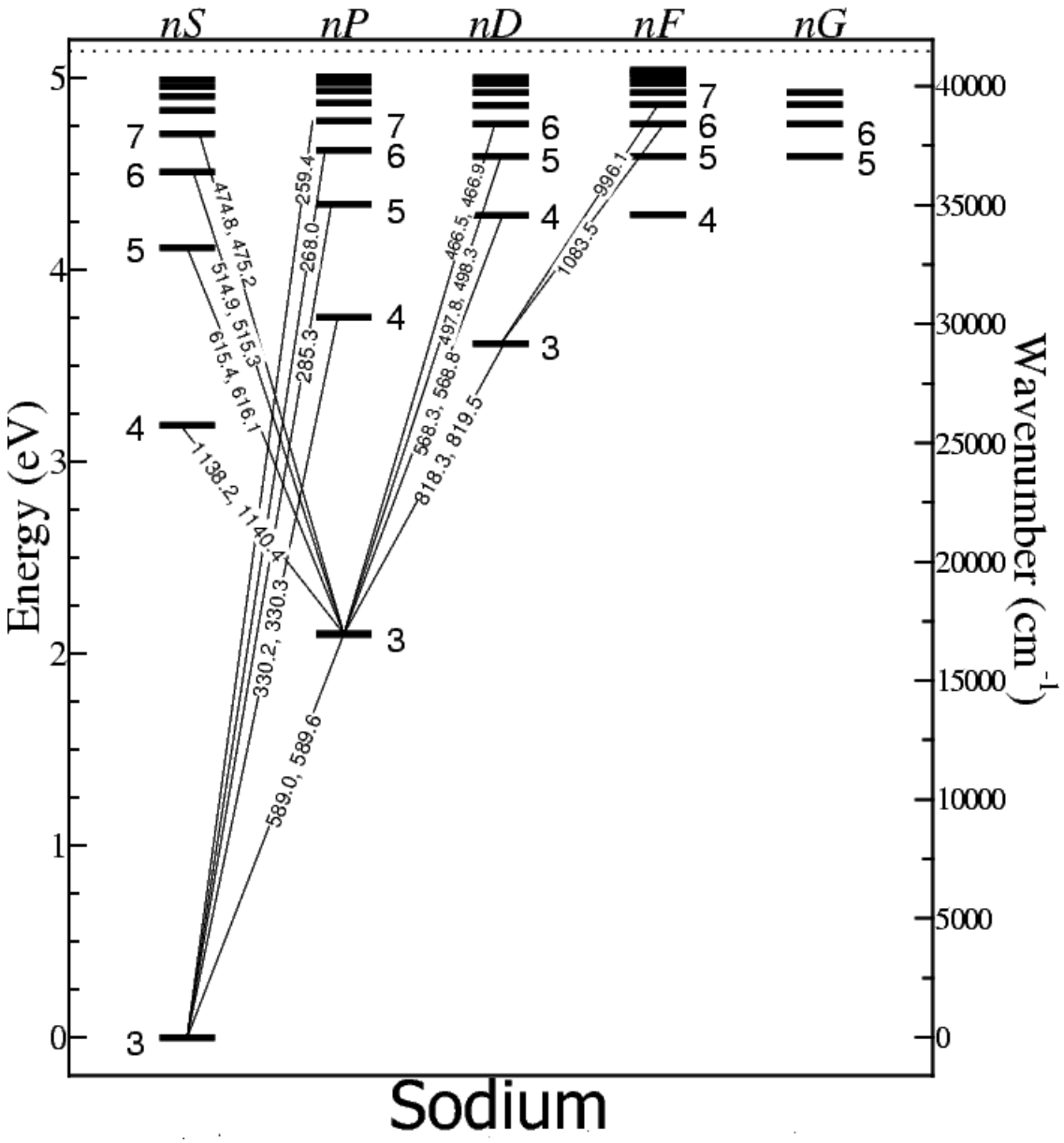

Figure 3.4: Level structure of atomic Na (from [**?**]). The two photon transition $3s \rightarrow 4s$ is at $3.19eV = 2 \times \frac{hc}{777nm}$. The 7p state is resonantly coupled with the $4s$ at $781.2nm$. The other states are off-resonance.

Table 3.1: Peak Stark shifts, dipole moments, and transition frequencies for the Na lines used in the calculations. All values are for center frequency $\omega_0 = 777$ nm and ideal π pulse intensity for a 50fs FWHM pulse. Stark shifts are calculated according to Eq. 3.26, and dipole moments are calculated from line strengths given in [1] according to [2].

Line	Dipole moment ($\times 10^{-29}$ Cm)	Transition Frequency ($\times 10^{15}$ rad/s)	Stark shift ($\times 10^{12}$rad/s)
3s-3p	2.11	3.19	-16.1
3s-4p	0.189	5.70	-0.0371
3s-5p	0.0703	6.60	-0.0043
4s-3p	2.09	1.65	-11.3
4s-4p	4.87	0.853	19.1
4s-5p	0.571	1.75	0.992
4s-6p	0.230	2.17	0.494
4s-7p	0.132	2.41	—-
4s-8p	0.0891	2.55	-0.153
7p-5s	0.448	1.00	0.404
7p-6s	1.75	0.409	2.14
7p-5d	0.672	0.284	0.242

Other levels give contributions of an order of magnitude or two smaller from the smallest values shown in the table and therefore we can safely exclude them from Eqs. 3.27 and 3.26. One basic check from the values tabulated above is that the sum of the frequencies for the $3s \rightarrow 3p$ (3.19×10^{15}rad/s) and the $3p \rightarrow 4s$ (1.65×10^{15} rad/s) transitions is equal to twice the frequency corresponding to a 777nm wavelength (2.42×10^{15}rad/s) and therefore two photons are required for the transition $3s \rightarrow 4s$. From the values of the DSS the reader might see the importance of the $4p$ and the $3p$ levels, since they give the largest contributions. Also, it should be noted that there is no contribution listed for the $7p$ to the DSS of the ground and excited state. This is because the $7p$ is one photon resonant with the $4s$ and it's treatment will be exactly as shown in the three level Hamiltonian Eq. 3.45. These tabulated values are for a peak intensity $I_0 = 2.88 \times 10^{15}\mathrm{W/m^2}$, which corresponds to a π pulse intensity, for a 50fs pulse, that inverts the $3s \rightarrow 4s$ two photon transition. Once we have the values for the peak DSS and two photon coupling we have all the information needed to simulate and test the theory just outlined above.

3.9 Compensating for the dynamic Stark shift

Since we are using pulsed fields, the instantaneous frequency in time of the electric field is given by the time derivative of the phase,

$$\omega(t) = \frac{\partial}{\partial t}\left(\omega_0 t + \varphi(t)/2\right). \tag{3.52}$$

In order to see how we can use our control over $\varphi(t)$ to compensate for the DSS, we recall the Hamiltonian in Eq. 3.32,

$$\hat{\mathbf{H}}' = \begin{pmatrix} -\frac{1}{2}(\delta_\omega^{(s)}(t) - \Delta + \dot{\varphi}(t)) & \chi(t) \\ \chi(t) & \frac{1}{2}(\delta_\omega^{(s)}(t) - \Delta + \dot{\varphi}(t)) \end{pmatrix}$$

This Hamiltonian shows the fundamental physics of a multiphoton transition in the presence of Stark shifts without resonant intermediate states. By coherently controlling $\varphi(t)$, one can cancel the diagonal elements of $\hat{\mathbf{H}}'$ and transfer population efficiently from $|g\rangle$ to $|e\rangle$ with a two-photon π-pulse:

$$\int_{-\infty}^{\infty} |\chi(t)| dt = \frac{\pi}{2} \tag{3.53}$$

$$\varphi(t) = \Delta t - \int_{-\infty}^{t} \delta_\omega^{(s)}(t') dt'. \tag{3.54}$$

Compensating for the atomic phase advance with the laser phase allows the two-photon pulse to remain on resonance throughout the pulse duration. To illustrate this point, in Figure 3.5 we show the population transfer to the $4s$ level for different phase compensations of the DSS. For $\Delta = 0$, we chose the following temporal phase,

$$\varphi(t) = -S \times \int_{-\infty}^{t} \delta_\omega^{(s)}(t') dt' \tag{3.55}$$

where complete compensation occurs for $S = 1$. The peak intensity I_0 for a π-pulse is calculated according to Eq.3.53.

Figure 3.5 shows the population of the $4s$ state, $|a_e(t)|^2$, from the numerical integration of Eqs. 3.47 for a 100 fs pulse with different values of the parameter S. The inset shows the dependence of the $4s$ and $7p$ state populations on pulse duration for $S = 1$. For a 100 fs pulse with $S = 1$, almost all of the population is transferred to the $4s$ state by the π-pulse, and almost no population is transferred to the $7p$. For small values of S, the atomic phase begins to vary rapidly during a pulse with the same intensity profile as the ideal ($S = 1$)

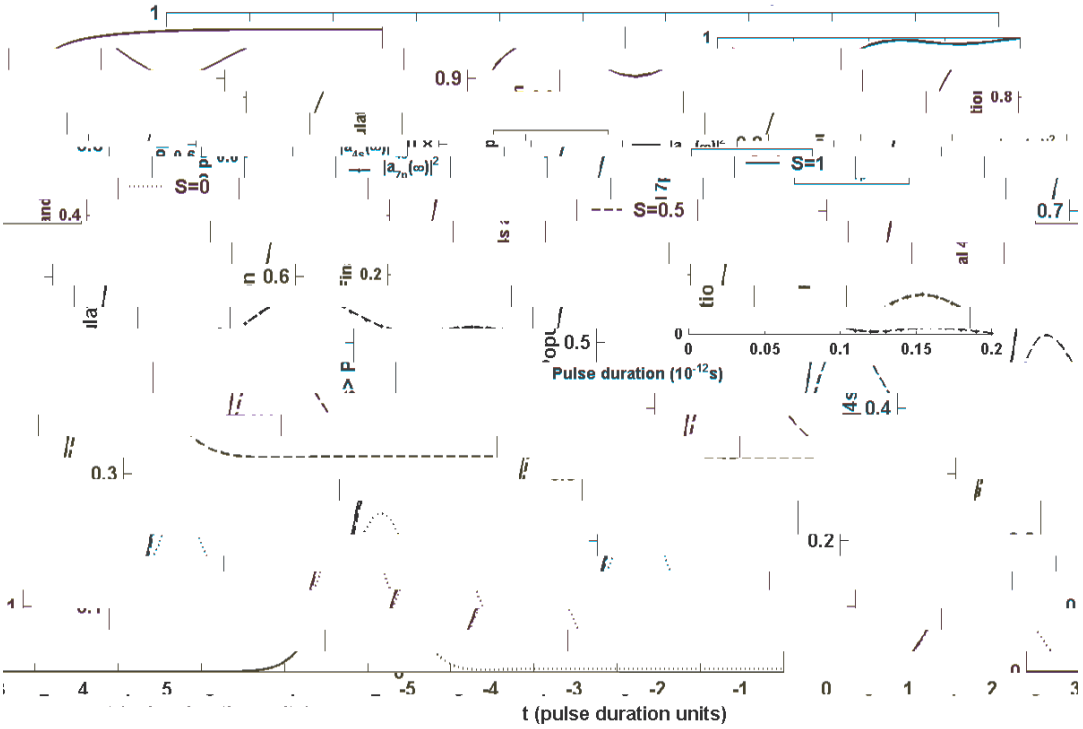

Figure 3.5: Sodium $|4s\rangle$ population, $|a_e(t)|^2$, for different values of the phase compensation parameter S for a 100 fs Gaussian pulse with peak intensity $I_0 = 1.44 \times 10^{15}\ W/m^2$ ($1.44 \times 10^{11} W/cm^2$) tuned to the bare resonance, $\lambda_0 = 777$ nm. The inset shows the final $|4s\rangle$ and $|7p\rangle$ populations as a function of pulse duration (FWHM).

pulse. Excited state population cannot build up as efficiently despite the pulse satisfying Eq. (3.53). In other words, for $S = 0$, the atom goes from stimulated absorption to stimulated emission during the pulse. These results at zero detuning show that multiphoton π-pulses can be achieved by tailoring the temporal phase of an ultrafast pulse to compensate for the dynamic Stark shift, and that in general, the phase compensation, S, can be used to control the population transfer.

The results presented in Figure 3.5 can be generalized to different detunings. Figure 3.6 shows the simulation results of a shaped pulse, with phase given by Eq. 3.55, as function of the compensation parameter S and center wavelength (before compensation). The peak intensity is that for a π pulse at 100fs and is the same for all combinations of S and λ_0. From the graph we see that there are several (infinite) combinations of phase and frequency that can lead to an efficient excitation, including an unshaped pulse ($S = 0$)at $\lambda_0 = 771$nm.

3.10 Density matrix formalism

So far it has been implicitly assumed that our quantum system is perfectly coherent. Although our 30fs laser system is much faster than any decoherence process, we will have to deal with some of them later on. For this, a density matrix formalism is more appropriate. In particular, we will derive the equations governing the evolution of slowly varying density matrices and will use this result for the two photon case. All of the above equations are defined in terms of slowly varying amplitudes a_j (they are called slowly varying because the quasi-stationary part has been removed from the atomic eigenvectors $|m>$). Accordingly, we can define a slowly varying density matrix,

$$Q_{nm}(t) = a_n(t)a_m^*(t), \tag{3.56}$$

for which the equation of motion (or time evolution) becomes,

$$\frac{\partial}{\partial t}Q_{nm}(t) = a_n(t)\frac{\partial}{\partial t}a_m^*(t) + a_m^*(t)\frac{\partial}{\partial t}a_n(t). \tag{3.57}$$

If we denote the matrix elements of our Hamiltonian by H_{mn}, the Schrödinger equation for the amplitudes can be written as (compare to Eqs. 3.8),

$$\frac{\partial}{\partial t}a_n(t) = -i/\hbar \sum_i H_{ni}a_i(t). \tag{3.58}$$

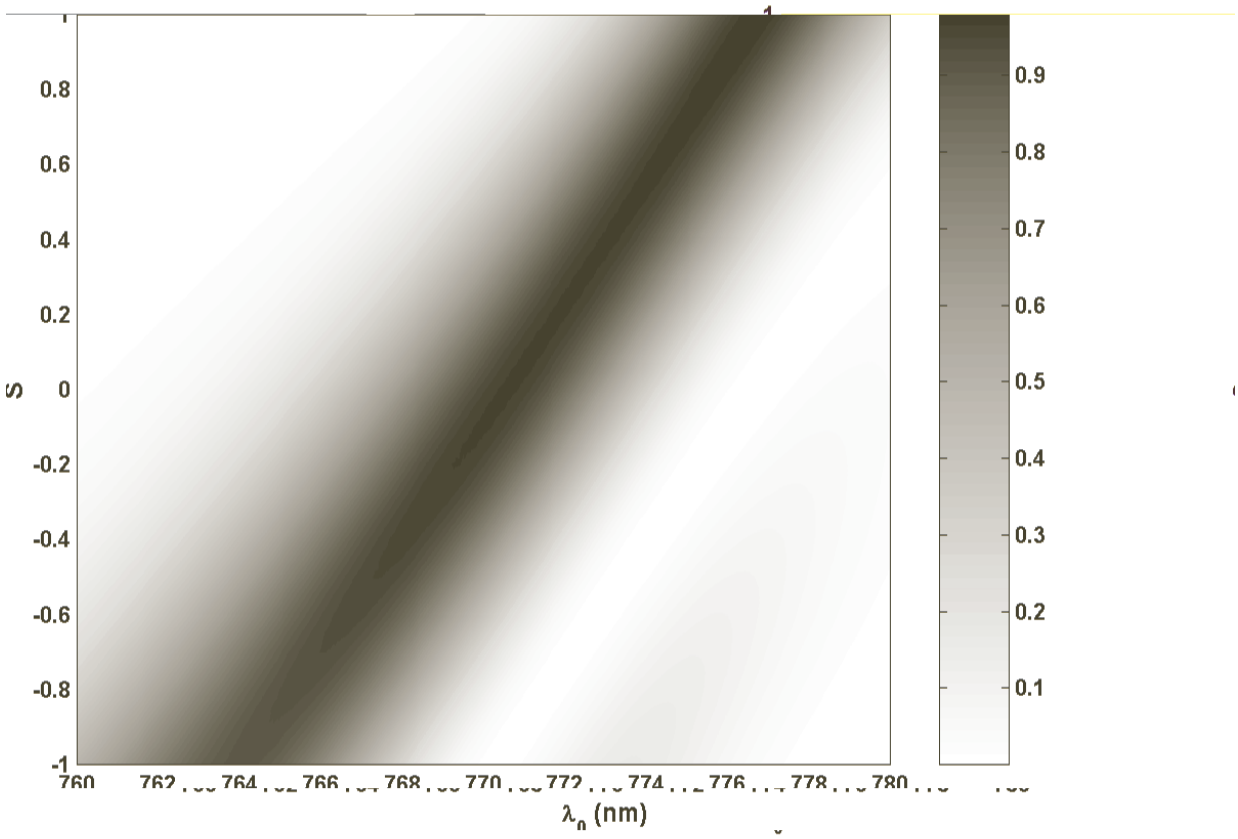

Figure 3.6: Final $|4s\rangle$ population, $|a_e(t \to \infty)|^2$, for a Gaussian pulse of 100 fs duration as a function of phase correction parameter S and λ_0. Population is proportional to the darkness of the shading as indicated by the scale on the right hand side, where 1 corresponds to 100% population transfer.

Substitute this into the evolution expression for Q_{nm} above,

$$\frac{\partial}{\partial t}Q_{nm}(t) = a_n(t)i/\hbar \sum_i H^*_{mi}a^*_i(t) - a^*_m(t)i/\hbar \sum_i H_{ni}a_i(t), \tag{3.59}$$

and to make it look Schrdinger like we pull put the $i\hbar$ term,

$$i\hbar\frac{\partial}{\partial t}Q_{nm}(t) = \sum_i H_{ni}a_i(t)a^*_m(t) - \sum_i H^*_{mi}a^*_i(t)a_n(t) \tag{3.60}$$

$$i\hbar\frac{\partial}{\partial t}Q_{nm}(t) = \sum_i H_{ni}Q_{im}(t) - \sum_i H^*_{mi}Q_{ni}(t). \tag{3.61}$$

Using now $H^*_{ij} = H_{ji}$ ($(HQ)_{nm} = \sum_j H_{nj}Q_{jm}$) we finally arrive at,

$$i\hbar\frac{\partial}{\partial t}Q(t) = \left[\hat{\mathbf{H}}, Q\right]. \tag{3.62}$$

This last equation dictates the evolution in time of the density matrix Q for any given Hamiltonian. We will use the two photon Hamiltonian obtained in Eq. 3.30. The two terms of the commutator are,

$$\begin{aligned}\mathbf{HQ} &= \hbar \begin{pmatrix} \omega_g^{(s)}(t) & \chi^*(t)e^{-\imath\Delta t} \\ \chi(t)e^{\imath\Delta t} & \omega_e^{(s)}(t) \end{pmatrix} \begin{pmatrix} Q_{11} & Q_{12} \\ Q_{21} & Q_{22} \end{pmatrix} \\ &= \begin{pmatrix} \omega_g^{(s)}(t)Q_{11} + \chi^*(t)e^{\imath-\Delta t}Q_{21} & \omega_g^{(s)}(t)Q_{12} + \chi^*(t)e^{\imath-\Delta t}Q_{22} \\ \chi(t)e^{\imath\Delta t}Q_{11} + \omega_e^{(s)}(t)Q_{21} & \chi(t)e^{\imath\Delta t}Q_{12} + \omega_e^{(s)}(t)Q_{22} \end{pmatrix}\end{aligned} \tag{3.63}$$

and,

$$\begin{aligned}\mathbf{QH} &= \hbar \begin{pmatrix} Q_{11} & Q_{12} \\ Q_{21} & Q_{22} \end{pmatrix} \begin{pmatrix} \omega_g^{(s)}(t) & \chi^*(t)e^{\imath-\Delta t} \\ \chi(t)e^{\imath\Delta t} & \omega_e^{(s)}(t) \end{pmatrix} \\ &= \begin{pmatrix} \omega_g^{(s)}(t)Q_{11} + \chi(t)e^{\imath\Delta t}Q_{12} & \chi^*(t)e^{\imath-\Delta t}Q_{11} + \omega_e^{(s)}(t)Q_{12} \\ \omega_g^{(s)}(t)Q_{21} + \chi(t)e^{\imath\Delta t}Q_{22} & \chi^*(t)e^{\imath-\Delta t}Q_{21} + \omega_e^{(s)}(t)Q_{22} \end{pmatrix}\end{aligned} \tag{3.64}$$

With this, we obtain the set of coupled differential equations for the Q's,

$$
\begin{aligned}
i\hbar\frac{\partial}{\partial t}Q_{11} &= \hbar\chi^*(t)e^{-\imath\Delta t}Q_{21} - \hbar\chi(t)e^{\imath\Delta t}Q_{12} && \text{(3.65a)}\\
i\hbar\frac{\partial}{\partial t}Q_{22} &= \hbar\chi(t)e^{\imath\Delta t}Q_{12} - \hbar\chi^*(t)e^{-\imath\Delta t}Q_{21} && \text{(3.65b)}\\
i\hbar\frac{\partial}{\partial t}Q_{12} &= \hbar\chi^*(t)e^{\imath-\Delta t}(Q_{22}-Q_{11}) + \hbar Q_{12}(\omega_g^{(s)}(t) - \omega_e^{(s)}(t)) && \text{(3.65c)}\\
i\hbar\frac{\partial}{\partial t}Q_{21} &= \hbar\chi(t)e^{\imath\Delta t}(Q_{11}-Q_{22}) + \hbar Q_{21}(\omega_e^{(s)}(t)) - \omega_g^{(s)}(t))) && \text{(3.65d)}
\end{aligned}
$$

Using the properties of the density matrix $Q_{ij} = Q_{ji}^*$, these equations reduce to,

$$
\begin{aligned}
i\hbar\frac{\partial}{\partial t}Q_{11} &= 2\hbar\,\mathrm{Im}\left\{\chi^*(t)e^{\imath-\Delta t}Q_{21}\right\} && \text{(3.66a)}\\
i\hbar\frac{\partial}{\partial t}Q_{22} &= -2\hbar\,\mathrm{Im}\left\{\chi^*(t)e^{\imath-\Delta t}Q_{21}\right\} && \text{(3.66b)}\\
i\hbar\frac{\partial}{\partial t}Q_{21} &= \hbar\chi(t)e^{\imath\Delta t}(Q_{11}-Q_{22}) + \hbar Q_{21}\delta_\omega^{(s)}(t). && \text{(3.66c)}
\end{aligned}
$$

In principle these equations can be reduced even further since there is yet another constraint. Since Q_{11} and Q_{22} represent the probabilities of the electron to be in the ground or excited state respectively, they need to satisfy $Q_{11} + Q_{22} = 1$. However, we opted to leave them as such and use this last constraint as a measure of the precision of the simulations. This had some impact on the speed of the calculations. We will use Eqs. 3.66 as a starting point for the theory of Chapter 5

3.11 Overview of the numerical methods used

Our numerical simulations involved integrating the three-level, time-dependent, Schrödinger Eqs. 3.47 using a fourth order Runge-Kutta approach. In some cases a Predictor-Corrector method (pre-built) was used. MatLab was used for all simulations. The Predictor-Corrector method used were the MatLab built-in `ode23` and `ode45` subroutines. The Runge Kutta method was used for most of the simulations. This selection was made because our algorithm is several times faster than the existing one. Also, it allowed for more flexibility. Both methods were crossed checked with each other. Additionally, the three level calculations were checked against calculations with the intermediate off-resonant states included explicitly (up to 16 levels were included) and without

the RWA.

Chapter 4

Control of two photon absorption

At this point, with the aid of the results from the previous chapter (Section 3.3 in particular) we can develop a qualitative picture of what happens when trying to invert the population in a two level system with TPA. We concentrate on the case of the two photon transition $3s \rightarrow 4s$ in atomic Na. We mentioned before that the $4s$ (or e) level is at ≈ 3.1eV from the ground state $3s$ (or g). This means we need two photons at $\lambda_0 = 777$nm to be on resonance, $\Delta = 0$, with this transition. For a strong laser field however, even for $\Delta = 0$, as the electric field's intensity increases in time, the levels will move apart, this means that we will no longer be on resonance. In particular, when the field is the strongest we are the farthest away from the resonance condition. This means that the overall amount of population excited to the excited state can be far from 100%.

In Section 3.9 we showed an approach for compensating for the DSS. We did not mention, however, that this method has spectral consequences in the sense that the center frequency of the field will change for different values of the compensation parameter S. This is bad news from an experimental point of view. In the lab we have several constraints that are not easy to overcome. This is the reason why the choice of phase proposed in Eq. 3.55 is not ideal for our experimental setup.

4.1 Feedback control on the two photon 3s-4s transition

Our approach to this problem is to use closed loop feedback on the fluorescence decay after excitation of the atom to the $4s$. As explained in Chapter 2, we

use a GA to govern the feedback. As fitness for the algorithm we use the integral of the fluorescence signal (trace) of the $3p \rightarrow 3s$ decay as measured by the PMT. This transition is centered at 589 nm. The GA manipulates the spectral phase in the pulse shaper until it finds a tailored pulse that maximizes the fitness. Ideally we would like to measure the $4s \rightarrow 3p$ transition, however, the wavelength in this case is of $\lambda = 1141$ nm which is in the far infrared and therefore harder to detect.

One important aspect that has to be taken into account when doing the experiments is that the shape of the field required for compensating for the DSS depends on the intensity. This can be seen by analyzing the Hamiltonian in Eq. 3.32, where both the diagonal an off-diagonal elements scale as the intensity of the field. In general, laser beams have a Gaussian spatial profile. This means that, for a Gaussian distribution of intensities, the measured atom-light interaction comes from an ensemble of atoms differently exposed and the registered signal is an *average* over this ensemble. Here we can make use of the technique described in Section 2.4 for having an almost flat two-dimensional spatial intensity profile. In order to illustrate the importance of spatial filtering, in Figure 4.1 we show the integrated fluorescence from the 3p to 3s decay as a function of pulse energy with and without the pinhole. As a guide, the beam profiles with and without filtering, are shown in an inset (same as in Section 2.4).

The use of this filtering system is crucial when working in the strong field limit [33]. This figure shows the beginning of Rabi oscillations when using the pinhole whereas without the pinhole there is a monotonic increase in the florescence yield for all intensities. The maximum energy shown for the case of using the pinhole is determined by the damage threshold of the pinhole. With no spatial filtering, there is a Gaussian distribution of intensities in the interaction region and the collected fluorescence originates from an ensemble of atoms exposed to a large range of laser intensities. If we want to extract any information from the shaped field, then we need to use this filtering system.

At this point we can use the GA for finding pulse shapes that compensate for the DSS. We do not have any *a priori* information to know if this scheme works, since in the lab we have several constraints. The most obvious one is that there is a limited energy. Another very important constraint is the limited bandwidth and pulse shaper resolution. Despite these obstacles, the learning algorithm finds solutions that greatly improve upon an unshaped pulse. Figure 4.2 shows the normalized fitness of the GA as function of generation for a typical GA run. In this case there is an enhancement factor of 3 over a TL (unshaped) pulse.

While our pulse shaper is capable of shaping both the spectral phase and

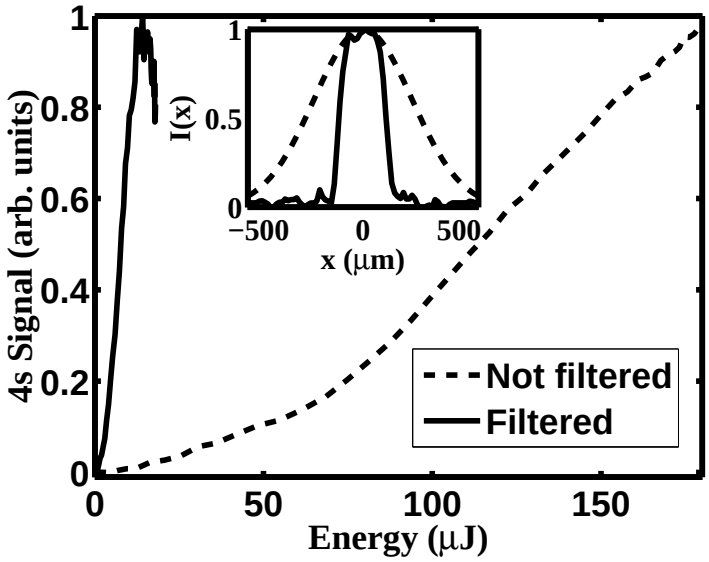

Figure 4.1: $4s$ signal as function of energy for a spatially filtered beam and a Gaussian beam. The presence of Rabi oscillations are detected only when using the filtering system. Note that the signals for both the unfiltered and filtered laser beam are each normalized to themselves. Inset: filtered (solid line) and not filtered (dashed line) spatial profiles measured at the interacting region.

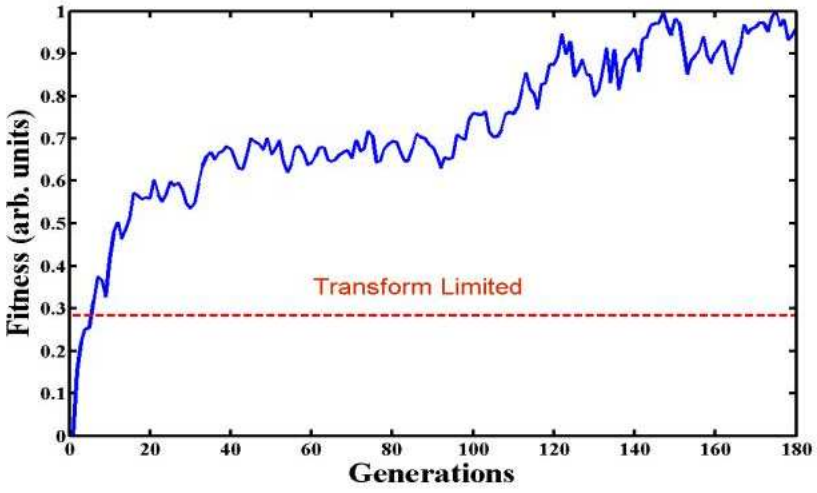

Figure 4.2: Normalized fitness as function of GA generation. Fitness is the integral of $3p \rightarrow 3s$ fluorescence traces.

amplitude of the pulses, we limited the pulse shaping in this experiment to phase only in order to work at a fixed pulse energy and to keep the number of degrees of freedom low enough for proper convergence of the learning algorithm. We performed the learning control experiments at three different central wavelengths (772 nm, 777 nm and 784 nm) around the bare resonance (777nm), because detuning plays an important role in the physics underlying control. For all three detunings, the GA was able to find pulse shapes that outperformed an unshaped pulse. At 777 nm and 784 nm, an optimal pulse increased the fluorescence yield by factors of 4.5 and 5 over an unshaped pulse respectively. To the blue, the increases were more modest - around a factor of 2.5. Running the GA in the weak field regime, where the pulse area was much less than π, yielded no improvement relative to an unshaped laser pulse.

From a control perspective this might be seen as a good result, however from a physical point of view it doesn't offer too much insight into the underlying process. Since coherent control of atomic and molecular processes has been already demonstrated, a more deep understanding of the control mechanisms is the current trend in our group [33, 64, 65] and in the community [66–68]. Optimal pulse shapes discovered by the algorithm were measured using SHG-FROG. The pulses had sufficient energy for a π pulse, with peak unshaped pulse intensities of about 3×10^{11} W/cm^2. The GA found an array of optimal pulses for each detuning. Figures 4.3a, b and c show optimal pulse shapes for central wavelengths of $\lambda_0 = 784$nm, $\lambda_0 = 772$nm, and $\lambda_0 = 777$nm respectively. For red detuning, the GA found the most consistent set of solutions, which have as a common feature the presence of two peaks separated in time, with a slowly and smoothly varying temporal phase. When the laser was tuned to the blue at $\lambda_0 = 772$nm , the GA found an array of solutions, which varied from complicated intensity and phase structure to a simple single pulse with a slowly varying temporal phase. Finally, at $\lambda_0 = 777$nm, various solutions consisted mostly of two and three sub-pulses. The different solutions for the three detunings do not immediately suggest a particular mechanism. Using these shaped fields to simulate the population to the excited state is the first step in gaining a comprehensive understanding of the control dynamics.

4.2 Simulation results with experimentally obtained fields

Although a simple idea, the task of using experimentally obtained fields as input for numerical simulations is complicated by the difficulty of making a very accurate pulse measurement. As we now know, the excitation probability

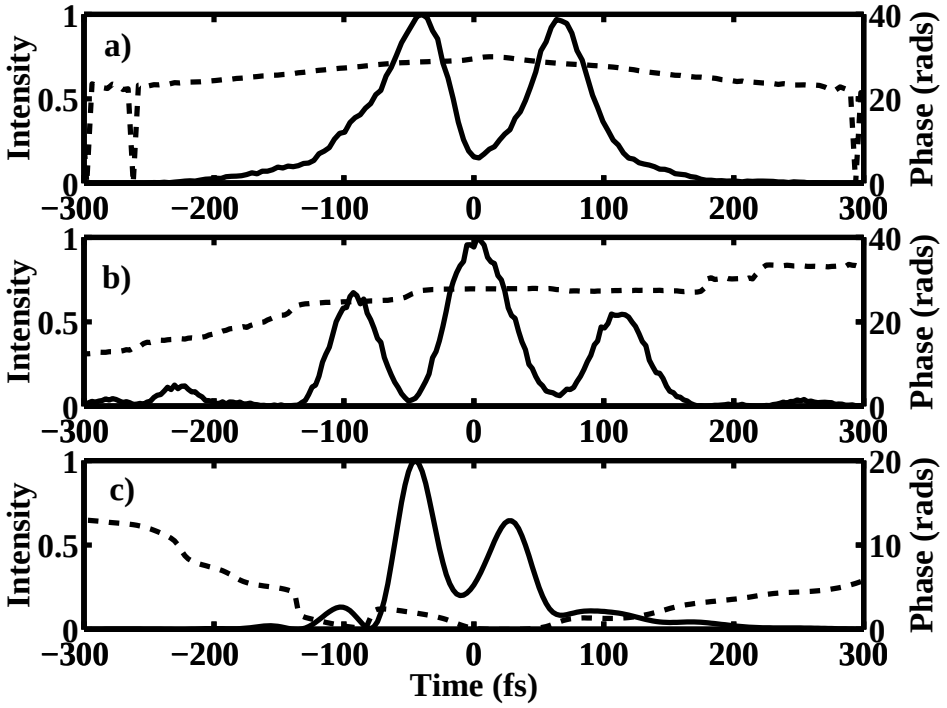

Figure 4.3: Intensity and phase of optimal pulses found by the GA for transferring population at different detunings. Panels a, b and c show pulses optimized at central wavelengths of $\lambda_0 = 784$nm, $\lambda_0 = 772$nm and $\lambda_0 = 777$nm respectively.

to the $4s$ is extremely sensitive to the phase and temporal profile shape of the field. This means that the intensity profiles and phases shown in the previous section need to be extremely accurate. There are several issues besides the usual noise that is present in the detection lines, or in the laser power. One of this issues is that, when using FROG for the field characterization, the relative height of the different peaks in time is not well determined. Also, if there are abrupt phase changes of π or even $\pi/2$ the reconstruction algorithm is not able to handle them. The strategy that we follow here is to use a theoretical parameterized pulse that follows very closely one obtained experimentally. If no clear parametrization is possible, then we use an experimentally obtained intensity and phase.

The most salient feature of the optimal pulses for red detuning ($\lambda_0 = 784$ nm) is the double pulse structure with a slowly varying temporal phase. Therefore we parameterized the field as two pulses separated by 110 fs, each pulse with a duration of 50 fs. Figure 4.4a shows the computed population as function of time for such parameterized field. Also shown in the figure as a dashed-dotted line is the population for a TL (unshaped) pulse *with the same energy* (area) as the two pulses.Panel a (Fig.4.4) shows that for a single unshaped laser pulse, the population in the $4s$ state goes up and comes back down to nearly zero during the pulse. For the optimal pulse solution, the population is as close as possible to being monotonically increasing for that detuning. Clearly, using two pulses is more efficient than one, even though the total shaped pulse energy is fixed.

As the solution for 772nm shown in Fig. 4.3b exhibits three pulses with phase jumps between pulses, we examine the population transfer as a function of time delay for three pulses with $\pi/2$ relative phase jump between pulses. Figure 4.4b show the simulation results for such an optical field. From Figure 4.3b, we can see that three pulses separated by 100fs, with $\pi/2$ phase jumps between pulses, and $\Delta = -1$THz leads to optimal excitation. We should also notice that an almost unshaped pulse at this detuning yields almost the same result as the three pulses one. The reason for this is basically that this detuning compensates for the average Stark shift (see Figure 3.6).

In order to interpret the solutions at 777nm, which were more difficult to parameterize because of their more complicated structure, we integrated the Schrödinger equation numerically for the algorithm-generated experimental pulse shapes. In Fig.4.4c, we show the $3s$ and $4s$ populations as function of time for the experimental pulse of Fig.4.3c, as well as for an unshaped pulse. Small phase errors in our pulse measurement and uncertainties in the experimental laser intensity account for the difference between the experimental and calculated contrast between a shaped and unshaped laser pulse. Nevertheless,

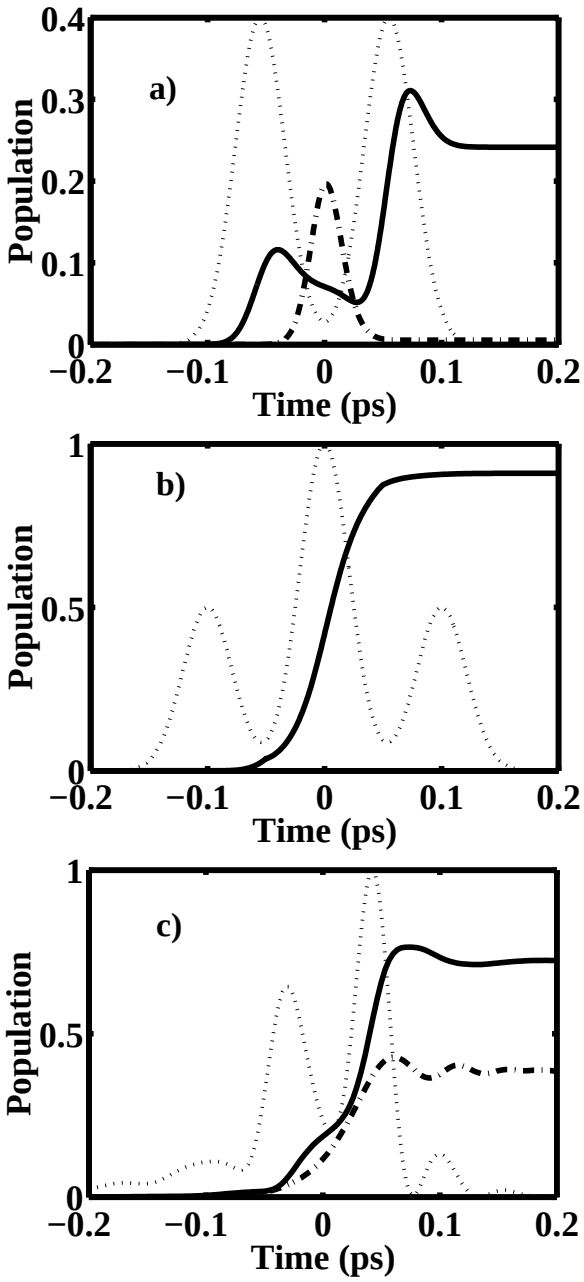

Figure 4.4: Panels a, b and c show the computed $4s$ population for shaped (solid) and unshaped pulses (dash-dot) vs. time for central wavelengths of $\lambda_0 = 784$nm, $\lambda_0 = 772$nm, $\lambda_0 = 777$nm respectively. Panels a and b are for parameterized pulse shapes and panel c is for a measured pulse. All panels also show the shaped pulse intensity profiles (dotted).

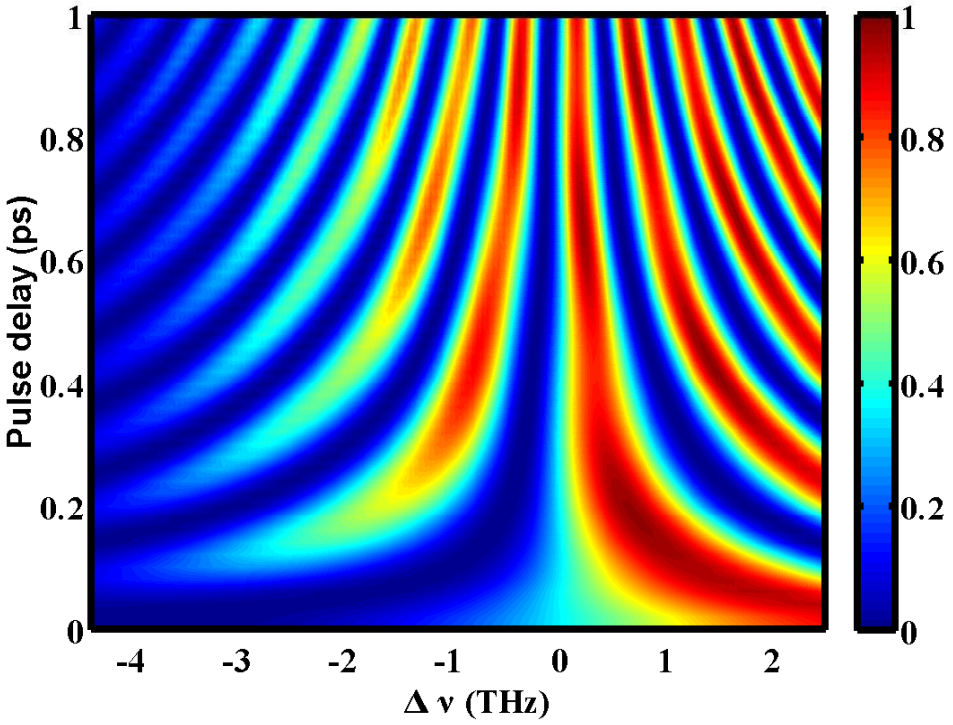

Figure 4.5: Final $4s$ population after interacting with a pair of laser pulses, with no relative phase, as a function of pulse delay and detuning from the two photon resonance

there is a definite enhancement when compared to a TL field.

4.3 Extension of the experimental results

The successful parametrization of the fields above leads to the question, is there any other combination of field shapes that can compensate for the DSS and thus give efficient population transfers? More importantly, we want to know if the parametrized fields shown above are isolated events, or if the GA actually found pulse shapes that belong to a family of pulses sharing generic mechanisms for the population transfer. To answer these questions we did simulations scanning the parameters involved in those fields.

Figure 4.5 shows the final $4s$ population for a pair of pulses as a function of detuning from the bare resonance and the time delay between the two pulses. The intensity is chosen such that the integral of $2\chi(t)$ is π for the pulse pair

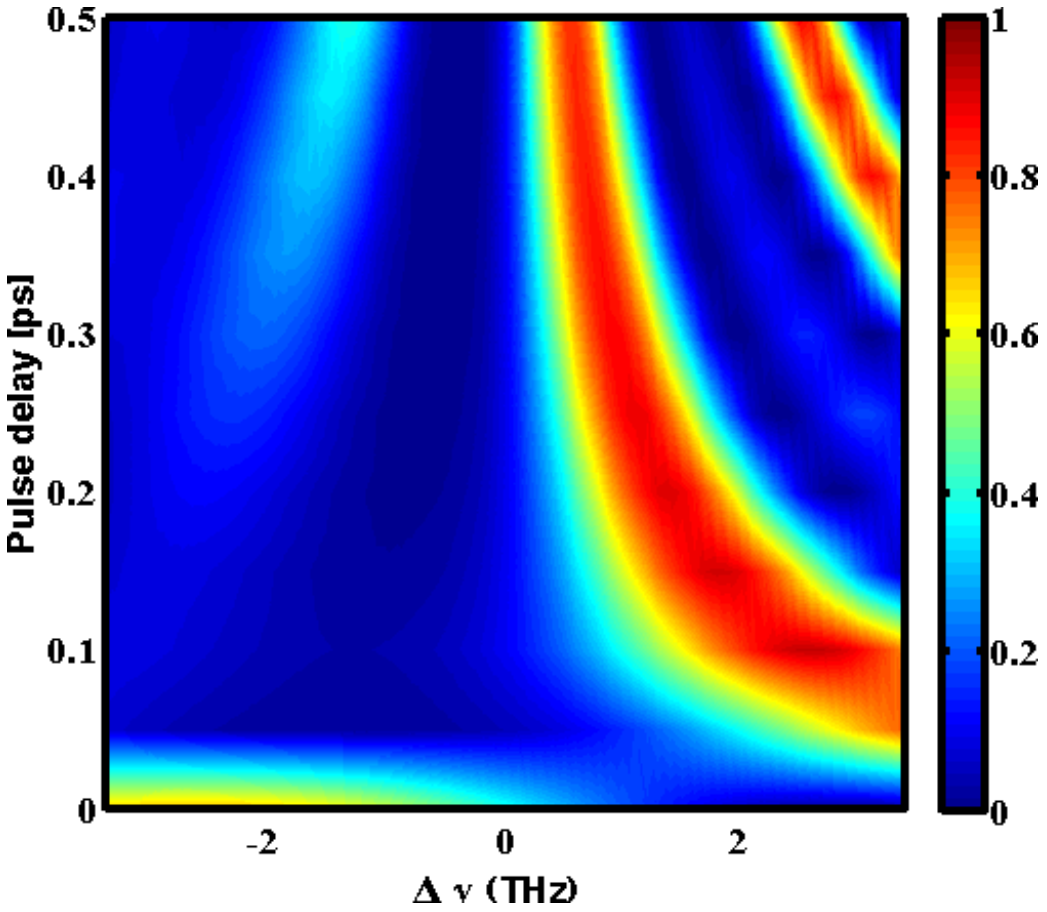

Figure 4.6: Final 4s population after interacting with three pulses as function of pulse delay between pulses with a $\pi/2$ phase jump in between pulses.

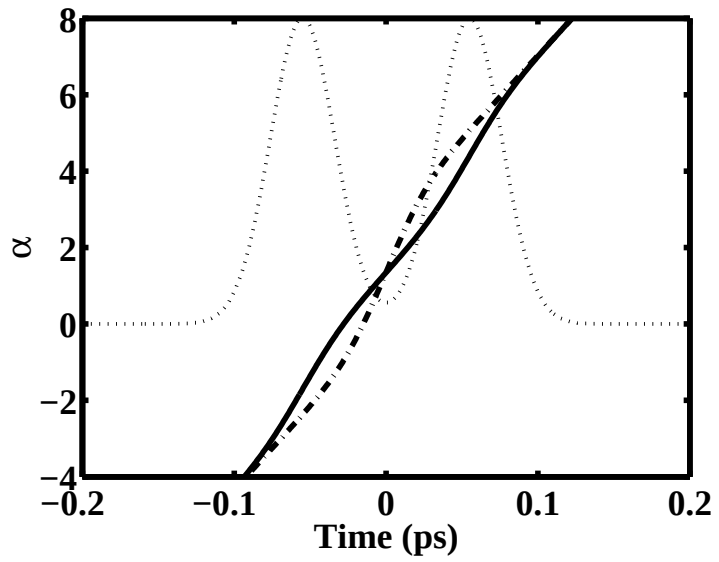

Figure 4.7: Atom-field phase, $\alpha(t)$ for an unshaped pulse (dash-dot) and the optimal pulse shown in Figure 4.4a (solid).

(minimum pulse energy required for full inversion) and the duration of each pulse is $\tau = 50$fs. Figure 4.6 shows the same, but for three pulses with a $\pi/2$ phase jump between the pulses. The middle pulse is twice as high as the other two. The duration of each individual pulse is of $50fs$ and the intensity is normalized in such a way that the total area is the same as a 50fs TL pulse. From both figures we can see that there are indeed several (infinite) combinations of delay between pulses and detunings that lead to optimum excitations. This establishes that solutions found by the GA are robust and a systematic part of a large class of solutions.

To give a clearer picture of how the phase matching works, we will take as an example the double pulse solution discovered by the GA for $\lambda_0 = 784$nm. Let's reinterpret the result shown for the population as function of time, but now with the aid of the atom-field phase matching picture. By comparing Figure 4.4a with Figure 4.7, we see that if the atom-field phase parameter $\alpha(t)$ (See Eq. 3.34),

$$\alpha(t) = -\left[\int_{-\infty}^{t} \delta_{\omega}^{(s)}(t')dt' - \Delta t + \varphi(t)\right],$$

goes beyond $\pm\pi/2$ during the pulse, the pulse begins to stimulate emission

rather than absorption, leading to less efficient population transfer. This is why it is more efficient to split the pulse into two such that $\alpha(t)$ evolves slower, while the field is on, and the atom can rephase with the field between subpulses (Figure 4.7), minimizing the amount of stimulated emission. Note that $\alpha(t)$ evolves by 2π between pulses in Figure 4.7. The action of turning off the coupling between states while the atom and field rephase is analogous to quasi-phase matching in nonlinear optics [69]. The separation of the excitation energy into two temporal pulses allows full use of the π pulse while the single-peaked π pulse necessarily imposes a Stark shift that forces a rapid phase-mismatch between the atom and effective two-photon field amplitude [31]. Of course, tuning the central frequency of the laser pulse would also provide a valid solution, but this is prevented by the experimental constraint of a fixed central frequency.

In Section 3.5 we saw how our model contains, as a special case, the perturbative limit. However, not only the two limits are interesting, but the transition from weak to strong field TPA is of great interest to us as well.

4.4 The transition from weak to strong fields

In order to illustrate how pulse shaping is required to maximize population transfer as one moves from the weak to strong field regime, we used our GA to optimize the excitation to the 4s state at different laser pulse energies. Figure 4.8 shows the ratio $P_{optimal}/P_{unshaped}$ for the 4s population transfer as a function of pulse energy. $P_{optimal}$ is the population transfer obtained with a feedback shaped pulse and $P_{unshaped}$ is the population transfer obtained with an unshaped pulse. There is a smooth transition from the weak to strong field regime illustrated by the improvement in a shaped pulse relative to an unshaped one. The unshaped pulse becomes increasingly inadequate with increasing intensity and DSS while the shaped pulse is able to compensate and maintain efficient population transfer [33]. Note that in the weak field limit, the ratio goes to 1. The intensity I_0 corresponds the peak intensity required for a π pulse of 50fs FWHM duration. The ratio at high pulse energies is limited in part by our ability to eliminate spatial intensity averaging in the focus of the laser. Without the pinhole, the ratio would be about 1 for all intensities. The error bars indicate the variation in population transfer for several optimizations at the same pulse energy.

To get a detailed picture of the change in dynamics going from the weak to strong field regime, we performed a systematic study of the co-dependence on pulse shape and intensity for a simple and intuitive pulse shape parametrization - a π phase jump in the spectral phase. This pulse parametrization can

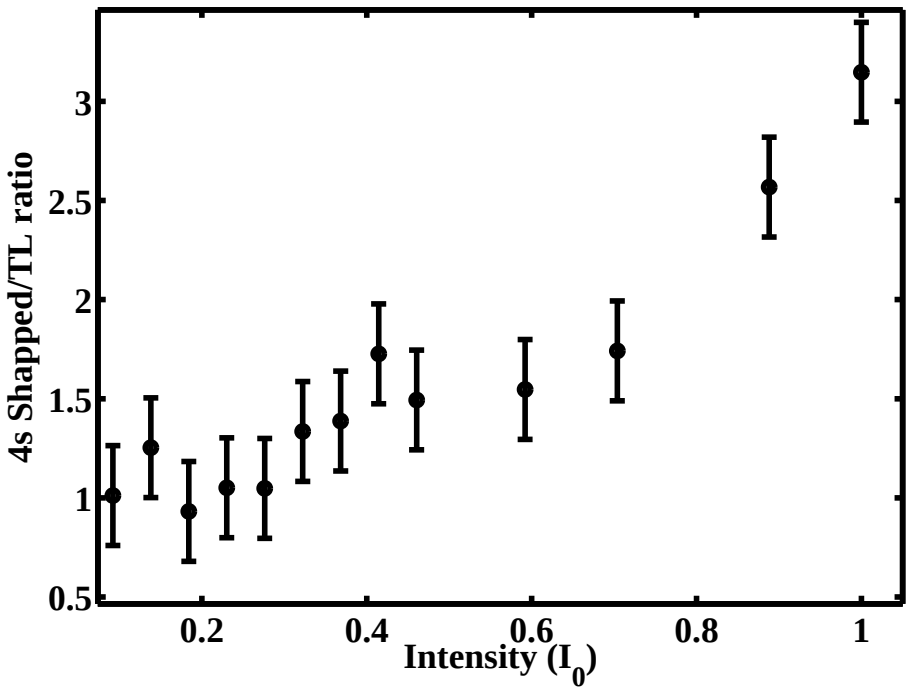

Figure 4.8: Ratio of 4s population for a GA maximized pulse to an unshaped one vs intensity. I_0 is the peak intensity required for a π pulse on the 3s-4s transition. Center wavelength is $\lambda_0 = 780nm$.

be interpreted in both the weak and strong field regimes and provides a direct measure of the DSS as discussed below. For weak field two photon excitation to the $4s$ state, a π phase jump in the spectral phase can yield either optimal excitation or a nearly dark pulse depending on the position of the phase jump [11]. For strong field excitation, the effect of a π spectral phase jump is best viewed in the time domain. The π spectral jump produces a pair of pulses with a smoothly varying phase which evolves by about π between pulses. Depending on the intensity and pulse spacing, this can result in constructive interference between the contributions of the two pulses (quasi phase matching) and optimal transfer, or destructive interference (anti-quasi phase matching) and a dark pulse. Note that this is not simply spectral interference. The spectrum of the laser pulse is constant, and so there are no spectral modulations in the pulse as a function of delay as with a Michelson interferometer. Furthermore, in the strong field limit, the resonance condition is dynamic, meaning that there is no well defined total frequency to which different combinations of spectral components can add constructively or destructively. As demonstrated below by the variation in population transfer with pulse energy for a given pulse shape, calculations based on a weak field model using spectral interference [11] do not accurately predict the population transfer achieved by a strong field laser pulse. Our measurements can be compared directly with [11], which were obtained in the weak field limit. The transition from the weak to strong field regime is highlighted by observing how the population transfer dependence on spectral phase jump position changes with intensity and the resonance conditions become dynamic.

Figure 4.9a shows the experimental measurement of the $4s$ population following excitation by a pulse with a π spectral phase jump as a function of both pulse energy and phase jump position. Figure 4.9b) shows the $4s$ population vs spectral phase jump position for several different intensities. Panels c) and d) show calculations of the $4s$ population after the same pulses using the Hamiltonian in Eq.3.45 for comparison with the experimental results. The calculations agree well with the experimental results at all intensities, with no adjustable parameters. At low intensities, where the DSS is negligible, the measurement reproduces the perturbative results in [11]. However, as the pulse energy increases (and therefore the peak intensity) there are three interesting features to note. One is the shift from right to left of the central peak which corresponds to having the π spectral phase jump on resonance. Another is the growth of this peak above the values far from resonance (unshaped pulse), and the third is the growth of a new peak at around 800 nm. All three features can be understood in terms of dynamic Stark shifting of the resonance and the integration of the Schrödinger equation using Eq. 3.36. The shifting of

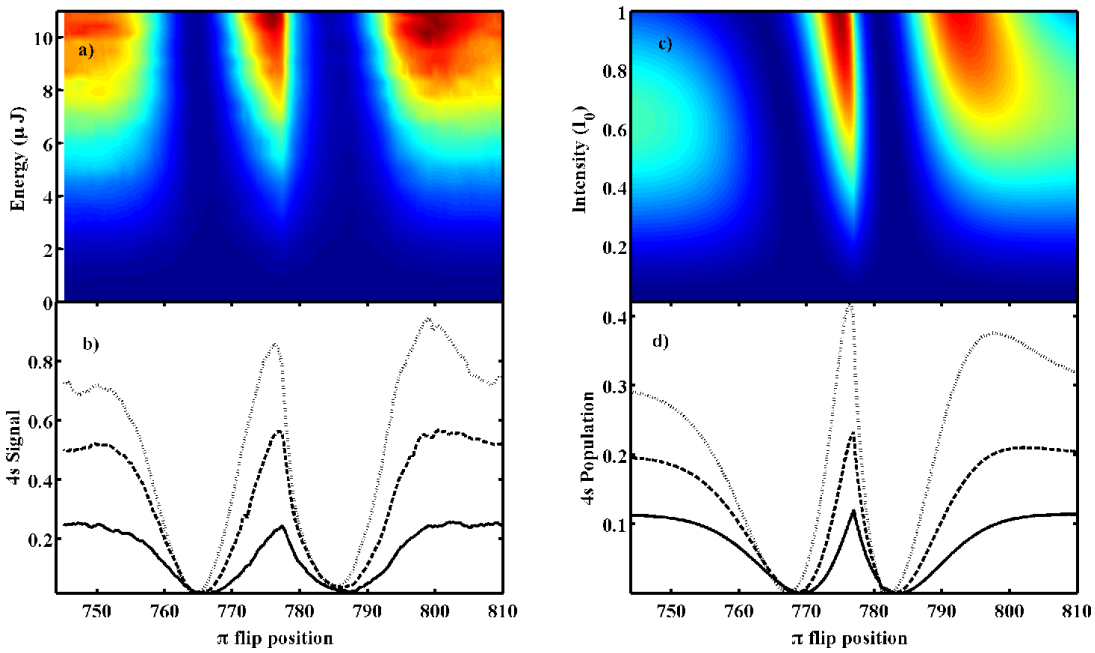

Figure 4.9: a) Experimental measurement of the 4s population as function of pulse energy (equivalent to peak intensity) and π flip position. b) Line outs of a) for three different pulse energies. c) Simulation of the 4s population as function of peak intensity and π flip position. d) Line outs of c) for different intensities. The solid, dashed, and dotted lines are for $I = 0.01I_0$, $I = 0.5I_0$, and $I = I_0$ respectively. The dark red regions correspond to higher population transfer.

the central peak originally at 777nm is a direct result of the dynamic Stark shift. As the pulse energy increases, the two photon resonance shifts to the blue and it is favorable to have a pi phase shift slightly blue detuned of the bare resonance. The growth of the peaks (located at about 777 nm and 800 nm) above the population transfer for an unshaped pulse can be explained by examining the integral of the off diagonal terms in Eq. 3.36. This is illustrated in Fig. 4.10.

Figure 4.10a) shows the integral

$$\int_{-\infty}^{\infty} \chi(t) \exp[i\alpha(t)]dt \tag{4.1}$$

as a function of intensity and π phase jump position. As expected, this shows agreement with the Fig. 4.9. The remaining panels show the temporal evolu-

tion of the atom-field phase parameter $\alpha(t)$, overlaid with the intensity profile of the pulse. All panels are for an intensity of $I = I_0$. The positions of the spectral phase flip are 775nm, 781nm, and 795nm for panels b), c), and d) respectively. These flip positions correspond to the two enhancement peaks and the minimum at 781 nm in the dotted line of Fig. 4.9d). For all three cases, the pulse intensity profile corresponds to a pulse pair, as a result of the step-like spectral phase. The graphs show that if $\alpha(t)$ evolves by an integer multiple (including zero) of 2π between pulses, then the population transfer is efficient because the excited state amplitude from both pulses can add constructively. However, if the evolution of $\alpha(t)$ is closer to π, then there is almost no population transfer, because the contributions from the two pulses add destructively. This illustrates how a given pulse parametrization which was originally motivated by frequency domain considerations for weak field excitation can be interpreted for the case of strong fields in the time domain using a phase matching picture.

With this, our study of non-resonant multiphoton transitions in a two level system is complete. We not only showed that in the strong field limit a time domain, phase matching picture is more useful, but also, we demonstrated that the perturbative weak field limit results are retrieved from our general formalism. Finally, the simple pulses used to study the transition can give us information about the level dynamics as the intensity increases. This could serve as a spectroscopic tool with strong fields.

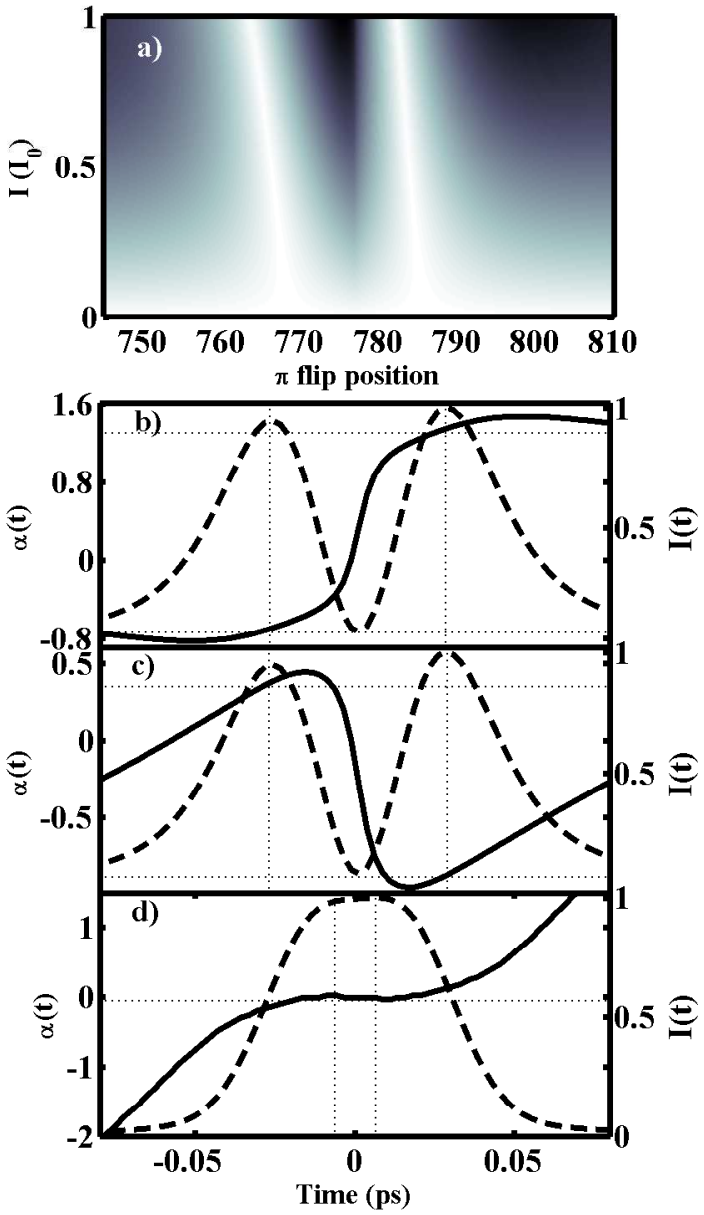

Figure 4.10: a) Calculation of the population transfer using the LHS of Eq.(3.37) as function of peak intensity (for an unshaped pulse) and π flip position. b), c), and d) evolution of $\alpha(t)$ (left axis, solid line) and $I(t)$ (right axis, dashed line) in time for different π phase flip positions (see text). All three are for the same pulse energy, corresponding to the minimum energy required for a π pulse, as defined by Eq. 3.37 with $\alpha(t) = 0$. The straight dotted lines mark the change of $\alpha(t)$ between the two maxima of $I(t)$. In a) the dark regions correspond to higher population transfer. I_0 is the peak intensity required for a π pulse (50fs FWHM) on the 3s-4s transition.

Chapter 5

Collective response to strong, ultrafast electric fields

The topic to be discussed here started as a curiosity and ended up as chapter of this thesis and as a published paper [34]. While maximizing the fluorescence signal for the $3p \rightarrow 3s$ transition, we noticed a very strong orange light coming out of the Na heat pipe oven. The next few sections is what followed after this *accident*. From a more general picture, the preceding chapter deals with the coherent control of single atoms through a TPA. In this chapter we will talk about how control, using the same process of two photon transition, differs when we target an ensemble of atoms. Furthermore, several recent papers which demonstrate and analyze control over atomic and molecular ensembles have generated discussion on the roles of collective vs single atom dynamics in the mechanisms underlying control [67, 68, 70–73]. This paper considers strong field control over spontaneous and stimulated emission from an ensemble of atoms and considers the differences in the yields in terms of single atom and collective dynamics.

5.1 Feedback control on a Sodium laser

The setup for this experiment has already been shown in Section 2.5. The differences from the single atom experiment (previous chapter) are that the spatial filtering system is not used (no pinhole) and that the signal used as fitness for the GA is the integral of this $\lambda \approx 589$nm (orange) *forward* scattered light. The detector we use in this case is a an unbiased slow-response photodiode. The reason for using a slow response photodiode is that when taking traces with the PMT the traces showed time durations that were at most as long as the detection capabilities in the lab (that is, $\approx$ 1ns). With

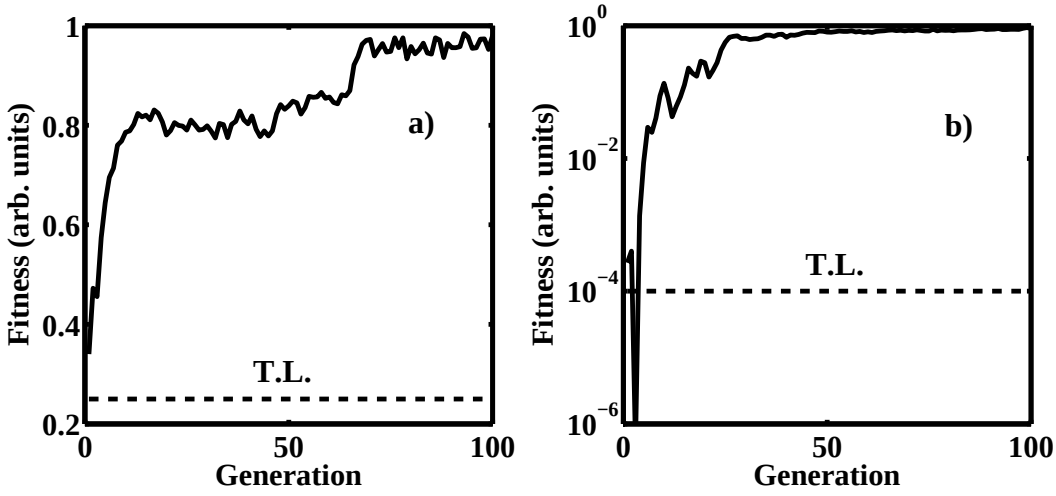

Figure 5.1: (a) Population transfer (as measured by florescence yield on the 3p-3s transition) as a function of generation. The dashed line indicates the yield for an unshaped (transform limited) laser pulse. (b) Stimulated emission yield vs generation. The dashed line shows the value for an unshaped laser pulse.

these settings we proceed to feedback onto the GA. The spontaneous emission is measured in the same way as depicted in the previous chapter and in Section 2.4.

Figure 5.1 shows the spontaneous and stimulated emission yields as a function of generation, when using our GA to optimize the measured light yield. Note that while the graphs are similar in many respects, the graph for the stimulated emission has a logarithmic ordinate axis. Whereas for the single atom response, we find enhancements of 3 to 4 compared to a TL pulse, for the stimulated emission, we measure improvements in the feedback signal of 3 to 4 *orders of magnitude* compared to an unshaped pulse. The central question that this chapter addresses is understanding the nature of the stimulated emission and why the increase in yield with pulse shape is dramatically larger than the increase in the single atom yield.

The simplest and most intuitive picture of why the stimulated emission gains are a dramatic function of pulse shape is that the stimulated emission yield is exponentially sensitive to the gain, which is proportional to the population of the excited state. In order to test this picture and rule out other explanations (such as parametric wave mixing in the atomic vapor), we performed detailed calculations of the collective atomic response and characterized

the stimulated emission pulses driven by an optimally shaped drive laser pulse.

5.2 The slowly varying density matrix for three level systems

Using the GA and our $\lambda_0 \approx 780$nm laser, we excite the ground state to the $4s$ via TPA. After this, the atoms decay and the system lases at $\lambda_0 = 589$nm. The excitation path is shown in Figure 5.2. From the figure, is clear that there are three fields and three levels to take into account. The fields are $\mathbf{E_L}$ for the pump at laser 780nm, $\mathbf{E_1(t)}$ for the field generated by the transition $4s \rightarrow 3p$ and $\mathbf{E_2(t)}$ for the field created by the decay of the $3p$ back to the ground state. The states to take into account are the ones just mentioned. The ground state $3s$, which we will label here 1 or g, the $4s$ labeled e or 2, and the $3p$ labeled as i (intermediate) or 3.

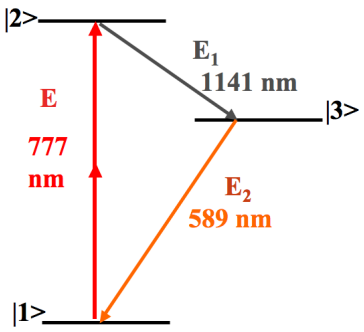

Figure 5.2: Excitation and decay path after the TPA.

The reason for changing the state labeling is just a practical matter. The number labeling follows the population $1 \rightarrow 2 \rightarrow 3$, which is the same as $g \rightarrow e \rightarrow i$ or, $3s \rightarrow 4s \rightarrow 3p$. This means that fields $\mathbf{E_1(t)}$ and $\mathbf{E_2(t)}$ are resonant with transitions $e \rightarrow i$ and $i \rightarrow g$ respectively. The wavelengths of this transition are $\lambda_1 = 1141$nm and $\lambda_2 = 589$nm. Formally, for the field that couples $2 \rightarrow 3$,

$$\mathbf{E_1}(t) = \frac{1}{2}\varepsilon_1(t)e^{-\imath\omega_1 t}\hat{\varepsilon_1} + c.c., \tag{5.1}$$

with ω_1 the field's frequency, $\hat{\varepsilon}_1$ is the polarization vector,

$$\varepsilon_1(t) = \varepsilon_1\sqrt{g_1(t)}e^{\imath\varphi_1(t)}, \tag{5.2}$$

$\sqrt{g_1(t)}$ is the field's 1 envelope, ε_1 is the field's strength, and $\varphi_1(t)$ the field's phase.

And for the field coupling $3 \rightarrow 1$,

$$\mathbf{E_2}(t) = \frac{1}{2}\varepsilon_2(t)e^{-\imath\omega_2 t}\hat{\varepsilon_2} + c.c., \tag{5.3}$$

where ω_2 is the field's frequency, $\hat{\varepsilon}_2$ is the polarization vector,

$$\varepsilon_2(t) = \varepsilon_2 \sqrt{g_2(t)} e^{\imath \varphi_2(t)}, \tag{5.4}$$

following the same notation.

The ground and excited state are directly linked through the pump laser via Hamiltonian in Eq. 3.30,

$$\hat{\mathbf{H}}(t) = \hbar \begin{pmatrix} \omega_g^{(s)}(t) & \chi^*(t) e^{-\imath \Delta t} \\ \chi(t) e^{\imath \Delta t} & \omega_e^{(s)}(t) \end{pmatrix}. \tag{5.5}$$

Coupling to/from the intermediate level occurs through a simple dipole interaction,

$$\langle j | \hat{H}_{AF} | i \rangle = -\frac{1}{2} \mu_{ji} \left(\varepsilon_{1,2}(t) e^{-\imath w_{1,2} t} + c.c \right) \tag{5.6}$$

with $j = e, g$. Then the equation for the slowly varying amplitude $a_i(t)$ becomes,

$$i\hbar \dot{a}_i(t) = a_e(t) e^{-i\omega_{ei} t} \langle i | \hat{H}_{AF} | e \rangle + a_g(t) e^{-i\omega_{gi} t} \langle i | \hat{H}_{AF} | g \rangle. \tag{5.7}$$

The latter means that the amplitudes a_e, a_g change by an extra amount proportional to the dipole coupling to the intermediate state. The three levels coupled equations expand to,

$$\begin{aligned} i\hbar \dot{a}_i(t) &= -a_e(t) e^{-i\omega_{ei} t} \frac{1}{2} \mu_{ie} \left(\varepsilon_1(t) e^{-\imath w_1 t} + c.c \right) - \\ &- a_g(t) e^{-i\omega_{gi} t} \frac{1}{2} \mu_{ig} \left(\varepsilon_2(t) e^{-\imath w_2 t} + c.c \right) \qquad (5.8) \\ i\hbar \dot{a}_g(t) &= \omega_g^{(s)}(t) a_g(t) + \chi^*(t) e^{-\imath \Delta t} a_e(t) \\ &\quad -a_i(t) e^{i\omega_{gi} t} \frac{1}{2} \mu_{gi} \left(\varepsilon_2(t) e^{-\imath w_2 t} + c.c \right) \qquad (5.9) \\ i\hbar \dot{a}_e(t) &= \chi(t) e^{\imath \Delta t} a_g(t) + \omega_e^{(s)}(t) a_e(t) \\ &\quad -a_i(t) e^{i\omega_{ei} t} \frac{1}{2} \mu_{ei} \left(\varepsilon_1(t) e^{-\imath w_1 t} + c.c \right) \qquad (5.10) \end{aligned}$$

Using again the RWA, we keep only the terms that are resonant with the

fields $\mathbf{E_1}$ and $\mathbf{E_2}$,

$$\begin{aligned} i\hbar\dot{a}_i(t) &= -a_e(t)e^{-i\Delta_{ei}t}\frac{1}{2}\mu_{ie}\varepsilon_1^*(t) - a_g(t)e^{i\Delta_{ig}t}\frac{1}{2}\mu_{ig}\varepsilon_2(t) && (5.11)\\ i\hbar\dot{a}_g(t) &= \omega_g^{(s)}(t)a_g(t) + \chi^*(t)e^{-\imath\Delta t}a_e(t) \\ &\quad -a_i(t)e^{-i\Delta_{ig}t}\frac{1}{2}\mu_{gi}\varepsilon_2^*(t) && (5.12)\\ i\hbar\dot{a}_e(t) &= \chi(t)e^{\imath\Delta t}a_g(t) + \omega_e^{(s)}(t)a_e(t) \\ &\quad -a_i(t)e^{i\Delta_{ei}t}\frac{1}{2}\mu_{ei}\varepsilon_1(t), && (5.13)\end{aligned}$$

with detunings $\Delta_{ig} = \omega_{ig} - \omega_1$ and $\Delta_{ei} = \omega_{ei} - \omega_2$ defined in the same way as before.

The two level Hamiltonian (Eq. 5.5) expands to,

$$\hat{\mathbf{H}}(t) = \hbar \begin{pmatrix} \omega_g^{(s)}(t) & \chi^*(t)e^{\imath-\Delta t} & -e^{-i\Delta_{ig}t}\frac{\mu_{gi}}{2\hbar}\varepsilon_2^*(t) \\ \chi(t)e^{\imath\Delta t} & \omega_e^{(s)}(t) & -e^{i\Delta_{ei}t}\frac{\mu_{ei}}{2\hbar}\varepsilon_1(t) \\ -e^{i\Delta_{ig}t}\frac{\mu_{ig}}{2\hbar}\varepsilon_2(t) & -e^{-i\Delta_{ei}t}\frac{\mu_{ie}}{2\hbar}\varepsilon_1^*(t) & 0. \end{pmatrix} \quad (5.14)$$

Care should be taken here to distinguish this Hamiltonian from the one in Eq. 3.45 since in that case only one field is present. In principle the $7p$ state should be considered here as well, but since the GA solutions yield very little contribution to the population of this state, we can neglect it here.

5.2.1 Three levels density matrix

Since stimulated emission is initialized by decay processes that are incoherent, the density matrix formalism developed in Section 3.10 will be of use here. Let us remember that the slowly varying density matrix $\mathbf{Q}$ satisfies the temporal evolution equation,

$$i\hbar\frac{\partial}{\partial t}Q(t) = \left[\hat{\mathbf{H}}, Q\right]. \quad (5.15)$$

With the density matrix including now a third level,

$$\mathbf{Q} = \begin{pmatrix} Q_{11} & Q_{12} & Q_{13} \\ Q_{21} & Q_{22} & Q_{23} \\ Q_{31} & Q_{32} & Q_{33} \end{pmatrix}, \quad (5.16)$$

the equations of motion for $\mathbf{Q}$ become,

$$
\begin{aligned}
\imath\hbar\frac{\partial}{\partial t}Q_{11} &= \hbar\chi^*(t)e^{\imath-\Delta t}Q_{21} - \hbar\chi(t)e^{\imath\Delta t}Q_{12} - \frac{\mu_{gi}}{2}\varepsilon_2^*(t)e^{-i\Delta_{ig}t}Q_{31} + \\
&+ \frac{\mu_{ig}}{2}\varepsilon_2(t)e^{i\Delta_{ig}t}Q_{13} \qquad (5.17)\\
\imath\hbar\frac{\partial}{\partial t}Q_{22} &= \hbar\chi(t)e^{\imath\Delta t}Q_{12} - \hbar\chi^*(t)e^{\imath-\Delta t}Q_{21} - \frac{\mu_{ei}}{2}\varepsilon_1(t)e^{i\Delta_{ei}t}Q_{32} + \\
&+ \frac{\mu_{ie}}{2}\varepsilon_1^*(t)e^{-i\Delta_{ei}t}Q_{23} \qquad (5.18)\\
\imath\hbar\frac{\partial}{\partial t}Q_{33} &= -\frac{\mu_{ig}}{2}\varepsilon_2(t)e^{i\Delta_{ig}t}Q_{13} - \frac{\mu_{ie}}{2}\varepsilon_1^*(t)e^{-i\Delta_{ei}t}Q_{23} + \frac{\mu_{gi}}{2}\varepsilon_2^*(t)e^{-i\Delta_{ig}t}Q_{31} + \\
&+ \frac{\mu_{ei}}{2}\varepsilon_1(t)e^{i\Delta_{ei}t}Q_{32} \qquad (5.19)\\
i\hbar\frac{\partial}{\partial t}Q_{12} &= \hbar\chi^*(t)e^{\imath-\Delta t}(Q_{22}-Q_{11}) - \hbar Q_{12}\delta_\omega^{(s)}(t) - \frac{\mu_{gi}}{2}\varepsilon_2^*(t)e^{-i\Delta_{ig}t}Q_{32} + \\
&+ \frac{\mu_{ie}}{2}\varepsilon_1^*(t)e^{-i\Delta_{ei}t}Q_{13} \qquad (5.20)\\
i\hbar\frac{\partial}{\partial t}Q_{21} &= \hbar\chi(t)e^{\imath\Delta t}(Q_{11}-Q_{22}) + \hbar Q_{21}\delta_\omega^{(s)}(t) - \frac{\mu_{ei}}{2}\varepsilon_1(t)e^{i\Delta_{ei}t}Q_{31} + \\
&+ \frac{\mu_{ig}}{2}\varepsilon_2(t)e^{i\Delta_{ig}t}Q_{23} \qquad (5.21)\\
i\hbar\frac{\partial}{\partial t}Q_{13} &= \omega_g^{(s)}(t)Q_{13} + \chi^*(t)e^{\imath-\Delta t}Q_{23} - \frac{\mu_{gi}}{2}\varepsilon_2^*(t)e^{-i\Delta_{ig}t}Q_{33} + \\
&+ \frac{\mu_{gi}}{2}\varepsilon_2^*(t)e^{-i\Delta_{ig}t}Q_{11} + \frac{\mu_{ei}}{2}\varepsilon_1(t)e^{i\Delta_{ei}t}Q_{12} \qquad (5.22)\\
i\hbar\frac{\partial}{\partial t}Q_{23} &= \chi(t)e^{\imath\Delta t}Q_{13} + \omega_e^{(s)}(t)Q_{23} - \frac{\mu_{ei}}{2}\varepsilon_1(t)e^{i\Delta_{ei}t}Q_{33} + \\
&+ \frac{\mu_{gi}}{2}\varepsilon_2^*(t)e^{-i\Delta_{ig}t}Q_{21} + \frac{\mu_{ei}}{2}\varepsilon_1(t)e^{i\Delta_{ei}t}Q_{22} \qquad (5.23)\\
Q_{31} &= Q_{13}^* \qquad (5.24)\\
Q_{32} &= Q_{23}^*. \qquad (5.25)
\end{aligned}
$$

These equations give the probability for the atom to be in the ground state $3s$ ($Q_{11}(t)$), in the excited state $4s$ ($Q_{22}(t)$), or in the intermediate state $3p$ ($Q_{33}(t)$) at any given time for fields $\mathbf{E_L}(t)$, $\mathbf{E_1}(t)$, and $\mathbf{E_2}(t)$. However, $\mathbf{E_1}(t)$ and $\mathbf{E_2}(t)$ depend on the atomic *coherences* Q_{23} and Q_{13}, which means that the last set of equations, must be solved simultaneously with the Maxwell equations in the atomic medium.

5.3 Polarization of a pulsed electric field in the presence of TPA

Since the Na atomic vapor is a dielectric medium, we need to find the polarization at the frequency of the three fields of importance. Polarization comes from the dipole moment of the entire system.

$$\mathbf{P_T} = N\langle\Psi|\hat{\mu}|\Psi\rangle \tag{5.26}$$

The relevant polarizations at ω_0, ω_1, and ω_2 are,

$$\begin{aligned}
\mathbf{P}(\mathbf{r},t) &= P(\mathbf{r},t)e^{-i\omega_0 t+i\mathbf{k}\cdot\mathbf{r}} + P^*(\mathbf{r},t)e^{i\omega_0 t-i\mathbf{k}\cdot\mathbf{r}} && (5.27)\\
\mathbf{P_1}(\mathbf{r},t) &= P_1(\mathbf{r},t)e^{-i\omega_1 t+i\mathbf{k_1}\cdot\mathbf{r}} + P_1^*(\mathbf{r},t)e^{i\omega_1 t-i\mathbf{k_1}\cdot\mathbf{r}} && (5.28)\\
\mathbf{P_2}(\mathbf{r},t) &= P_2(\mathbf{r},t)e^{-i\omega_2 t+i\mathbf{k_2}\cdot\mathbf{r}} + P_2^*(\mathbf{r},t)e^{i\omega_2 t-i\mathbf{k_2}\cdot\mathbf{r}} && (5.29)
\end{aligned}$$

In principle we can split Eq. 5.26 in the three contributing terms and find the solutions for the polarization by separating the variables in time and space. This means that for a given value of $\mathbf{r}$ we can write,

$$\begin{aligned}
P(t)e^{-i\omega_0 t} &= N\langle\Psi(t)|\hat{\mu}|\Psi(t)\rangle && (5.30)\\
P_1(t)e^{-i\omega_1 t} &= N\langle\Psi_1(t)|\hat{\mu}|\Psi_1(t)\rangle && (5.31)\\
P_2(t)e^{-i\omega_2 t} &= N\langle\Psi_2(t)|\hat{\mu}|\Psi_2(t)\rangle && (5.32)
\end{aligned}$$

Where $\Psi_1(t)\rangle, \Psi_2(t)\rangle$,and $\Psi(t)\rangle$ are the wavefunctions for the atom-field interaction with fields $\mathbf{E_1}$, $\mathbf{E_2}$, and $\mathbf{E}$ respectively. Since the difference in frequency between all the fields is large, each field couples only one pair of levels. This means we can divide the problem in three subproblems, each one dictated by the relevant atomic transition. Each of these subproblems involve finding the wave function and with it, the polarization.

5.3.1 $\mathbf{E_1}$ and $\mathbf{E_2}$ polarizations

Transitions $2 \rightarrow 3$ and $3 \rightarrow 1$ involve a single photon. This means that the interaction (and therefore the polarization) occurs through a simple dipole moment. The wave function and polarization are,

$$\begin{aligned}
\Psi_1(t)\rangle &= a_e(t)e^{-i\omega_e t}|e> + a_i(t)e^{-i\omega_i t}|i> && (5.33)\\
\langle\Psi_1|\hat{\mu}|\Psi_1\rangle &= a_i^*(t)a_e(t)e^{-i\omega_{ei}t}\mu_{ie} + c.c, && (5.34)
\end{aligned}$$

for the $e \rightarrow i$ transition and,

$$\begin{aligned} \Psi_2(t)\rangle &= a_g(t)e^{-i\omega_g t}|g> + a_i(t)e^{-i\omega_i t}|i> & (5.35) \\ \langle\Psi_2|\hat{\mu}|\Psi_2\rangle &= a_i^*(t)a_g(t)e^{i\omega_{ig}t}\mu_{ie} + c.c & (5.36) \end{aligned}$$

for the $i \rightarrow g$ one. Polarizations, after taking only terms with frequencies close to ω_1, ω_2 (RWA), yield,

$$\begin{aligned} P_1(t) &= Na_i^*(t)a_e(t)e^{-i\Delta_{ei}t}\mu_{ie} & (5.37) \\ P_2(t) &= Na_i(t)a_g^*(t)e^{i\Delta_{ig}t}\mu_{gi}. & (5.38) \end{aligned}$$

5.3.2 Multiphoton polarization.

Unfortunately, polarization in a medium due to a multiphoton transition is not as simple. Furthermore, the treatment of this case seems to be lacking in the strong field regime. Similar formalisms, in the presence of Raman transitions have been proposed [67, 68]. Here we outline the theoretical details for obtaining the polarization in a TPA medium interacting with a strong, ultrafast electric field beyond perturbation theory. It follows very closely the theoretical model used to derive the TPA Hamiltonian Eq. 3.30. The laser field couples states a_g, a_e and off resonant a_m, therefore the wave function is,

$$\Psi(t)\rangle = a_e(t)e^{-i\omega_e t}|e> + a_g(t)e^{-i\omega_g t}|g> + \sum_m a_m(t)e^{-\imath\omega_m t}|m\rangle, \quad (5.39)$$

and again the polarization can be expressed as,

$$\langle\Psi|\hat{\mu}|\Psi\rangle = \sum_m a_m^*(t)a_g(t)e^{-i\omega_{gm}t}\mu_{mg} + \sum_m a_m^*(t)a_e(t)e^{-i\omega_{em}t}\mu_{me} + c.c. \quad (5.40)$$

At this point we can substitute $a_m(t)$ obtained in equation 3.21 (after the adiabatic elimination),

$$\begin{aligned} a_m(t) &= \frac{\mu_{mg}}{2\hbar}a_g(t)e^{\imath\omega_m t}\left[\frac{\varepsilon(t)e^{-i(\omega_g+\omega_0 t)}}{\omega_{mg}-\omega_0} + \frac{\varepsilon^*(t)e^{-i(\omega_g-\omega_0 t)}}{\omega_{mg}+\omega_0}\right] + \\ &\quad \frac{\mu_{me}}{2\hbar}a_e(t)e^{\imath\omega_m t}\left[\frac{\varepsilon(t)e^{-i(\omega_e+\omega_0 t)}}{\omega_{me}-\omega_0} + \frac{\varepsilon^*(t)e^{-i(\omega_e-\omega_0 t)}}{\omega_{me}+\omega_0}\right], \quad (5.41) \end{aligned}$$

with which the bracket in Eq. 5.40 becomes,

$$\begin{aligned}
\langle\Psi|\hat{\mu}|\Psi\rangle &= \sum_m \left[a_g(t)e^{-i\omega_{gm}t}\mu_{mg} + a_e(t)e^{-i\omega_{em}t}\mu_{me}\right] \times \\
&\times\ e^{-\imath\omega_m t}\left\{\frac{\mu^*_{mg}}{2\hbar}a^*_g(t)\left[\frac{\varepsilon^*(t)e^{i(\omega_g+\omega_0 t)}}{\omega_{mg}-\omega_0} + \frac{\varepsilon(t)e^{i(\omega_g-\omega_0 t)}}{\omega_{mg}+\omega_0}\right] + \right. \\
&+\ \left.\frac{\mu^*_{me}}{2\hbar}a^*_e(t)\left[\frac{\varepsilon^*(t)e^{i(\omega_e+\omega_0 t)}}{\omega_{me}-\omega_0} + \frac{\varepsilon(t)e^{i(\omega_e-\omega_0 t)}}{\omega_{me}+\omega_0}\right]\right\} + \\
&+\ \sum_m \left[a^*_g(t)e^{i\omega_{gm}t}\mu^*_{mg} + a^*_e(t)e^{i\omega_{em}t}\mu^*_{me}\right] \times \\
&\times\ e^{\imath\omega_m t}\left\{\frac{\mu_{mg}}{2\hbar}a_g(t)\left[\frac{\varepsilon(t)e^{-i(\omega_g+\omega_0 t)}}{\omega_{mg}-\omega_0} + \frac{\varepsilon^*(t)e^{-i(\omega_g-\omega_0 t)}}{\omega_{mg}+\omega_0}\right] + \right. \\
&+\ \left.\frac{\mu_{me}}{2\hbar}a_e(t)\left[\frac{\varepsilon(t)e^{-i(\omega_e+\omega_0 t)}}{\omega_{me}-\omega_0} + \frac{\varepsilon^*(t)e^{-i(\omega_e-\omega_0 t)}}{\omega_{me}+\omega_0}\right]\right\} \qquad (5.42)
\end{aligned}$$

Since the complex polarization Eq. 5.30 oscillates at frequency ω_0, in order to apply the RWA we need to extract terms that oscillate at $-\omega_0$, that is, terms that contain $e^{-i\omega_0 t}$ (look at equations 5.32). Also we can keep terms that oscillate at $\pm\Delta$, $\Delta = \omega_e - \omega_g - 2\omega_0 = \omega_{em} - \omega_{gm} - 2\omega_0$. Multiplying Eq. 5.42 by $e^{-i\omega_0 t}$ and applying the RWA as mentioned, we arrive at,

$$\begin{aligned}
e^{i\omega_0 t}\langle\Psi|\hat{\mu}|\Psi\rangle &= \sum_m \left[|a_g|^2(t)\frac{|\mu_{mg}|^2}{2\hbar}\frac{\varepsilon(t)}{\omega_{mg}+\omega_0} + |a_e|^2(t)\frac{|\mu_{me}|^2}{2\hbar}\frac{\varepsilon(t)}{\omega_{me}+\omega_0}\right] + \\
&+\ \sum_m e^{i\omega_0}a_e(t)e^{-i\omega_{em}t}\mu_{me}\frac{\mu^*_{mg}}{2\hbar}a^*_g(t)\frac{\varepsilon^*(t)e^{i(\omega_{gm}+\omega_0 t)}}{\omega_{mg}-\omega_0} + \\
&+\ \sum_m \left[|a_g|^2(t)\frac{|\mu_{mg}|^2}{2\hbar}\frac{\varepsilon(t)}{\omega_{mg}-\omega_0} + |a_e|^2(t)\frac{|\mu_{me}|^2}{2\hbar}\frac{\varepsilon(t)}{\omega_{me}-\omega_0}\right] + \\
&+\ \sum_m e^{i\omega_0}a^*_g(t)e^{i\omega_{gm}t}\mu^*_{mg}\frac{\mu_{me}}{2\hbar}a_e(t)\frac{\varepsilon^*(t)e^{-i(\omega_{em}-\omega_0 t)}}{\omega_{me}+\omega_0}. \qquad (5.43)
\end{aligned}$$

By comparing this last equation to Eq. 3.25 we can see that the definitions of the DSS, $\omega^{(s)}_{\{e,g\}}$, and two photon coupling, $\chi(t)$, introduced earlier are useful. With these definitions we finally arrive to the TPA polarization,

$$P(t) = 2N\hbar\left[|a_g|^2(t)\omega^{(s)}_g\varepsilon(t) + |a_e|^2(t)\omega^{(s)}_g\varepsilon(t) + 2a_e(t)a^*_g(t)e^{-i\Delta t}\chi\varepsilon^*(t))\right]. \qquad (5.44)$$

Here we can see that, because $\omega^{(s)}_{\{e,g\}}$ and $\chi(t)$ are of the same order of magni-

tude, the medium's response to a strong field is not only through the non-linear coupling $\chi(t)$, but it also involves the DSS.

5.3.3 Polarization in terms of density matrix

The polarizations obtained above can be put in terms of the density matrix. Using again the numbered definition for the $3s$, $4s$, and $3p$, $g = 1$, $e = 2$, $i = 3$. Fields $\mathbf{E_1}$ couples levels $2 \rightarrow 3$ and $\mathbf{E_2}$ couples levels $3 \rightarrow 1$,

$$\begin{aligned} P(t) &= 2N\hbar \left[Q_{11}\omega_g^{(s)}\varepsilon(t) + Q_{22}\omega_e^{(s)}\varepsilon(t) + 2Q_{21}\chi e^{-i\Delta t}\varepsilon^*(t) \right] \\ P_1(t) &= NQ_{23}e^{-i\Delta_{ei}t}\mu_{ie} \\ P_2(t) &= NQ_{31}e^{i\Delta_{ig}t}\mu_{gi} \end{aligned} \tag{5.45}$$

Using these last set of equations combined with the equations for the temporal evolution of $\boldsymbol{Q}$ we can analyze how both the fields and wave function evolve in time. However, as mentioned above, this result is at a given position $\boldsymbol{r}$ and, as of yet, we have no information on the functional dependence of polarizations and wave functions with position.

5.4 Propagation.

The starting point for taking into account propagation effects is to study how the fields propagate. This involves solving the Maxwell equations in a dielectric medium with polarization $\boldsymbol{P_T}(r,t)$ given in Eq. 5.26,

$$\left(\nabla^2 - \frac{1}{v^2}\frac{\partial^2}{\partial t^2} \right) \mathbf{E}(z,t) = \frac{1}{\epsilon_o c^2}\frac{\partial^2}{\partial t^2}\mathbf{P}(r,t) \tag{5.46}$$

With vector fields,

$$\mathbf{E}(\mathbf{r},t) = E(\mathbf{r},t)e^{-\imath\omega_0 t + i\mathbf{k}\cdot\mathbf{r}} + E^*(\mathbf{r},t)e^{\imath\omega_0 t - i\mathbf{k}\cdot\mathbf{r}} \tag{5.47}$$

and polarizations,

$$\mathbf{P}(\mathbf{r},t) = P(\mathbf{r},t)e^{-\imath\omega_0 t + i\mathbf{k}\cdot\mathbf{r}} + P^*(\mathbf{r},t)e^{\imath\omega_0 t - i\mathbf{k}\cdot\mathbf{r}}. \tag{5.48}$$

For 1D geometry, the Laplacian reduces to a single second derivative. The time and space second derivatives in the left hand side of Eq. 5.46 can be reduced to simple derivatives. Spatially this is justified due to the fact that the variation of the field, along the propagation axis is smooth. In time, second

derivatives can be dropped using a slowly varying envelope approximation. This is equivalent to expand, the second derivative of the field up to the first order. With these approximations, the left hand side on Eq. 5.46 reduces to,

$$2ike^{-i(\omega t-k\dot{r})}\left(\frac{\partial}{\partial z}+\frac{1}{v}\frac{\partial}{\partial t}\right)\varepsilon(z,t). \tag{5.49}$$

Expanding the right hand side yields,

$$\frac{\partial^2}{\partial t^2}\mathbf{P}(r,t)=e^{-i(\omega t-k\dot{r})}\frac{\partial^2}{\partial t^2}P(z,t)-\omega^2e^{-i(\omega t-k\dot{r})}P(z,t)-2i\omega e^{-i(\omega t-k\dot{r})}\frac{\partial}{\partial t}P(z,t). \tag{5.50}$$

Making use of the slowly varying envelope approximation,

$$\omega^2P(z,t)\gg\omega\frac{\partial}{\partial t}P(z,t)\gg\frac{\partial^2}{\partial t^2}P(z,t), \tag{5.51}$$

we obtain for the right hand side of 5.46,

$$\frac{\partial^2}{\partial t^2}P(z,t)=-\omega^2e^{-i(\omega t-k\dot{r})} \tag{5.52}$$

These two results yield the so called 1D reduced Maxwell equation [67, 68, 74],

$$\frac{\partial}{\partial z}\mathbf{E}(z,t)+\frac{1}{c}\frac{\partial}{\partial t}\mathbf{E}(z,t)=\frac{1}{2\epsilon_0c}\frac{\partial}{\partial t}\mathbf{P}(z,t) \tag{5.53}$$

assuming the speed of light in the medium is c, and with the derivative is done only on the exponential (again according to the slowly varying slope approximation).

In the local time frame this equation reduces to,

$$\frac{\partial}{\partial z}E(z,t)=\imath\frac{\omega}{2\epsilon_0c}P(z,t) \tag{5.54}$$

which is valid for all fields.

Now we finally are in the position to express the equations governing the spatio-temporal evolution of the atom's quantum state and the fields detected experimentally. Amplitudes are given by,

$$\frac{\partial}{\partial t}Q_{11} = -i\left[\chi(z,t)e^{-i\Delta t}Q_{21} - \chi^*(z,t)e^{i\Delta t}Q_{21}^* - \frac{\mu_{gi}}{2\hbar}\varepsilon_2^*(z,t)e^{-i\Delta_{ig}t}Q_{31} + \right.$$
$$\left. + \frac{\mu_{ig}}{2\hbar}\varepsilon_2(z,t)e^{i\Delta_{ig}t}Q_{31}^*\right] \quad (5.55a)$$

$$\frac{\partial}{\partial t}Q_{22} = -i\left[\chi^*(z,t)e^{i\Delta t}Q_{21}^* - \chi(z,t)e^{-i\Delta t}Q_{21} - \frac{\mu_{ei}}{2\hbar}\varepsilon_1(z,t)e^{i\Delta_{ei}t}Q_{32} + \right.$$
$$\left. + \frac{\mu_{ie}}{2\hbar}\varepsilon_1^*(z,t)e^{-i\Delta_{ei}t}Q_{32}^*\right] \quad (5.55b)$$

$$\frac{\partial}{\partial t}Q_{33} = -i\left[\frac{\mu_{gi}}{2\hbar}\varepsilon_2^*(z,t)e^{-i\Delta_{ig}t}Q_{31} - \frac{\mu_{ig}}{2\hbar}\varepsilon_2(z,t)e^{i\Delta_{ig}t}Q_{31}^* + \right.$$
$$\left. + \frac{\mu_{ei}}{2\hbar}\varepsilon_1(z,t)e^{i\Delta_{ei}t}Q_{32}\frac{\mu_{ie}}{2\hbar}\varepsilon_1^*(z,t)e^{-i\Delta_{ei}t}Q_{32}^*\right] \quad (5.55c)$$

$$\frac{\partial}{\partial t}Q_{21} = -i\left[\chi^*(z,t)e^{i\Delta t}(Q_{11}-Q_{22}) + Q_{21}\delta_\omega^{(s)}(z,t) - \frac{\mu_{ei}}{2\hbar}\varepsilon_1(z,t)e^{i\Delta_{ei}t}Q_{31} + \right.$$
$$\left. + \frac{\mu_{ig}}{2\hbar}\varepsilon_2(z,t)e^{i\Delta_{ig}t}Q_{32}^*\right] \quad (5.55d)$$

$$\frac{\partial}{\partial t}Q_{31} = i\left[\omega_g^{(s)}(z,t)Q_{31} + \chi^*(z,t)e^{i\Delta t}Q_{32} + \frac{\mu_{ig}}{2\hbar}\varepsilon_2(z,t)e^{i\Delta_{ig}t}(Q_{11}-Q_{33}) + \right.$$
$$\left. + \frac{\mu_{ie}}{2\hbar}\varepsilon_1^*(z,t)e^{-i\Delta_{ei}t}Q_{21}\right] \quad (5.55e)$$

$$\frac{\partial}{\partial t}Q_{32} = i\left[\omega_e^{(s)}(z,t)Q_{32} + \chi(z,t)e^{-i\Delta t}Q_{31} + \frac{\mu_{ie}}{2\hbar}\varepsilon_1^*(z,t)e^{-i\Delta_{ei}t}(Q_{22}-Q_{33}) + \right.$$
$$\left. + \frac{\mu_{ig}}{2\hbar}\varepsilon_2(z,t)e^{i\Delta_{ig}t}Q_{21}^*\right] \quad (5.55f)$$

with fields evolving according to,

$$\frac{\partial}{\partial z}\varepsilon(z,t) = 2\hbar\imath\frac{N\omega_0}{2\epsilon_0 c}\left[Q_{11}(z,t)\omega_g^{(s)}\varepsilon(z,t) + Q_{22}(z,t)\omega_e^{(s)}\varepsilon(z,t) + \right.$$
$$\left. + 2Q_{21}(z,t)\chi e^{-i\Delta t}\varepsilon^*(z,t)\right] \quad (5.56a)$$

$$\frac{\partial}{\partial z}\varepsilon_1(z,t) = \imath\frac{N\omega_1}{2\epsilon_0 c}Q_{32}^*(z,t)\mu_{ie}e^{-i\Delta_{ei}t} \quad (5.56b)$$

$$\frac{\partial}{\partial z}\varepsilon_2(z,t) = \imath\frac{N\omega_2}{2\epsilon_0 c}Q_{31}(z,t)\mu_{gi}e^{i\Delta_{ig}t}. \quad (5.56c)$$

Note that we have used here the notation $Q_{ij} = Q_{ij}(z,t)$ since now all the amplitudes depend on the propagation variable z and on time. For simplicity the z, t dependence has been omitted in Eqs. 5.55.

The above equations consist of eight coupled, complex differential equations. A closer look will reveal that the the space evolution is dictated by the fields, whereas the time evolution is in the density matrix. This allows us

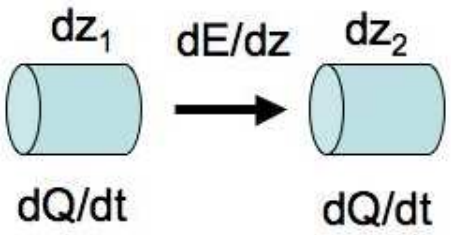

Figure 5.3: Scheme for integrating couple differential equations Eqs. 5.55 and Eqs. 5.56. At each position z_i equations for $\boldsymbol{Q}(z_i, t)$ are solved, to propagate to the next $z_{i+1} = z_i + dz$ position, the fields equations are solved to obtain $\varepsilon(z_{i+1}, t)$, using as coherences the calculated $\boldsymbol{Q}(z_i)$.

to separate the differential equations in two for numerical integrations. One part solves the time equations Eqs. 5.55 and the other part is responsible for propagating the fields in space Eqs. 5.56. This is schematically shown in Figure 5.3. This algorithm basically assumes that the fields are constant in a small region dz, and that coherences inside the medium *interact* through the existing fields. The integration in time is done using the same 4^{th} order Runge Kutta mentioned before and the space equations were integrated with a first order linear integration $\Delta\varepsilon = \Delta z \partial\varepsilon/\partial z$.

It should also be noted that there are no atomic decay factors involved. This means that if there is no other perturbative factor in the equations, no other light will be produced and only a two photon transition throughout the medium will happen. The stimulated emission process is initiated by a spontaneous decay, 4s $\rightarrow$ 3p, along the optical axis which is not included in the equations. This can be simulated by perturbing Q_{32} at $z = 0$ at some early time t' after the drive pulse. All parameters used in the simulations mimic the experimental conditions. The propagation length is 10cm and atomic Na densities can be as high as $\sim 5 \times 10^{21} m^{-3}$. The initial perturbation of Q_{32} was calculated taking into account the area of the interacting region, the density of atoms and the ratio of the pump laser ($\approx$ 35fs) to the lifetime of the $4s$ (38ns). Since the simulations are extremely CPU intensive, we used another optimization method. Again looking at Eqs. 5.55 and Eqs. 5.56, we notice that the atom density dependence only enters in the latter set of equations (Maxwell) in a linear form, the same way as the length of the propagation (assuming the density is constant). This allows us to shorten the simulations by changing the number of atoms the fields *sees* by just increasing the density. We checked this algorithm and it matches full simulations very nicely. Finally, since the time scale of the pump pulse (and therefore the population transfer

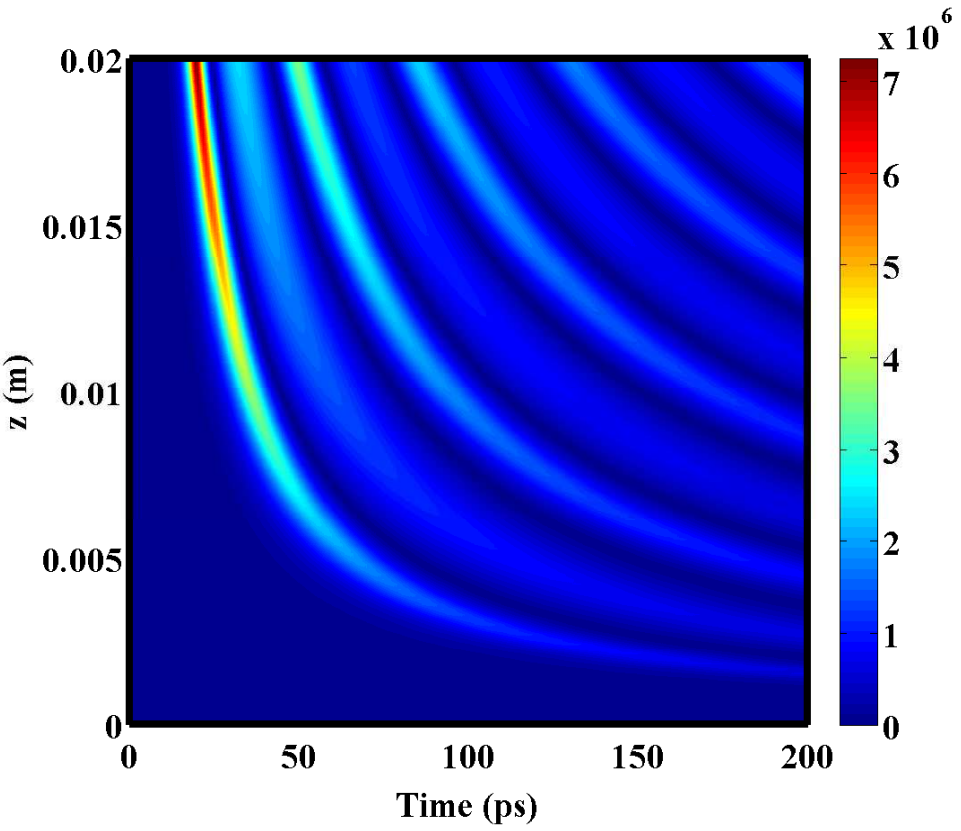

Figure 5.4: Simulation results for $E_2(z,t)$. Parameters for the simulation are $z = 10$cm, $T = 350$C ($T_{sim} = 400$C), $Q_{11} = 0.2$, and $Q_{22} = 0.8$.

to the $4s$ state) is extremely short compared to the atomic lifetimes, we can assume that the role of the strong pump field is to just excite the atoms. The latter allows us to ignore the relative coherences imparted by the pump laser to the different states. Again, this was verified with full calculations. The electric field $\varepsilon_2(z,t)$ after such calculation (with the parameters just mentioned) is shown in Figure 5.4.

The simulation temperature $T_{sim} = 400$C is chosen so that the *effective* length of the simulation is 10cm with a corresponding experimental temperature of $T = 350$C. The initial population distribution (after the pump pulse) is $Q_{11} = 0.2$ and $Q_{22} = 0.8$. The step size in z is $dz = 50\mu$m and the step size in time $dt = 40$fs. The value for the initial coherence $Q_{32} \approx 4.8 \times 10^{-6}$ which was taken into account to preserve the total population. The only reason why the $\varepsilon_2(z,t)$ is more important than the others is simply that it is the only measurable quantity in the lab. Although in principle we could measure the

1141nm light as well, detection at these frequencies is extremely expensive. In Figure 5.5 we show the full output of the calculations. The initial conditions are the same as for the previous graph.

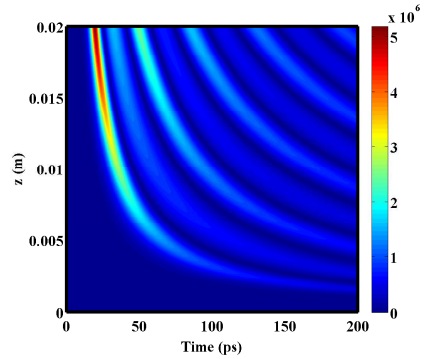

(a) $|\varepsilon_1(z,t)|$ (1141nm, $4s \rightarrow 3p$ transition

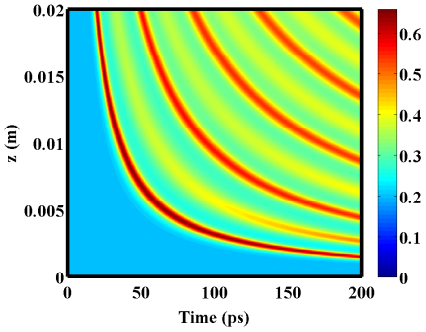

(b) $Q_{11}(z,t)$ ($3s$ probability)

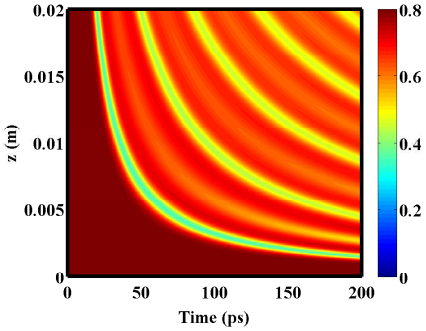

(c) $Q_{22}(z,t)$($4s$ probability)

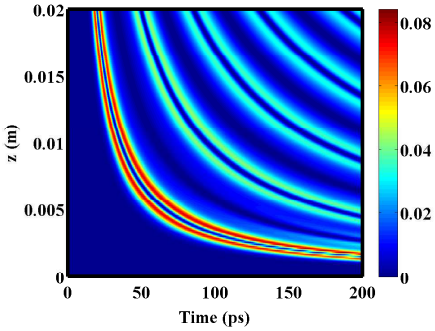

(d) $Q_{33}(z,t)$ ($3p$ probability)

Figure 5.5: Propagation simulation results after integrating Eqs. 5.55 and Eqs. 5.56. Parameters for the simulation are $z = 10$cm, $T = 350$C ($T_{sim} = 400$C), $Q_{11} = 0.2$, and $Q_{22} = 0.8$.

From Figure 5.5 we can see how the electric fields build up as they propagate through the vapor. As a matter of fact, at some point the ε_1 and ε_2 become so strong that the transitions $4s \rightarrow 3p$ and $3p \rightarrow 3s$ show Rabi oscillations. These are the oscillating trends we see in the 2D graphs above. The reason for this amplification is that when some small, initial set of Na atoms decay, emitting some photons, they only *see* excited atoms. Therefore, the most likely process to happen is stimulated emission from the $4s$ to the $3p$. This is similar to the well known Amplified Spontaneous Emission (ASE).

After this lengthy derivation, the next step is to compare the simulations

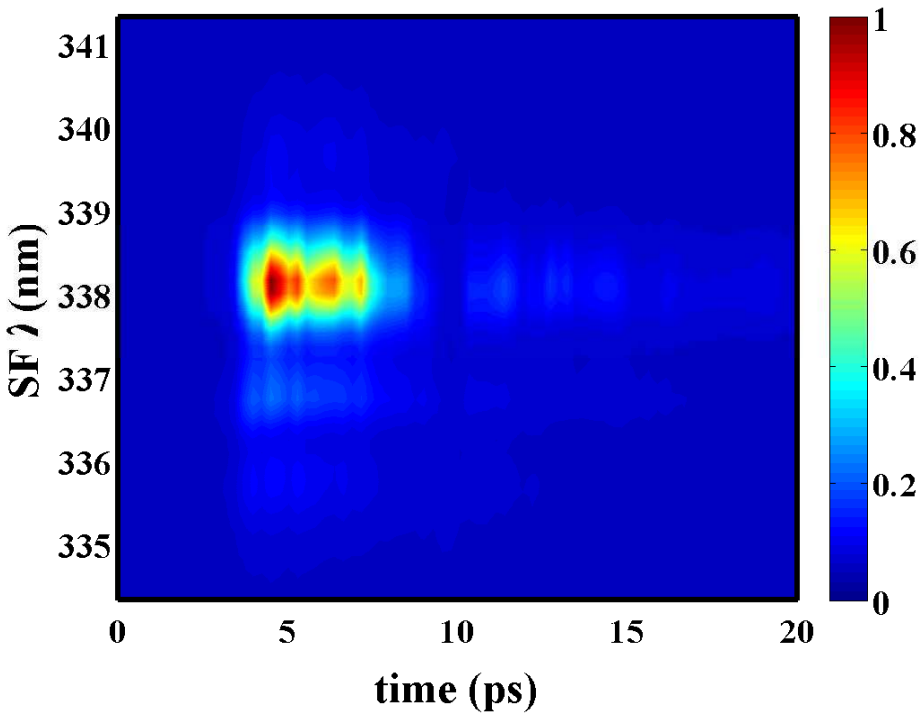

Figure 5.6: Sample cross correlation measurement of the 589nm forward light with the pump laser.

to experimental data.

5.5 Temporal characterization of the forward light: Yoked superfluorescence

After maximizing the forward light (589nm) signal using the GA, we proceed to its characterization. A typical measurement of the cross correlation of the 589nm forward light with the infrared pump pulse is shown in Figure 5.6. For this measurement we used the experimental setup outlined in Section 2.5. The spectral part of the measurement (y axis) is governed by the spectral properties of the pump laser, since it has roughly 30nm FWHM. However, the temporal part shows durations on the order of picoseconds. This is interesting, since it is a time scale that does not match either the atomic lifetimes (tens of nano seconds to micro seconds), nor the pump laser (femto seconds). Also it is a time scale that closely resembles the previous theoretical results. We also did

measurements at different Na vapor densities, controlled by changing the heat pipe temperature. Figure 5.7a shows the projection in time of the measured cross correlation for different vapor densities. It should be noted that since the cross correlation temporal width is much larger than the pump laser (by 2 or 3 orders of magnitude) this is equivalent to a measurement of the duration of the $\varepsilon_2(t)$ field. Shown in the graph are pulse durations for values of the densities of $3.16 \times 10^{21} m^{-3}$ (dashed line), $1.55 \times 10^{21} m^{-3}$ (dotted line), and $9.56 \times 10^{20} m^{-3}$ (solid line).

Although both, theory and experiment, yield pulsed electric fields of durations on the same order of magnitude, the temporal shape differs substantially. In order to fully reproduce the time characteristics of $\varepsilon_2(t)$, we need to consider fluctuations of the initial conditions when integrating Eqs. 5.55 and Eqs. 5.56. These fluctuations are in the initial population of the $4s$ level, due mainly to laser noise, and in the coherences. The latter is extremely important for Q_{32} and takes into account the fact that the initial decay from the $4s$ level, that seeds the entire process, occurs from different atoms in the interacting region. We follow earlier work in averaging over a Gaussian random distribution for this initialization [75–77]. The output fields ε_1 and ε_2 are coherently averaged over the Q_{32} distribution and incoherently averaged over fluctuations in the drive pulse energy. In our discussion of the calculations, we focus on ε_2 (at 589 nm) because most of our measurements were of this field rather than ε_1 (at 1141 nm). We confirmed the presence of an emission pulse at 1141 nm, but we did not perform time resolved measurements of the pulse profile. Simulation results, after using this additional feature, are shown in Figure 5.7b.

Both, the measurements and calculations, reveal a dramatic dependence of the stimulated emission yield (at 589 nm) on the drive pulse shape. They also predict a temporally delayed simulated emission The fact that the stimulated emission pulse is delayed with respect to the drive pulse indicates that it is not the result of a parametric process [78]. Furthermore, the duration of the pulse compared with the coherence time in the vapor allows us to identify the pulse as Super Florescence (SF) rather than Amplified Spontaneous Emission (ASE). The condition for SF rather than ASE is that $T_2 \gg \sqrt{(}\tau_r \tau_d)$, where T_2 is the coherence time, τ_r is the stimulated emission pulse duration, and τ_d is the delay of the simulated emission pulse relative to the drive pulse [79–81]. We calculate the coherence time to be $T_2 = 440$ps (from collision line broadening, [59]), thus fulfilling the condition above for SF rather than ASE. Finally, we identify the SF as Yoked Super Fluorescence (YSF) because the SF involves two emissions (ε_1 and ε_2) occurring at the same time rather than cascaded. Further evidence of YSF instead of cascade SF is that the later also emits a backwards SF beam [82]. We see no experimental evidence of backwards

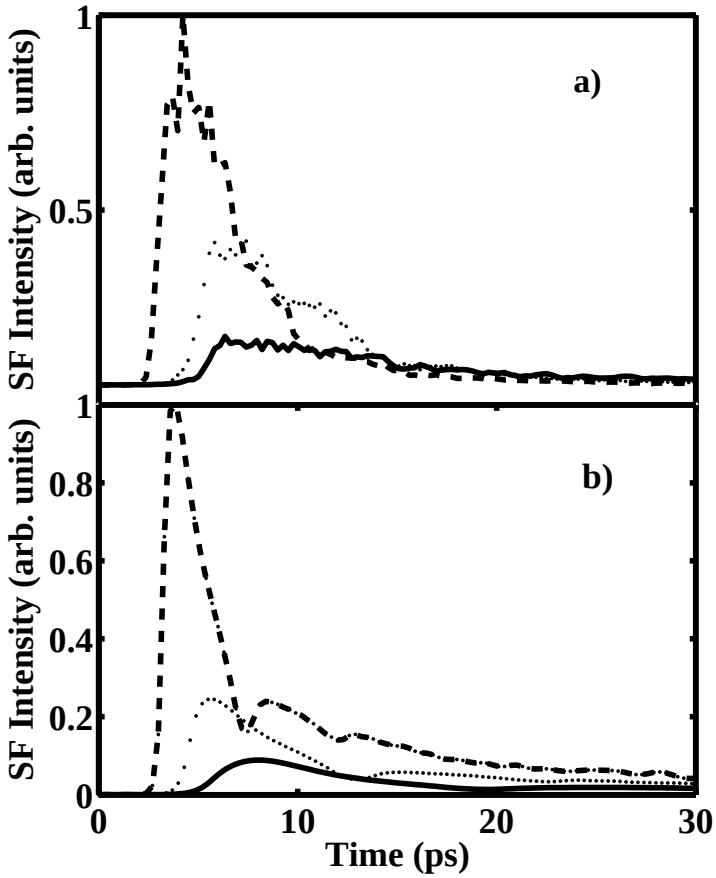

Figure 5.7: a) Experimental cross correlation measurement of the stimulated emission pulse profiles for atomic densities of $3.16 \times 10^{21} m^{-3}$ (dashed),$1.55 \times 10^{21} m^{-3}$ (dotted) and $9.56 \times 10^{20} m^{-3}$ (full) with a propagation length $Z =$ 10 cm. b) Calculated stimulated emission pulse profiles for the same densities as used in the measurements.

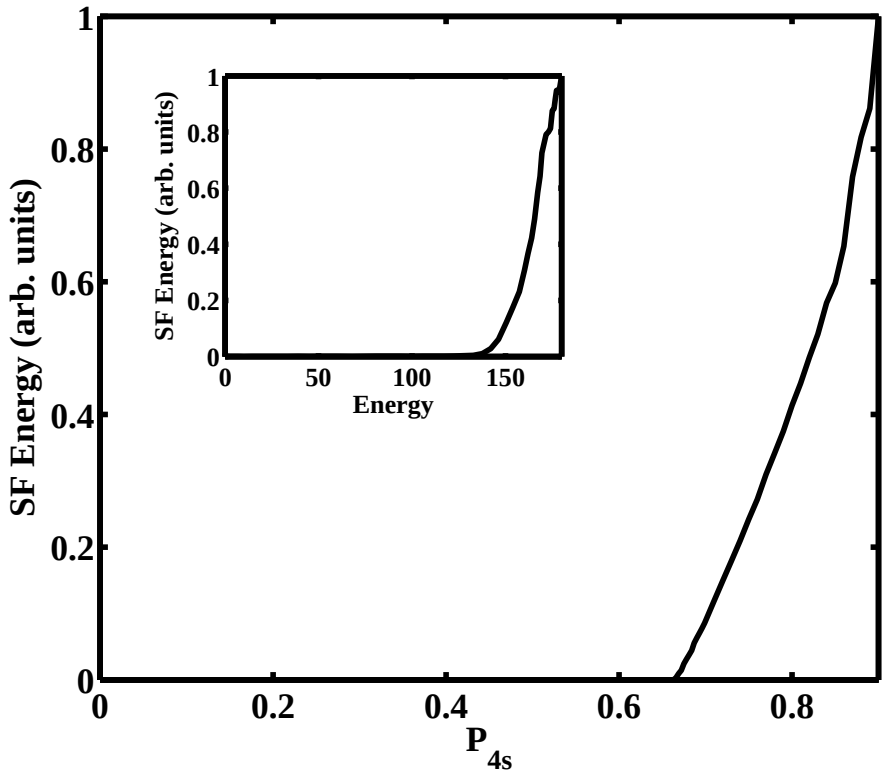

Figure 5.8: Stimulated emission yield vs 4s population (Q_{22}). Parameters used for the calculation are $N = 1.33 \times 10^{21} m^{-3}$, $z = 10$cm, $Q_{32}(z = 0, t = 5 \times \tau_L) = 10^{-}6$. Inset: Experimental stimulated emission yield (SF) vs drive pulse energy.

SF. The almost perfect coherence of the SF pulse is consistent with the basic picture of SF where the emission is a result of phase locking of the many atomic dipoles in the ensemble, acting together as one macroscopic dipole. with a width and delay which depends on density.

Our calculations of the stimulated emission buildup indicate that the optimal pulse shape found in experiments using our GA is more effective than an unshaped pulse in inverting the 3s-4s transition. Also, both our measurements and calculations indicate the stimulated emission is a delayed and nearly perfectly coherent pulse. Therefore, we examine the stimulated emission yield as a function of the population transfer accomplished by the drive pulse. In Figure 5.8, we show the dependence of the stimulated emission yield as a function of 4s population following the drive pulse. We observe a very sharp

threshold at about 0.666. This graph should be compared to the experimentally measured stimulated emission yield as a function of drive pulse energy, as shown in the inset. Clearly the stimulated emission yield is *very* sensitive to the 4s population near threshold. This explains the substantial gains in the stimulated emission yield with pulse shaping, since an unshaped drive pulse transfers much less than 50% of the ground state population to the 4s state, but a shaped pulse can transfer close to 100% [33]. The control over the stimulated emission yield therefore reflects control over single atom dynamics during the drive pulse followed by a collective atomic response *if the control pulse can generate a critical population inversion*. The coherence between the 3s and 4s states during the drive pulse is critical for control, and underscores the fact that the control in this experiment is coherent. Once the control pulse is able to achieve a critical inversion density, the atoms act collectively, and super-fluoresce.

In conclusion, we have uncovered the physical mechanism underlying control over stimulated emission in an ensemble of sodium atoms exposed to shaped strong field laser pulses. The stimulated emission can be understood in terms of super fluorescence, which results from an almost impulsive inversion of the atoms and phaselocking of their dipoles. The inversion is achieved by shaping of the strong field drive pulses, compensating for the effects of the dynamic Stark shift. The dramatic gains in the SF yield with pulse shaping reflect the sensitivity of the collective atomic dynamics to the impulsive inversion achieved with a shaped ultrafast laser pulse. This work illustrates that one must be careful in interpreting stimulated gains based on a single atom/molecule response in control experiments. It also suggests that modest coherent control yields for single quantum systems can lead to dramatic effects whenever an ensemble of such systems can act collectively following control on an ultrafast timescale. We are currently investigating the detailed correlated behavior of the two emitted SF pulses, and how they can be used to drive correlated absorption.

Chapter 6

Control in a three level system

In Chapter 4 we discussed the underlying physics for TPA in the presence of strong fields. The discussion was limited to two levels. In this chapter we discuss control of a three level system: The $3s$, $4s$, and $7p$ levels in atomic Na. Since the $4s \rightarrow 7p$ has a wavelength of 781.2nm, the same 35fs laser can target the TPA $3s \rightarrow 4s$ and the $4s \rightarrow 7p$. Level schemes like this one are called $2+1$ [17], since there is a two photon transition followed by a one photon transition to the final state. As expected, the case of three levels, will build on the two-level one.

6.1 Transition from weak to strong fields in a three level system

For the study of the transition from weak to strong fields in a three level system, we follow the same procedure used in Section 3.5. We used our GA to optimize the excitation to the $7p$ state at different laser pulse energies. Figure 6.1 shows the ratio $\mathrm{P}_{optimal}/\mathrm{P}_{unshaped}$ for the 7p population transfer as a function of pulse energy. $\mathrm{P}_{optimal}$ is the population transfer obtained with a feedback shaped pulse and $\mathrm{P}_{unshaped}$ is the population transfer obtained with an unshaped pulse. As in the two level case, there is a smooth transition from the weak to strong field regime illustrated by the improvement in a shaped pulse relative to an unshaped one. Note that in the weak field limit, the ratio goes to $\sim$3. This highlights the fact that pulse shaping is required for optimizing population transfer even for weak fields if there is an intermediate resonance. The intensity I_0 corresponds the peak intensity required for a π pulse (50fs FWHM) on the 3s-4s transition when compensating for the DSS. The error bars indicate the variation in population transfer for several optimizations at the same pulse energy. A similar result was found for TPA with an intermediate resonant

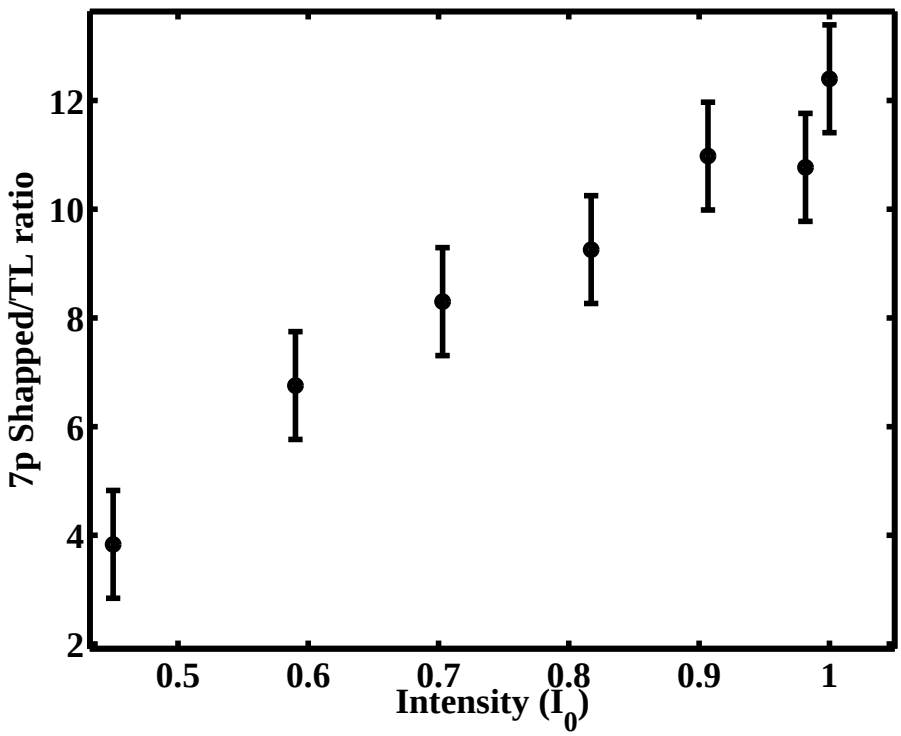

Figure 6.1: Ratio of 7p population for a GA maximized pulse to an unshaped one vs intensity. I_0 is the peak intensity required for a π pulse (50fs FWHM) on the 3s-4s transition. Center wavelength is $\lambda_0 = 780nm$.

level [16].

As in the case of two levels TPA, we also study the co-dependence on pulse shape and intensity for a π phase jump in the spectral phase. For the case of the three level system, a π phase jump around the intermediate resonance yields an intuitive enhancement over an unshaped pulse in the weak field limit [17]. As there is a π phase shift of the response around resonance for a driven oscillator, one can improve the constructive interference of the near resonance contributions to the three photon $7p$ excitation by placing a π phase jump in the spectrum around the frequency resonant with the $4s-7p$ transition. These measurements can be compared directly with [17], for the weak field limit.

Figure 6.2a) shows the measurements of the 7p population transfer as a function of pulse energy and π phase jump position. Panel b) shows simulation results for the dependence on π phase jump position for three different intensities. Again, there is a clear transition from weak to strong fields. A

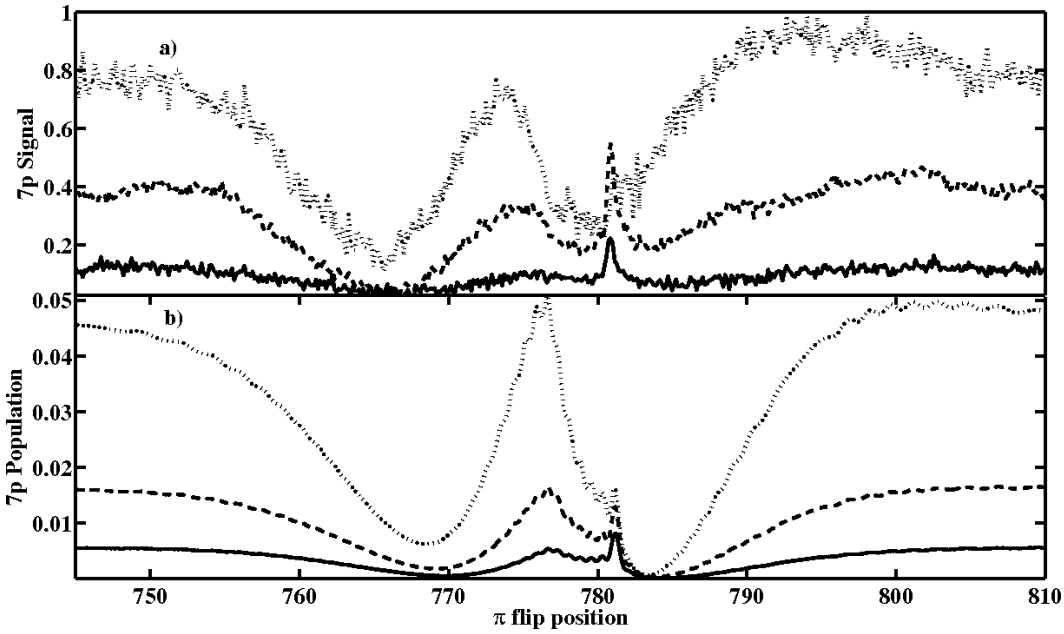

Figure 6.2: a) Measurement of the 7p population for three different energies as function of the π flip position. b) Simulation of the 7p population for equivalent peak intensities as function of the π flip position. The enhancement obtained for weak fields at $\lambda_0 = 781.2$nm washes out for high fields. In all graphs, solid line is for low intensities ($I \approx 0.1 I_0$), the dashed line is for intermediate energies ($I \approx 0.4 I_0$), and the dotted line is for ($I \approx I_0$). I_0 is the peak intensity required for a π pulse (50fs FWHM) on the 3s-4s transition.

new feature in the measurement which highlights the difference between strong and weak fields is the narrow peak at 781.2nm. This corresponds to the field free resonant wavelength for the 4s to the 7p transition [17]. For the lowest intensities, the enhancement with a π flip at this frequency is about a factor of three over an unshaped pulse (Fig. 6.2b)) consistent with the ratio of 3 seen for weak fields in figure 6.1. However, as the intensity increases, this enhancement essentially disappears as shown in the dashed line in Figure 6.2b). The enhancement vanishes for high field intensities because of the DSS of the $4s$ and $7p$ states. The resonance condition is not at 781.2 nm at all times during an intense pulse and averaging over different detunings results in cancellation of this resonant enhancement. We argue that this is a generic feature of strong field excitation and control in the strong field must take this into account in order to be effective.

The other features in the $7p$ data follow the $4s$ data, illustrating that

the same pulse features which maximize the 4s population are efficient at populating the 7p as well. We are currently investigating to what extent it is possible to maximize the 7p population while minimizing the population of the 4s. There are several indications that this is possible and that it is even possible to transfer more population to the 7p state than to the 4s using strong fields.

6.2 Control results of three levels in atomic Sodium

In Figure 6.1 we saw that feedback control yields improvements over a TL pulse of roughly 10. This is closely related to the well known fact that in the case of intermediate resonances, an unshaped pulse is not optimal [16]. Yet, we would like to get more insight into the mechanism for maximizing the population transfer in a three level system, when one transition involves a multiphoton process. Unfortunately, this case is not as simple as the two level single photon problem, where a simple condition of detuning and pulse area is sufficient. This project is still under development and will be part of a future Ph.D. thesis. Here we present a summary of the present results.

The detection scheme used was discussed in Section 2.4. All the results presented in this section were obtained by measuring the $5d \rightarrow 3p$ transition at 500nm.One thing that we realized early on the experiments trying to maximize the $7p$ population is that the energy that goes through the pinhole is too small to invert the total population. Just recently we acquired a diamond pinhole (Lenox Laser part No HP-3/8-DISC-DIM-100) that allowed us spatially filtered energies of $\sim 25\mu$J. With these energies we are able to go well into the non-perturbative regime of the 2+1 transition. This is clearly seen in an energy scan of the $5d \rightarrow 3p$ fluorescence (500nm). The result is shown in Figure 6.3.

We have already shown the results from the feedback on the fluorescence that measures the $7p$ population. There we saw that at high energies, the GA yield improvements of a factor of 10. At higher energies we see that this ratio remains almost constant, the reason being that as the energy increases the yield of a TL pulse also improves. Following the same scheme as for the two level case, we can now used the experimentally retrieved pulses and use them to integrate Schrödinger equation with Hamiltonian Eq. 3.45.

The results of such simulation are shown in Figure 6.4. For this calculation we used GA runs at 25μJ for which we estimate a peak intensity of roughly $I_0 \approx 3.5 \times 10^{15} W/m^2$. As we can see from the figure, the pulse found by the GA is not a simple one. This is not an isolated case, but rather standard and

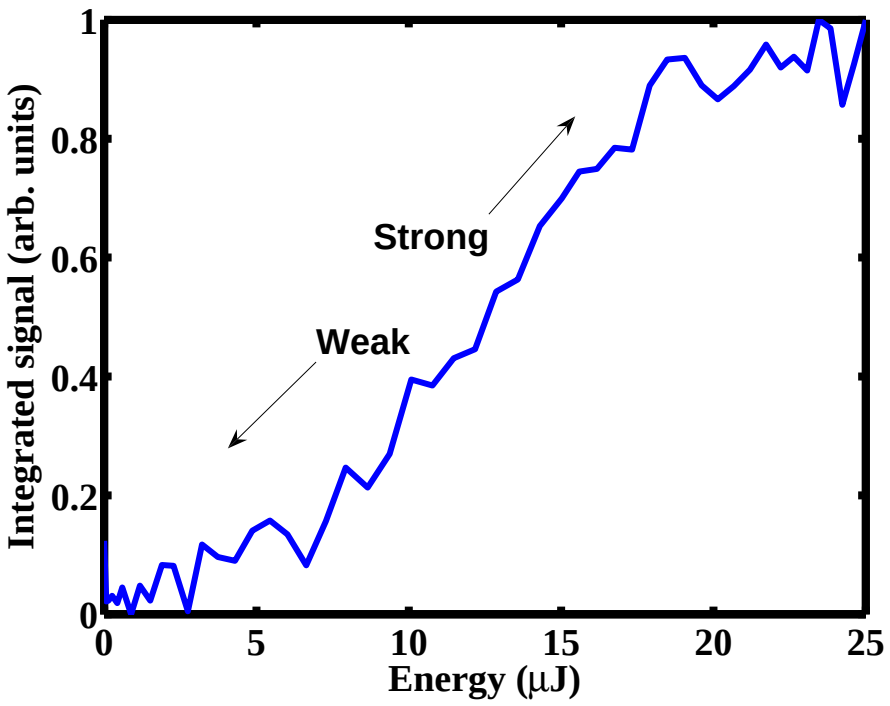

Figure 6.3: Energy scan of the $5d \rightarrow 3p$ transition for an unshaped pulse.

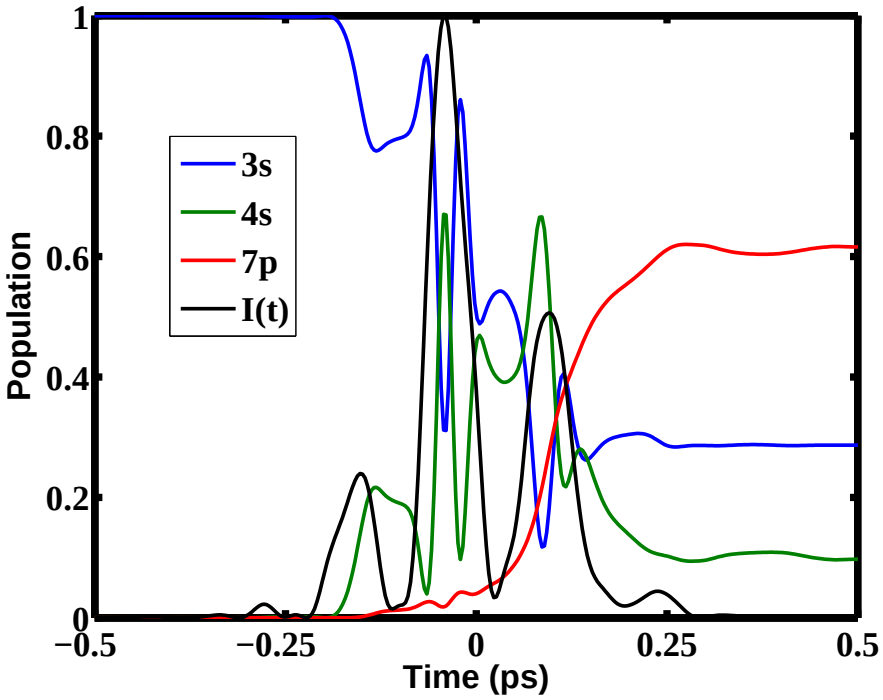

Figure 6.4: Population as function of time for levels $3s$, $4s$, and $7p$. The intensity profile is shown in black.

is a major obstacle we have found in this study since the FROG algorithm has strong limitations when the shape of the electric field is this complicated. Is for this reason that we have also used another approach, where instead of using the FROG pulses, we calibrate the pulse shaper and calculate the output field by means of a simple Fourier transform.To have an idea how critical this is, in Figure 6.5 we show the reconstructed fields with this method. The time dependent field (panel b) should be compared with the intensity profile in Figure 6.4.

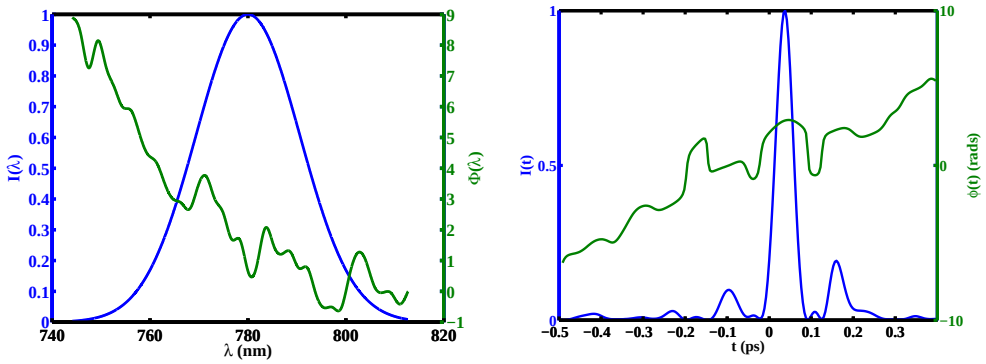

(a) Intensity and phase in wavelength.

(b) Intensity and phase in time

Figure 6.5: Pulse reconstruction from a GA optimized pulse. The reconstruction is through a pulse shaper frequency calibration and a Fourier transform.

The fact that fields reconstructed by both methods are so different indicate that extra care needs to be taken when trying to use experimentally obtained fields, since they are extremely complicated. We will come back to the control of the $7p$ briefly in the next chapter. But again, this will be the main topic of another project in our group.

Chapter 7

Extensions and future work

In this chapter we will discuss some topics that are still open to some discussion and probably will be part of future projects in our group.

7.1 Local control theory for two and three level systems

This section will treat theory and simulation results for another kind of control scheme. While the learning algorithms, such as the GA, can be considered as extreme points (maximum or minimum) global searching algorithms, there are other approaches. One such approach is the so called *Local Control* and it was developed in a series of papers by Ronnie Koslov an David Tanor [35–37] and recently generalized in [38]. The basic idea behind this scheme is to integrate the Schrödinger equations in time asking at each point in time that a certain condition (or conditions) be satisfied. This is similar to finding an extreme in a function with restrictions using Lagrange multipliers.

7.1.1 Two level systems

In order to illustrate the procedure we will first study the two level system in the presence of DSSs. The starting point is again the time dependent Schrödinger Eqs. 3.28,

$$\begin{aligned} \dot{a}_g(t) &= -i\omega_g^{(s)}(t)a_g(t) - i\chi^*(t)e^{-\imath\Delta t}a_e(t), \\ \dot{a}_e(t) &= -i\omega_e^{(s)}(t)a_e(t) - i\chi(t)e^{\imath\Delta t}a_g(t). \end{aligned} \tag{7.1}$$

The optimum pulse shape for controlling the excited state is an electric field that at any given time takes electrons from the ground to the excited

state. Formally, this is equivalent to,

$$\frac{d|a_e(t)|^2}{dt} \geq 0. \tag{7.2}$$

Since the amplitudes are complex numbers, the derivative of its absolute value can be written as,

$$\frac{d|c_i(t)|^2}{dt} = 2Re\{c_i^*(t)\dot{c}_i(t)\}. \tag{7.3}$$

Using this, the population rate of change can be written as,

$$\frac{d|c_g(t)|^2}{dt} = 2\chi(t)Im\{e^{\imath\alpha(t)}c_g^*(t)c_e(t)\}, \tag{7.4}$$

$$\frac{d|c_e(t)|^2}{dt} = 2\chi(t)Im\{e^{-\imath\alpha(t)}c_e^*(t)c_g(t)\}, \tag{7.5}$$

which combined with Eq. 7.7, gives the necessary condition for the population transfer to the excited state $4s$ be maximum and *monotonic*,

$$\chi(t)Im\{e^{-\imath\alpha(t)}c_e^*(t)c_g(t)\} \geq 0. \tag{7.6}$$

We should notice that the above condition needs to be satisfied by the intensity temporal profile $\chi(t)$ and the atom-laser phase parameter $\alpha(t)$. The amplitudes will follow this two parameters according to Eq. 3.28. Just as in the case of learning algorithms, local control won't give all the necessary information to understand the underlying physical process in a given phenomena, but at least can give solutions that "solve" the problem at hand.

For our simulations, we used a more "relaxed" condition than Eq. 7.2. We choose $\chi(t)$ and $\alpha(t)$ such that they satisfy,

$$\left.\frac{d|a_e(t)|^2}{dt}\right|_{\chi(t),\alpha(t)} = \max\left(\frac{d|a_e(t)|^2}{dt}\right). \tag{7.7}$$

Figure 7.1 shows the results of integrating Eqs. 7.1 using the local condition in Eq. 7.7. The simulations were carried out at three different wavelengths and changing only the intensity (panels a) to c)) in time to maximize the time gradient of the $4s$ population. In panel d), we show the same simulation as in panel for $\lambda_0 = 780$nm, but now changing the phase as well to fulfill Eq. 7.7. From the simulations we found that the local control approach can invert the population to the $4s$ level. However, if a center wavelength different than $\lambda_0 = 771nm$ is used, not only the temporal intensity profile is important, but the phase needs to be controlled as well for the inversion to happen. This

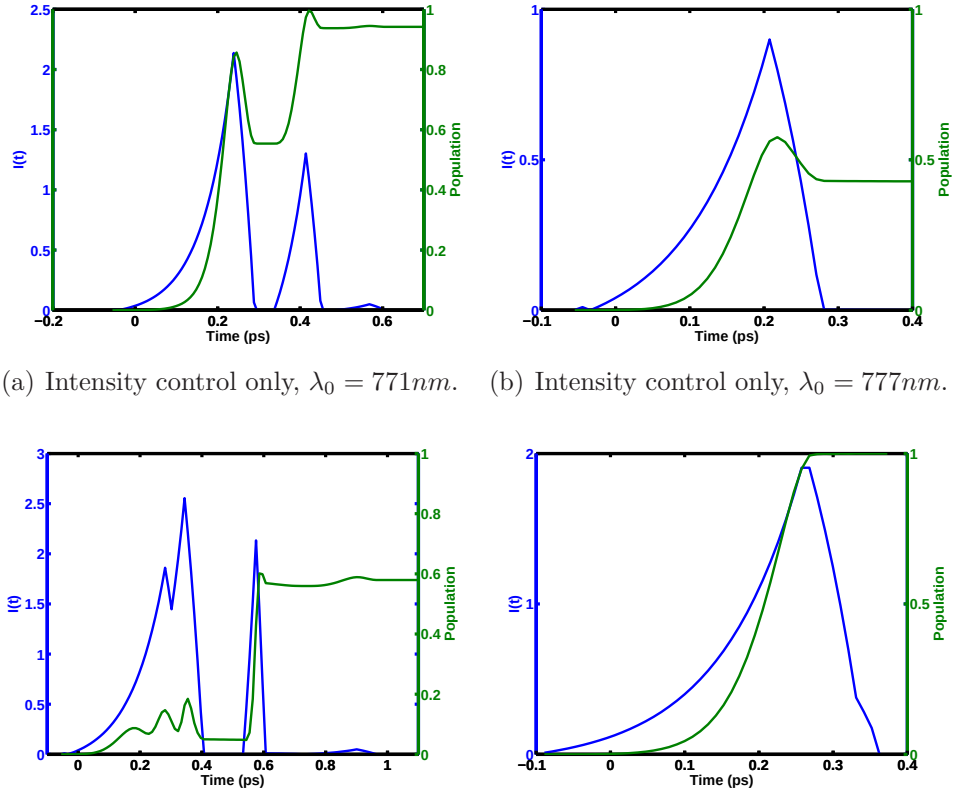

(a) Intensity control only, $\lambda_0 = 771nm$. (b) Intensity control only, $\lambda_0 = 777nm$.

(c) Intensity control only, $\lambda_0 = 780nm$. (d) Intensity and phase control, $\lambda_0 = 780nm$.

Figure 7.1: Fields and populations in time after the integration of Eqs. 7.1 using the local control algorithm with condition in Eq. 7.7. The calculation is done for different center wavelengths of the pulsed field, controlling only the intensity profile $I(t)$ (panels a) to c) or both the phase $\varphi(t)$ (not shown) and $I(t)$ (panel d)). Intensity is in units of $I_0 = 2.88 \times 10^{15} W/m^2$, which is the intensity required for a 50 fs π pulse on the $3s \rightarrow 4s$ transition.

contrasts with the results shown in Chapter 4, in particular, those shown in Figure 4.5, where two gaussian pulses separated at some delay can yield a full inversion of the population at different wavelengths. This demonstrates one strong shortcoming of this approach, *it is a local search algorithm*, in contrast with the GA which is a global one. It should also be noticed that the condition in Eq. 7.2 is more strict than just population inversion since it also demands that the population never decrease in time, whereas a learning algorithm only cares about the limit $|a_e(t \to \infty)|^2 = 1$ without requiring a monotonic increase.

7.1.2 Three level systems

For the three level case, the starting point is again the three level Hamiltonian in Eq. 3.45. However, for simplicity, we will consider that the DSS of the $7p$ is negligible. This is supported by simulations done with and without the inclusion of the Stark shift for this level that give almost the same results. Under this approximation the three level Hamiltonian becomes,

$$\hat{\mathbf{H}}_{\mathbf{3}}(t) = \begin{pmatrix} \omega_g^{(s)}(t) & \chi^*(t)e^{i(\Delta t-\varphi(t))} & 0 \\ \chi(t)e^{-i(\Delta t-\varphi(t))} & \omega_e^{(s)}(t) & \chi_{er}^*(t)e^{-i[\varphi(t)/2-\Delta_{er}t]} \\ 0 & \chi_{er}(t)e^{i[\varphi(t)/2-\Delta_{er}t]} & 0 \end{pmatrix}. \tag{7.8}$$

After doing the same two rotations in Eqs. 3.31 and Eqs. 3.35, the three level Hamiltonian above transforms to,

$$\hat{\mathbf{H}}_{\mathbf{3}}''(t) = \begin{pmatrix} 0 & \chi(t)e^{\imath\alpha(t)} & 0 \\ \chi(t)e^{-\imath\alpha(t)} & 0 & \chi_{re}(t)e^{\imath\alpha_3(t)} \\ 0 & \chi_{re}(t)^*e^{-\imath\alpha_3(t)} & 0 \end{pmatrix}. \tag{7.9}$$

with,

$$\chi_{re} = -\frac{\mu_{er}}{2\hbar}\varepsilon_0\sqrt{g(t)}, \tag{7.10}$$

and

$$\alpha_3(t) = -\varphi(t)/2 + \Delta_{re}t + \int_{-\infty}^{t} \omega_e^{(s)}(t')dt'. \tag{7.11}$$

The Schrödinger equation for the amplitudes c_i is now,

$$\begin{aligned} \dot{c}_g(t) &= -i\chi(t)e^{\imath\alpha(t)}c_e(t), \\ \dot{c}_e(t) &= -i\chi^*(t)e^{-\imath\alpha(t)}c_g(t) - i\chi_{re}(t)e^{\imath\alpha_3(t)}c_r(t), \\ \dot{c}_r(t) &= -i\chi_{re}(t)^*e^{-\imath\alpha_3(t)}c_e(t). \end{aligned} \tag{7.12}$$

Using again Eq. 7.3, the rate of change of the population in states g, e, and r is,

$$\begin{aligned}
\frac{d|c_g(t)|^2}{dt} &= 2\chi(t)Im\{e^{\imath\alpha(t)}c_g^*(t)c_e(t)\}, \\
\frac{d|c_e(t)|^2}{dt} &= 2\left[\chi(t)Im\{e^{-\imath\alpha(t)}c_e^*(t)c_g(t)\} + \chi_{re}Im\{e^{\imath\alpha_3(t)}c_e^*(t)c_r(t)\}\right], \\
\frac{d|c_r(t)|^2}{dt} &= 2\chi_{re}Im\{e^{-\imath\alpha_3(t)}c_r^*(t)c_e(t)\}. \qquad (7.13)
\end{aligned}$$

Excitation to the third resonant level r is given by the condition,

$$\left.\frac{d|c_r(t)|^2}{dt}\right|_{\chi(t),\alpha(t)} = \max\left(\frac{d|c_e(t)|^2}{dt}\right). \qquad (7.14)$$

The result of integrating Eqs. 7.12 using the local condition Eq. 7.14 is shown in Figures 7.2a) to f). The calculations were done for different center wavelengths, λ_0. Panels a), c), and e) show the the intensity (blue)and phase (green) in time that maximize the $7p$ population. In panels b), d), and f) we show the time evolution of the population for the three levels, $3s$ (blue), $4s$ (green), and $7p$ (red) for their respective fields. From top to bottom, the used center wavelengths were $\lambda_0 = 775$nm (panels a) and b)), $\lambda_0 = 777$nm (panels c) and d)), and $\lambda_0 = 781$nm (panels e) and f)). It is remarkable how successful the integration algorithm is, as it finds solutions that are able to invert the population to the third state for all wavelengths. It is also noticeable that the population in the $7p$ increases monotonically in perfect agreement with Eq 7.14. The reason why the intensity profiles in Figures 7.2a), c), and f) is that the the search algorithm is purely linear, more sophisticated time steps can give smoother variations (see for example [36]). It is also interesting the fact that for all frequencies there is a chirp that follows the intensity profile. This clearly means that the instantaneous frequency will change to compensate, not only for the DSS between the $3s$, $4s$, and $7p$, but also, some shaping is needed to take population to the $7p$ *without* taking population from the $4s$ down to the ground state. The sequence in which this happens, can be seen by looking in detail to the figures. The population goes first from the $3s$ to the $4s$, and then to the $7p$. This is in close resemblance to the analysis we did in the previous chapter, where the excitation to the $7p$ is clearly divided in a two step process.

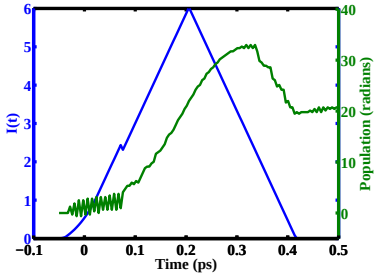

(a) Optimum intensity and phase, $\lambda_0 = 775nm$.

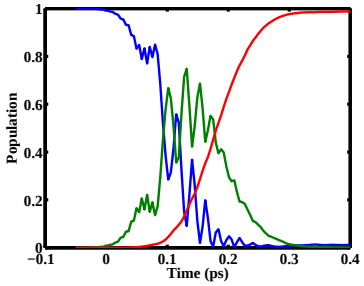

(b) Population of the three levels $3s$, $4s$, and $7p$ for $\lambda_0 = 775nm$.

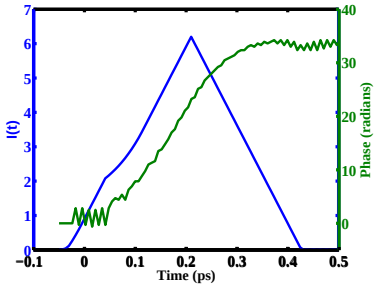

(c) Optimum intensity and phase, $\lambda_0 = 777nm$.

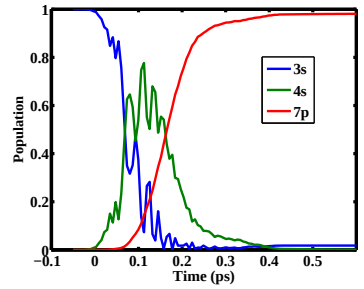

(d) Population of the three levels $3s$, $4s$, and $7p$ for $\lambda_0 = 777nm$.

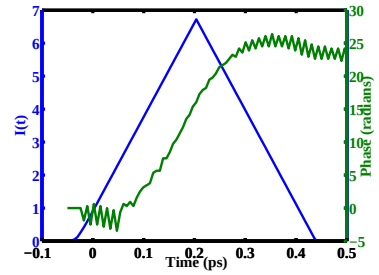

(e) Optimum intensity and phase, $\lambda_0 = 781nm$.

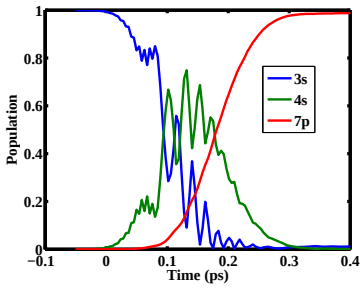

(f) Population of the three levels $3s$, $4s$, and $7p$ for $\lambda_0 = 781nm$.

Figure 7.2: Fields and populations in time after the integration of Eqs. 7.12 using the local control algorithm with condition in Eq. 7.14. The calculation is performed for different center wavelengths. Intensity is in units of $I_0 = 2.88 \times 10^{15} W/m^2$, which is the intensity required for a 50 fs π pulse on the $3s \rightarrow 4s$ transition.

7.2 Pulse shape spectroscopy of molecules

In this section we will extend the knowledge gained in the atomic case. Coherent control of molecular excitations is a vast topic in the AMO community [49, 50, 64, 65, 83]. Molecules, just as atoms, can exhibit multiphoton transitions. For several molecules, the first electronic excited state is a few eV away from the ground state. At $\lambda_0 \approx 800$nm (the most common wavelength for femtosecond lasers), the only possible way of exciting the molecule is through a multiphoton transition.

We use the same approach as in Chapter 4 to study the transition from weak to strong fields. More specifically, in this section we study dissociative ionization as a functions of spectral π phase flip position (see Section 3.5). To further motivate this section, in Figure 7.3 we show the experimental result of the above mentioned phase manipulation for atomic Na and the CCl_4 molecule.

From the figure we can see that the CCl_3^+ ion yield shows a similar behaviour to that of the $4s$ population in atomic Na. The main difference is the fact that the enhancement near the middle of the spectrum moves in a different direction with increasing energy. They also differ in that the dark pulses are not so dark for CCl_3^+. We also measured other fragments and they show similar behaviours. This is an important observation since it suggests that there is an intermediate state through which almost all excitations, after interacting with our laser field, have to go through.

In Figure 7.2 we show the absorption spectrum of the CCl_4 molecule. The red dashed line indicates where the absorption of four photons occurs in the spectrum for a field with wavelength of $\lambda_0 = 800nm$. This is the first excited state of CCl_4. From this, we assume that ionization and creation of the child ions CCl_3^+ and CCl_2^+ has an intermediate state at four photons from the ground state. From the intermediate state the molecule gets ionized, CCl_4^+ is unstable and decays to CCl_3^+. The described excitation path is depicted in panel b) of the same figure. This excitation scheme resembles the well known Resonance Enhanced Multiphoton Ionization (REMPI) [85].

To better understand the physical process behind these experimental results, we developed a simple model to describe the interaction of strong fields with this molecule. The four photon transition between the ground and the first excited state of CCl_4 can be treated in the same way as the TPA in atomic Na but for a higher order process. Since we are dealing with strong fields, the phase-matching model described earlier seems very appropriate. Theoretically, we follow closely the density matrix formalism developed earlier in Section 3.10. Here we start with the rotated two level Hamiltonian in Eq.

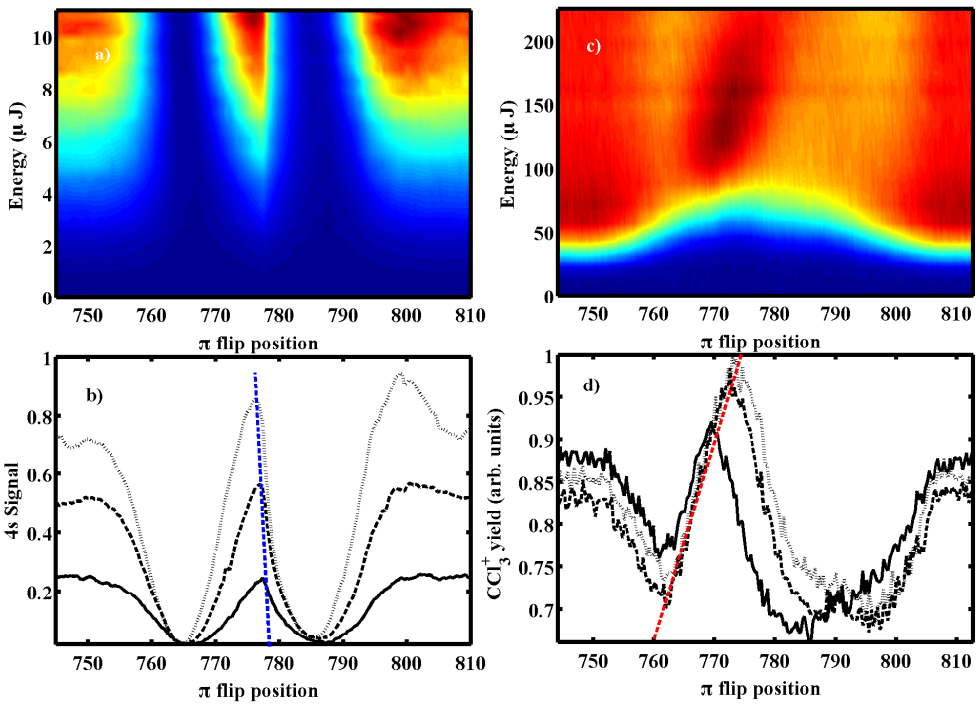

Figure 7.3: a) Experimental measurement of the Na 4s population as function of pulse energy (equivalent to peak intensity) and π flip position. b) Line outs of a) for three different pulse energies. c) Same as a) for the CCl_3^+ yield after ionization of CCl_4. d) Lineouts of c) at three different energies.

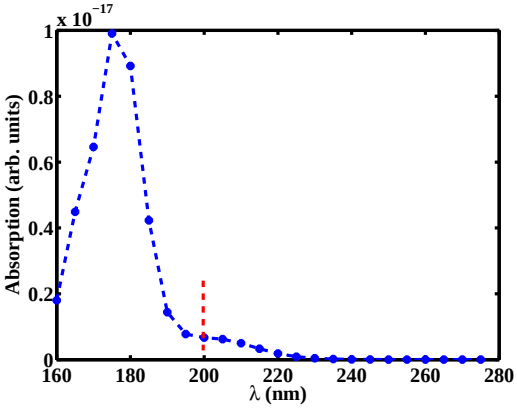

(a) Absorption spectrum for CCl_4 [84].

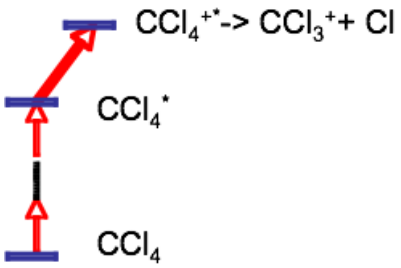

(b) Excitation path for $CCl_4 + \gamma \rightarrow CCl_3^+ + Cl + e^-$.

Figure 7.4: Excitation path and absorption spectrum for CCl_4. The red dashed line in the spectrum indicates where the 4 photon absorption is for a field of center wavelength $\lambda_0 = 800nm$.

3.36, but for a four photon process,

$$\hat{\mathbf{H}}'' = \begin{pmatrix} 0 & \chi_4(t)e^{i\alpha_4(t)} \\ \chi_4(t)e^{-i\alpha_4(t)} & 0 \end{pmatrix}, \tag{7.15}$$

with,

$$\alpha_4(t) = -\left[\int_{-\infty}^{t} \delta_\omega^{(s)}(t')dt' - \Delta_4 t + 2 * \varphi(t)\right], \tag{7.16}$$

where $\delta_\omega^{(s)}(t)$ is the DSS exactly as before, which means it scales with the intensity, *not* with the intensity squared. $\chi_4(t) = \chi_4^0 \varepsilon(t)^4$ is the time dependent four-photon coupling between the ground and the first excited state and $\Delta_4 = 4\omega_0 - \omega_{eg}$ is the four photon detuning. It should also be noted that $\alpha_4(t)$ has now a term $2 \times \varphi(t)$ since the four photon process scales with the field to the fourth power.

For atoms, the excited electron can undergo several Rabi oscillations from the ground to the excited state. In molecules, there is a high density of states, in particular for states beyond the highest occupied molecular orbital (HOMO). This means that as the field increases, the molecule, instead of going into the stimulated emission regime, will undergo further excitation. To simulate this process, we propose the inclusion of a term into the density matrix equations, similar to that used to describe spontaneous decay in atoms. With

this in mind and using the above Hamiltonian we arrive to the equations of motion for the slowly varying density matrix,

$$\frac{\partial}{\partial t}Q_{11} = 2\chi_4(t)\,\mathrm{Im}\{e^{i\alpha_4(t)}Q_{21}\} \tag{7.17}$$

$$\frac{\partial}{\partial t}Q_{22} = -2\chi_4(t)\,\mathrm{Im}\{e^{i\alpha_4(t)}Q_{21}\} - A_L|\varepsilon(t)|^{N_L}Q_{22} \tag{7.18}$$

$$\frac{\partial}{\partial t}Q_{21} = -i\chi_4(t)e^{-i\alpha_4(t)}(Q_{11}-Q_{22}), \tag{7.19}$$

where the second term in right hand side of Q_{22} is the above mentioned, decoherence-like term since it's real and $\propto Q_{22}$ [59]. Notice however that it also contains a field dependence $A_L|\varepsilon(t)|^{N_L}$. This is included since the further excitation from this intermediate level is proportional to some power of the field (depending on the order of the transition).

In the case of molecular dissociative ionization, the excited state $*$ (see Figure 7.2) serves as a resonant intermediate state en route to the electronic continuum. Therefore, we extend our two level model to a three level system. Since the molecular states couples strongly to many different states in addition to the intermediate resonant one, we model the coupling between the intermediate and final states as an incoherent interaction that depends on the field strength and the intermediate state population. Assuming that the ionic state we measure in the lab is some electronic state with electron population probability Q_{33}, the time evolution equations for the relevant electronic states are,

$$\frac{\partial}{\partial t}Q_{11} = 2\chi_4(t)\,\mathrm{Im}\{e^{i\alpha_4(t)}Q_{21}\} \tag{7.20}$$

$$\frac{\partial}{\partial t}Q_{22} = -2\chi_4(t)\,\mathrm{Im}\{e^{i\alpha_4(t)}Q_{21}\} - A_L|\varepsilon(t)|^{N_L}Q_{22} \tag{7.21}$$

$$\frac{\partial}{\partial t}Q_{21} = -i\chi_4(t)e^{-i\alpha_4(t)}(Q_{11}-Q_{22}) \tag{7.22}$$

$$\frac{\partial}{\partial t}Q_{33} = A_I|\varepsilon(t)|^{N_I}Q_{22}. \tag{7.23}$$

Here, $A_I|\varepsilon(t)|^{N_I}$ controls the rate of ionization to the state 3, which can, in general be different than the transition $1 \rightarrow 2$. $\alpha_4(t)$ is the atom-field (molecule-field in this case) phase parameter defined above. As mentioned before, A_L and N_L control the rate of de-excitation from the first excited state. On the other hand, A_I and N_I control the rate of excitation to the final dissociative state, which in turn, leads to the ionic fragment. In the general case, these parameters can be different, but for the simulations presented here we chose

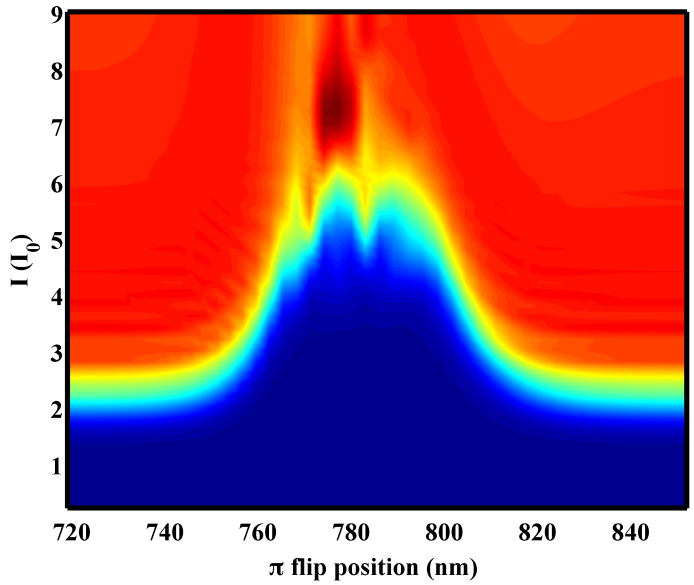

Figure 7.5: Theoretical simulation results after integrating Eqs. 7.20. $\lambda_0 =$ 780nm, peak $\delta_\omega^{(s)}(t) = 50$THz, $\Delta_4 = 120THz$. Intensity is in units of a four photon 50 fs π pulse.

$A_L = A_I$ and $N_L = N_I$.

Modeling molecular processes with actual molecules is a daunting task since quite often we need to infer most of their properties. This can be done either by *ab* Initio quantum calculations of the molecule or by a fit of the model to an experimental measurement (see for example [64, 65] for the former and [67, 67] for the latter). In our case we are going to explore the different parameters as a fit to our experimental measurement. The most relevant relation is between the DSS $\delta_\omega^{(s)}(t)$ and the four photon coupling $\chi_4(t)$. The latter is chosen as the two photon coupling per unit of intensity for Na squared, χ_0^2. With this parameter fixed, we then choose $\delta_\omega^{(s)}(t)$ so that $\max(\delta_\omega^{(s)}(t)) \sim \max(\chi_4(t))$. In Figure 7.5 we show the result of integrating Eqs. 7.20 using a peak DSS of 50THz and detuning $\Delta_4 = 120THz$. The positive sign of the DSS means that the relevant levels will move closer together as the fields gets stronger in time. The sign of the detuning is also fixed by the experimental data that shows that the enhancement of the ionization goes from blue to red frequencies. The figure shows that we are able to capture most of the features shown in the experimental measurements. To make this agreement clearer, in Figure 7.6a) we show lineouts of the experimental data in presented in Figure 7.3, together

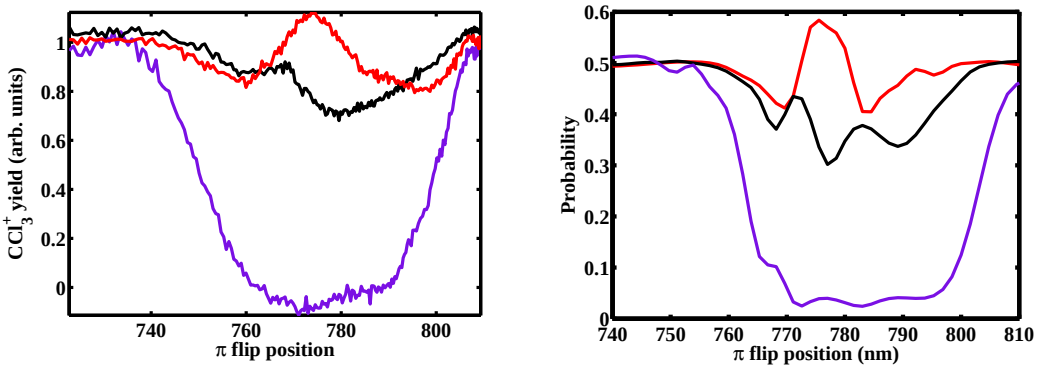

(a) Lineouts of the CCl_3^+ yield shown in Figure 7.3 at different energies.

(b) Lineouts of the simulation results shown in Figure 7.5 at different peak intensities.

Figure 7.6: Lineouts of the two dimensional data presented in Figures 7.3 (experiment) and 7.5 (simulations) at different energies and peak intensities respectively. In blue is shown the weak field limit and in red the strong field limit.

with (panel b) of the same figure) lineouts of the simulations shown in Figure 7.5.

One thing that stands out from Figure 7.6 is the fact that for low peak intensities, our theoretical model recovers the weak field behaviour shown in the experiment. As the field becomes stronger, the predicted structure from perturbation theory "washes" out, and a new pattern emerges. As expected, for strong fields, a transform limited pulse is no longer optimum and shaping is required to maximize the fragmentation yield. Other features recover by our three level theoretical model are, the saturation of the population in the ionic state, the tilt of the enhancement as the intensity grows, and the fact that there are no pure dark pulses. It is remarkable that we are able to reproduce the experimental data with such a simple model. This reinforces our initial qualitative picture that there is an intermediate state that dictates the excitation of the molecule and that the DSS takes the two levels closer instead of apart.

We need to mention that we tried several combinations of four photon coupling and DSS values, and only in a very limited set of values do we observe such an agreement with the experimental data. It is also important to mention that the trend shown in the case of the CCl_4 molecule is not universal. We performed the same experiments in other molecules and we obtained other results. In Figure 7.7 we show the fragment yield of some child fragments of

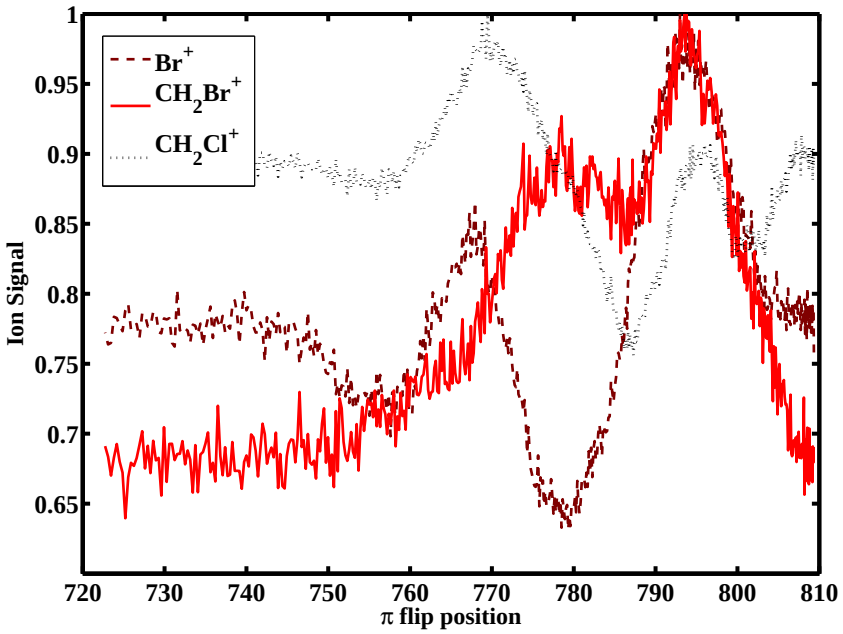

Figure 7.7: Yield of CH_2BrCl child fragments, Br^+, CH_3Br^+, and CH_2Cl^+ as function of a spectral π flip phase.

the molecule CH_2BrCl as function of π flip position in the spectrum of the pulse at high energies.

From the figure we note an almost total lack of correlation between the different fragments. This is in contrast with the case of the CCl_4 molecule where all child fragments showed an almost identical behaviour with the pulse shape and energy. Another feature of the data is that there is some degree of control between some of the fragments for a given position of the flip position. That is, for some pulse shapes (position of the π flip) there is a strong anticorrelation between different fragments. This might be explained by the presence of several intermediate states, each one leading to a particular dissociation channel. By changing the phase in the spectrum we target one of these states and therefore, control the fragment yield.

7.3 Future work

Stimulated Rapid Adiabatic Passage (STIRAP) is the long name given to the process that, by the use of two electric fields, is able to invert the population in a three level system without putting any (or almost any to be precise)

electrons in the intermediate state[37, 86, 87]. Furthermore, the population follows adiabatically the field directly from the ground state all the way to the final excited state. In Appendix A.3 we summarize the basics of the *standard* STIRAP. In atomic Na, we would like to achieve a STIRAP transition from the $3s$ to the $7p$, with the intermediate (non-populated) state being the $4s$ state. Whereas these processes have been studied for single photon transitions, the presence of a two photon transition in our case makes it quite different to what has been proposed before, although some groups have recently proposed similar studies. However, our system also differs in that we are proposing to use only one field and that both transitions, the $3s \rightarrow 4s$ TPA and the single photon from the $4s \rightarrow 7p$ one, are effectively targeted by the same field. STIRAP is usually achieved with two fields at different frequencies so that each one targets different transitions and their center frequencies are so far apart that each field only couples one pair of states. Processes very similar to STIRAP are the ones known as Optical Paralysis [36, 88]. The basic similarity is that some intermediate states are *paralyzed* in time, in the sense that they don't change its initial population as the optical field evolves in time. In the initial paper proposing the optical paralysis, the authors proposed the use of a single ultrafast field. In that sense, a better name for the proposed process here might be optical paralysis of multiphoton transitions. In any case, our goal is to invert the population from the $3s$ to the $7p$ while freezing the $4s$ at all times.

Our approach in this case is to make further use of the local control methodology discussed before for the three level systems. While we still need the condition in Eq. 7.14, we also need to add a new condition to trap the population in the $4s$. This condition can be expressed as,

$$\frac{d|c_e(t)|^2}{dt} = 0, \tag{7.24}$$

which clearly states that the population in the e ($4s$) state can not change at any time and in this particular case is set to be fixed at 0. From Eqs. 7.13 the above condition means that,

$$\chi(t) Im\{e^{-\imath\alpha(t)} c_e^*(t) c_g(t)\} = -\chi_{re} Im\{e^{\imath\alpha_3(t)} c_e^*(t) c_r(t)\}. \tag{7.25}$$

This closely follows the interpretation of the STIRAP by Malinovsky and Tannor [37] that the trapped state won't get populated as long as the contributions to it's population cancel out. In practice, the last equation gives us a constraint for how the phase and intensity need to be related to each other to achieve the trapped state. Simulations taking the new constraint into account

are underway. Another approach is to use two fields, each one with a small enough bandwidth that each won't interfere with the other transition. Since the transition from the $4s \rightarrow 7p$ occurs at $\lambda_{re} = 781.2$nm and the $3s \rightarrow 4s$ at $\lambda_{eg} = 777$nm we need fields with bandwidths of ~ 2nm.

Chapter 8

Conclusions

In this thesis we have shown that strong field multiphoton resonances can be controlled explicitly by phase tailoring an ultrafast laser pulse. This control can be used to compensate for the dynamic Stark shift in non-perturbative, two-photon absorption. From the theoretical point of view, a simple formalism illustrates the nature of the phase tailoring for an optimal pulse. More generally, higher-order transitions occur in the presence of these strong, intensity-dependent shifts, where the field-induced detunings are of the same order or larger than the effective coupling strengths. Unlike single-photon transitions, where the detuning is intensity-independent, or a lambda (Raman) system involving ground states, where Stark shifts may cancel each other out, the general coherent control problem involving multiphoton transitions typically must account for these types of strong field effects implicitly or explicitly. For systems where there are competing multiphoton resonances, phase compensation for dynamic Stark shifts combined with central frequency tuning and intensity may serve as effective control parameters in directing population to a selected target state.

We also found a general condition for inverting the population in a multiphoton transition. This condition is a time dependent quasi-phase matching picture. We shown how compensation of the DSS can be achieved experimentally by using a learning algorithm to discover strong field laser pulses that are more efficient than an unshaped pulse in driving two photon absorption. The solutions found by the GA can be understood in terms of an atom-field phase matching in the presence of a strong optical field. The results are promising for understanding closed-loop learning-control experiments in general.

In Chapter 5 we uncovered the physical mechanism underlying control over stimulated emission in an ensemble of sodium atoms exposed to shaped strong field laser pulses. The stimulated emission can be understood in terms of super fluorescence, which results from an almost impulsive inversion of the atoms

and phaselocking of their dipoles. The inversion is achieved by shaping of the strong field drive pulses, compensating for the effects of the dynamic Stark shift. We found the presence of a threshold in the population inversion of 0.66 for the system to lase. The dramatic gains in the SF yield with pulse shaping reflect the sensitivity of the collective atomic dynamics to the impulsive inversion achieved with a shaped ultrafast laser pulse. This work illustrates that one must be careful in interpreting stimulated gains based on a single atom/molecule response in control experiments. It also suggests that modest coherent control yields for single quantum systems can lead to dramatic effects whenever an ensemble of such systems can act collectively following control on an ultrafast timescale.

By using solutions found by our GA, we have studied the transition from weak to strong field excitation in two and three photon transitions using shaped ultrafast laser pulses. The distinction between the two regimes is made in terms of ground state depletion and dynamic Stark shifts. In weak fields, a frequency domain picture of the interaction is appropriate and captures the essential atom field dynamics. In strong fields, the resonance condition becomes dynamic, perturbative strategies for optimizing population transfer break down and a time domain picture yields insight into the strong field dynamics and pulse shape dependence. These results are also supported by the results obtained in the co-dependence with pulse shape and intensity in two and three photon transitions. For one, two or three pulses, the presence of high population transfer or dark pulses can be understood in terms of the quasi-phase matching picture mentioned above. Basically, as the field intensity increases, in order to obtain a high population inversion, the field needs to be tailored in such a way that the evolution of the atom-field phase parameter evolves by $N \times 2\pi$, with N an integer number that can be equal to 0. On the other hand, a dark pulse can be achieved if $\alpha(t)$ changes by π while the electric field is on. An important experimental finding is that, in order to understand strong field processes, a constant intensity profile in the interaction region is crucial.

Finally, we have shown that control in a three level systems is possible even in the presence of DSS. The fact that an unshaped pulse is very inadequate, even in the weak field limit, makes pulse shaping a must if control in this system is to be achieved. This topic looks very promising, and new studies are underway to explain how the control we achieve for a three level system, in the presence of multiphoton transitions, differs from well established schemes such as STIRAP. Local control theory has given us a great deal of insight in this case.

One very important result in this thesis work was presented in Section

7.2. Here we showed that the knowledge gained in the atomic case can be used in molecules. In particular, using simple pulse shapes that have a very intuitive and simple explanation on how they behave, in both the weak and strong limit is an attractive idea. A pulse with a π phase flip that changes position in the spectrum is an example. This pulse shape has a very well known behaviour that can be traced to weak fields. In the strong field limit, this pulse parametrization can be used to map the presence of the DSS. Whereas a simple three level model can not totally match the experimental data to a 100%, it is able to reproduce of the key features of the experimental data found.

Probably one more general point that we have shown in this thesis, is that learning algorithms can be successfully used to understand coherent control processes. This understanding been not only limited to a qualitative picture of the interaction, but it can also lead to a very deep and general model of the process at hand.

Appendix A

Details on some physical processes and conventions mentioned in the thesis

A.1 Rotating Wave Approximation

The Rotating Wave Approximation or RWA is on of the most widely used approximations in Physics and can be found in almost any modern quantum mechanics text book. Assume an oscillating electric field that couples two levels g and e through a simple dipole moment. The amplitude of the excited state obeys the time dependent Schrödinger equation,

$$i\hbar\frac{\partial}{\partial t}a_e(t) = -a_g(t)e^{i\omega_{eg}t}\frac{1}{2}\mu_{eg}\left(\varepsilon(t)e^{-\imath\omega_0 t} + c.c\right). \tag{A.1}$$

A closer look to the previous equations reveals that the second term (the c.c. one) oscillates much faster than the first. If the field is close to the atomic resonance, this term oscillates almost $2\times\omega_0$ faster ($omega_0 \approx \omega_{eg}/2$) which means that if we explicitly integrate in time, since the faster oscillating terms have more nodes as well, the contribution to the integral will be much smaller as their signs cancel out. This approximation is valid if the overall evolution of the amplitudes has a characteristic time longer than the optical frequencies. In our case, our laser has a wavelength of $\lambda_0 = 780$nm that corresponds to a period $T_{optical} \approx 2.5$fs. Since the field durations we typical obtain in the lab are of ~ 30 fs, this approximation is well justified.

A.2 Pulse area theorem

Although known through out the literature as a theorem, the derivations to be shown are far from been a strict mathematical proof. More details derivations can be found in [89]. Lets start with a two level Hamiltonian, after the RWA, that represents the interaction of a resonant pulsed field with levels $|1>$ and $|2>$,

$$H = \begin{pmatrix} 0 & \Omega(t) \\ \Omega(t) & 0 \end{pmatrix}, \tag{A.2}$$

with Ω being the Rabi frequencies.

The Schrödinger equation for the amplitudes is,

$$i\hbar\dot{a}_1 = \Omega(t)a_2(t) \tag{A.3}$$
$$i\hbar\dot{a}_2 = \Omega(t)a_1(t). \tag{A.4}$$

Introducing the variables,

$$b^+(t) = a_1(t) + a_2(t) \tag{A.5}$$
$$b(t) = a_1(t) - a_2(t), \tag{A.6}$$

we can uncouple Eqs. A.3 for these new variables. Integrating the equations and doing the inverse transformation we get for the amplitude a_2,

$$a_2(t) = \sin \int_{-\infty}^{t} \Omega(t')dt'/\hbar. \tag{A.7}$$

From the last equation we ca clearly see that if the area of the pulse $\int_{-\infty}^{\infty} \Omega(t)dt = \frac{\pi}{2}$, the population in the excited state at $a_2(t = \infty) = 1$.

A.3 Conventional STIRAP

Stimulated Raman Adiabatic Passage or STIRAP, is most known in a three level Λ system shown in Figure A.1.

The two fields are historically named Stokes for the field that couples levels $|2>$ and $|3>$ and pump for the field that couples levels $|1>$ (ground) and $|2>$. Assuming that both fields are in resonance with it's respective transition, $\Delta_S = 0$ and $\Delta_P = 0$. After applying the RWA and in the interaction picture,

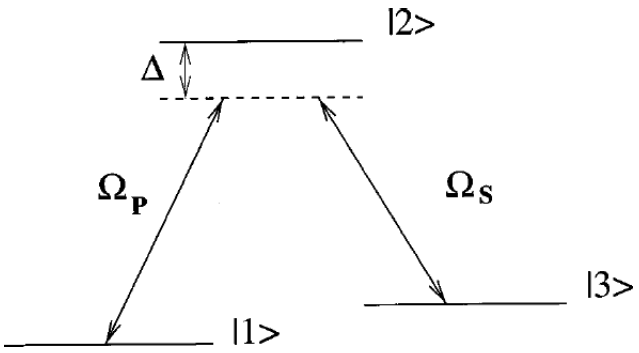

Figure A.1: Three level in a Λ configuration.

the Hamiltonian describing the interaction is,

$$\hat{\mathbf{H}} = \begin{pmatrix} 0 & \Omega_P & 0 \\ \Omega_P & 0 & \Omega_S \\ 0 & \Omega_S & 0 \end{pmatrix}, \tag{A.8}$$

where Ω_P and Ω_S are the Pump and Stokes Rabi frequencies (couplings) respectively. This Hamiltonian can be diagonalized, giving eigenvalues,

$$E^{0,\pm} = \hbar\omega^{0,\pm} = 0, \pm\frac{\hbar}{2}\Omega, \tag{A.9}$$

with,

$$\Omega = \sqrt{\Omega_P^2 + \Omega_S^2}, \tag{A.10}$$

and corresponding eigenvectors,

$$|g_0> = [\Omega_S|1> -\Omega_P|3>]\,\Omega^{-1} \tag{A.11}$$

$$|g_\pm> = \frac{1}{\sqrt{2}}\left\{[\Omega_P|1> +\Omega_S|3>]\,\Omega^{-1} \mp |2>\right\}. \tag{A.12}$$

Defining now the mixing angle Θ,

$$\Theta = \arctan\frac{\Omega_P}{\Omega_S}, \tag{A.13}$$

the dressed states eigenvectors above can be written as,

$$|g_0> = \sin\Theta|1> - \sin\Theta|3> \quad (A.14)$$

$$|g_\pm> = \sin\Theta|1> \mp \frac{1}{\sqrt{2}}|2> + \cos\Theta. \quad (A.15)$$

It should be noticed that there is no contribution to $|g_0>$ from level $|2>$. This is the foundation of STIRAP. If we have two fields that overlap enough (but not totally) in time, the character of $|g_0>$ will change *adiabatically* from that of level $|1>$ to level $|3>$. This means that the population *follows* the evolution of Ω_S and Ω_P. However, there is something we have overlooked which is that the ordering of the two pulses is counterintuitive in the sense that the Stokes pulse needs to come before the Pump one. This can be seen from the definition of the mixing angle Θ. Another way of looking at this is two think in terms of dressed states. First we dressed the states $|2>$ and $|3>$ with the Stokes pulse in such a way that they become degenerate. Then we apply the pump pulse from the ground state $|1>$ and the population follows directly to level $|3>$. A more detailed of this derivation can be found in [6].

Yet another approach to find STIRAP-like solutions was proposed by Malinovsky and Tannor [37]. The scheme here is very simple and it basically states that the condition to have the second state trapped (i.e., dark, frozen, paralyzed) is that the fields satisfy,

$$\frac{d|a_2(t)|^2}{dt} = 0. \quad (A.16)$$

Using the Schrödinger equation in the interaction picture to solve for the amplitudes $a_i(t)$, we arrive at,

$$\frac{d|a_2(t)|^2}{dt} = \Omega_P(t) Im\{a_2^*(t)a_1(t)\} + \Omega_S(t) Im\{a_2^*(t)a_3(t)\}. \quad (A.17)$$

In order for the population in the level $|2>$ to be trapped (i.e., remain unpopulated), the two contributions in the last equation need to cancel each other. We will make extensive use of this approach in Chapter 7.

A.4 Transformation of the A_{ki} coefficients to the LL' basis

The listing of atomic states properties, such as dipole moment couplings to other levels is usually done taking into account the fine structure. This means

that they are represented in the $\boldsymbol{J}$ basis since the quantum number for the total angular momentum $\boldsymbol{J}$ is a good quantum number, i.e., it commutes with the Hamiltonian. However, since we are so far detuned in all cases from the atomic resonances, the relevant dipole moments are those relating two states with orbital angular momentum l and l' without taking into account the sub-manifold of J and J' states. This means that we need to translate the listed values in [1] from the JJ' basis to the LL' basis. Let's assume that the transition from state $|a>$ with quantum numbers n, S, L, and J to state $|a'$ with quantum numbers n', S', L', and J'. For convenience we will use the transition strength, since it has a very simple relation to the dipole moments. The transition strength is defined as the square of the dipole moment,

$$S(nSL; n'S'L') = (2S+1)\|(nSL|er|n'S'L')\|^2, \tag{A.18}$$

for $L \rightarrow L'$ transitions and is defined as,

$$S(nSLJ; n'S'L'J') = (2S+1)\|(nSLJ|er|n'S'L'J')\|^2, \tag{A.19}$$

for $J \rightarrow J'$ transitions.

The relationship between S in both basis is,

$$S(nSLJ|er|n'S'L'J') = (2J+1)(2J'+1) \times \left\{ \begin{array}{ccc} L & J & S \\ J' & L' & 1 \end{array} \right\}^2 |(nl|er|n'l')|^2, \tag{A.20}$$

where the $\{\}$ are the Wigner $6j$ symbols. Since all but n are angular quantum momentum numbers, the transition strength also satisfies,

$$S(nSL|er|n'S'L') = \sum_{JJ'} S(nSLJ|er|n'S'L'J'). \tag{A.21}$$

Using now the properties of the Wigner $6j$ symbols and the intrinsic properties of angular quantum numbers,

$$\sum_{J'} = (2J'+1) \times \left\{ \begin{array}{ccc} L & J & S \\ J' & L' & 1 \end{array} \right\} = \frac{1}{2L+1} \tag{A.22}$$

$$\sum_{J} (2J+1)(2J'+1) = (2L+1)(2s+1). \tag{A.23}$$

With the aid of these relationships and combining Eq. A.21 and Eq. A.18, we can obtain the relation between the tabulated values of $S(nSLJ|er|n'S'L'J')$

and the dipole moment in the LL' basis for transitions between states with $L = 0$ and $L' = 1$,

$$(nl|er|n'l') = sqrt\frac{3}{2}S(nSLJ|er|n'S'L'J'). \tag{A.24}$$

The effect of polarization needs also to be taken into account [2]. Since we use a linearly polarized laser in our experiments, the dipole moment, after averaging over all directions of the projection of the polarization is,

$$(nl|er|n'l')_{LP} = \frac{1}{\sqrt{3}}(nl|er|n'l'), \tag{A.25}$$

which is the final value we use to calculate the tabulated values in Table 3.1.

Appendix B

Listing of selected code

All the simulations carried out in this thesis were done using Mathworks Matlab. For the data acquisition in the lab, National Instrument's LabView was used. Following are two sample programs used in the creation of some the figures in this thesis.

B.1 Using a simplified model

This code uses Matlab's built in `ode23`. The example listed here is used to calculate the $3s$, $4s$, and $7p$ populations as function of time for different intensities and delays between two gaussian pulses (see Fig. 4.5).

B.2 Sample code for Runge Kutta integration

This section lists more complicated code based on a home built fourth order Runge-Kutta algorithm. It is meant to be used in situations were analytical dependence with time is not known. For example, when using experimentally found electric fields (see Fig. 4.4), or for the local control algorithm used in Chapter 7 (see Fig. 7.2). This kind of algorithm was also used in the simulations of the yoked superfluorescence in Chapter 6 since we found that it is several times faster than the built in ODE (Ordinary Differential Equations) solver.

Program 1 Simple code version that calculates the population of the $3s$ and $4s$ levels after two gaussian pulses. Uses subroutine sodiumtom9.m

```
% Calculates population of the 3s,4s, and 7p states for two peaks delayed
% by DelayT, phase is controlled by sparam, sparam=0 is T.L.
% uses sodiumtom9.m

global sparam omega0Rad DeltaT Io DeltaI DelayT I2max;

sparam=0;
DeltaT=0.6; % Pulse duration
DeltaI=1;
to=-15;
tfinal=15;
s0=[1,0,];

DelayT=0.16; % Delay betweem two gauss pulses

chi2Io=1.0234E-02;
IoGauss = sqrt(pi*log(2))/(chi2Io*DeltaT*1e-12)*DeltaI;

omega0nm=777;
omega0Rad = 2*pi*3e8/(omega0nm*1e-9);

tt=to:0.01:tfinal;
tau=DeltaT/(2*sqrt(log(2)));

I1=exp(-tt.^2/(DeltaT/2/sqrt(log(2)))^2);
I2=exp(-(tt+DelayT/2/tau).^2)+exp(-(tt-DelayT/2/tau).^2);

Iratio=0.5;
I2max=max(I2);
Io=IoGauss*Iratio*max(I2);
DeltaI=Iratio*max(I2)*DeltaI;

options = odeset('RelTol',1e-6,'AbsTol',[1e-7]);
[t,s] = ode23('sodiumtom9',[to tfinal],s0,options);
figure
plot(t/tau,abs(s).^2);
titlestr= ['Two pulses no stark no 7p for s=', num2str(sparam), ' I_0 ='
 num2str(IoGauss), 'W/m^2, \Delta T ', num2str(DeltaT), ' Delay = ',num2str(DelayT
xlabel('Time [pulse duration]'); ylabel('Populatio');title(titlestr);
```

Program 2 Subroutine sodiumtom9.m used by na2peaks2.m. This is the Jacobian (right hand side) of the two level problem Eqs. 3.28.

```
function sp = sodiumtom9(t,s)
% Calculates population for a two gaussian pulse
%All units are in THz and ps and time is rescaled to pulse duration (50fs)
%chi0 chosen so that the integral of Rabi freq is pi/2
%no 7p state
%
global sparam omega0Rad DeltaT Io DeltaI DelayT I2max;

tau=DeltaT/(2*sqrt(log(2)));

delta_7p=(omega0Rad-2.41278E+15)/1e12*tau;
chi0=sqrt(pi)/(2*tau);
wgs=-32.3*0;
wes=18.3*0;
diffstark=wes-wgs;%8*2*pi;
%delta=(0/4)*diffstark;
delta=(2*omega0Rad - 4.8519e+015)/1e12*tau;
chi7p = 1.32707E-30/(2*1.05e-34)*sqrt(2*Io/(3e8*8.85e-12))/1e12;
phi0=-sparam*diffstark*tau*sqrt(pi)*DeltaI;
ponder=(2*Io/(3e8*8.85e-12))*(1.6e-19)^2/(4*(omega0Rad)^2*9.11e-31)/1.05e-34/1e12;
stark7p=0.25;
sp = -i*tau*[wgs*gg(t)*s(1)*DeltaI+exp(-i*phi0*(erf(t)+1)*0.5 +i*delta*t)
                                                    *chi0*gg(t)*s(2)*DeltaI,
   exp(i*phi0*(erf(t)+1)*0.5 - i*delta*t)*chi0*gg(t)*s(1)*DeltaI+
                                                    wes*gg(t)*s(2)*DeltaI];

function gg2=gg(t)
% t is already in units of tau, DelayT is not
global sparam omega0Rad DeltaT Io DeltaI DelayT I2max;
tau=DeltaT/(2*sqrt(log(2)));

gg2=exp(-(t+DelayT/2/tau).^2)+exp(-(t-DelayT/2/tau).^2);

gg2=gg2/I2max;
```

Program 3 napopanyfield4.m, calculates the population in time for an arbitrary field in time. The input format is setup to read from the output of experimentally generated FROGs.

```
% Calculates the population as a function of time of 3s, 4s, 7p for an
% arbitrary field in time.
% Reads file ek.dat generated by experimental frog. Adds a phase in frequency

%uses sodium_eq.m, array_filter.m

global omega0Rad Io DeltaI;
DeltaI=1;
omega0nm=772;
omega0Rad = 2*pi*3e8/(omega0nm*1e-9);
DeltaT=0.05;
%chi2Io=1.0234E-02;
%Io=sqrt(pi*log(2))/(chi2Io*DeltaT*1e-12)*DeltaI;
%Io=2.85473e15;

%reads the pulse shape in time

folder='E:\DATA\2005 09 05 Y\GA run 4\pulse with window\';

frogt=dlmread([folder 'ek.dat']);

toflip=input('Reverse time order [1=y/0=n]');
if toflip==1
frogt(:,2)=flipud(frogt(:,2)); % Uncomment this line for time reversal
frogt(:,3)=flipud(frogt(:,3));
end
% Calculates the experimental intensity
Energy=10*1e-6; % Energy in mJ
Area=63140*1e-12; % Area in um^2
Io=Energy/sum(frogt(:,2))/(abs((frogt(2,1)-frogt(1,1)))/1e15)/Area

Int0=frogt(:,2);
phi0=-frogt(:,3)-387*frogt(:,1).^2;
t0=frogt(:,1)/1e3; % convert from femtosecons to picoseconds
tresh=1000;
array_filter3
```

Program 4 napopanyfield4.m continuation

```
Field_envelope=Int1;
phi_t=phi1;
t_values=t1;

% RK fourth order begins here
tinit=min(t_values);
tfinal=max(t_values);
dtrk = (tfinal - tinit)/500/2;
trk = tinit:dtrk:tfinal;
stemp = zeros(3,1);
srk = zeros(3,length(trk)/2);
stemp(1)=1;

global trk g2 phi;
g2 = interp1(t_values, Field_envelope, trk,'spline');
phi = interp1(t_values, phi_t, trk,'spline');
srk(:,1)=stemp;
for n = 2:length(trk)-2
   k1 = dtrk*sodium_eq(n, stemp);
   k2 = dtrk*sodium_eq(n + 1, stemp + k1/2);
   k3 = dtrk*sodium_eq(n + 1, stemp + k2/2);
   k4 = dtrk*sodium_eq(n+2, stemp + k3);
   srk(:,round((n+2)/2)) = stemp + k1/6 + k2/3 + k3/3 + k4/6;
   stemp = srk(:,round((n+2)/2));
end

srk=srk';
trk2=tinit:dtrk*2:tfinal;

figure
plot(trk2, abs(srk).^2, t_values, Field_envelope, 'k')
titlestr= [folder, ' I_0 =' num2str(Io/1e12), 'TW/m^2,  \lambda_0 = ', num2str(ome
title(titlestr);
xlabel('Time (ps)');
ylabel('Population');
'Final population'
abs(srk(length(srk),2)).^2
abs(srk(length(srk),3)).^2

abs(srk(length(srk),2)).^2+abs(srk(length(srk),3)).^2
```

Program 5 sodium_eq7pDSS.m, contains the Jacobian (i.e., right hand side) of the Schrödinger equations for amplitudes in Eq. 3.47.

```
function sp = sodium_eq(n,s)
%All units are in THz and ps
%time is now the index, g2 is intensity profile, phi is phase,
% both are arrays

global omega0Rad Io DeltaI;
global trk g2 phi;
%tau=1/(2*sqrt(log(2)));

delta_7p=(omega0Rad-2.41278E+15)/1e12;
chi2Io=1.0234E-02;
chi0=chi2Io*Io/1e12;

% 18.3 and 32.3 are the values for the stark shift at 50fs,
% Io=2.883e15, it depends lineraly on intensity
% therefore this expression is correct
wgs=-32.3*Io/2.883e15;
wes=18.3*Io/2.883e15;
diffstark=wes-wgs;
w7psIo=0.001861535
w7ps=w7psIo*Io;

%delta=(0/4)*diffstark;
delta=(2*omega0Rad - 4.8519e+015)/1e12;
chi7p = 1.32707E-30/(2*1.05e-34)*sqrt(2*Io/(3e8*8.85e-12))/1e12;
%phi0=-diffstark*tau*sqrt(pi)*DeltaI;
%phi0=tau*sqrt(pi)*DeltaI;
phi0=1;
stark7p=w7psIo*Io/1e12;

valg2= g2(n);
valphi=phi(n);
t=trk(n);

sp = -i*[wgs*valg2*s(1)*DeltaI + exp(-i*valphi + i*delta*t)*chi0*valg2
                                                    *s(2)*DeltaI,
   exp(i*valphi - i*delta*t)*chi0*valg2*s(1)*DeltaI + wes*valg2*s(2)*DeltaI +
  chi7p*sqrt(valg2)*exp(-i*valphi*0.5+ i*delta_7p*t)*s(3)*sqrt(DeltaI),
   chi7p*sqrt(valg2)*exp(i*valphi*0.5- i*delta_7p*t)*s(2)*sqrt(DeltaI)
  +valg2*stark7p*DeltaI*s(3)];
```

Bibliography

[1] Yu. Ralchenko, F. C. Jou, D. E. Kelleher, A. E. Kramida, A. Musgrove, J. Reader, W. L. Wiese, and K. Olsen. Nist atomic spectra database (version 3.1.0). In *NIST Atomic Spectra Database, NIST Standard Reference Database Number 78*. National Institute of Standards and Technology, Gaithersburg MD, 20899, 2006. http://physics.nist.gov/PhysRefData/ASD/.

[2] I. I. Sobel'man. *An Introduction to the Theory of Atomic Spectra*. Pergamon Press, 1972.

[3] D.J. Tannor and S.A. Rice. Control of selectivity of chemical reaction via control of wave packet evolution. *J. Chem. Phys.*, 83:5013, 1985.

[4] Paul Brumer and Moshe Shapiro. Control of unimolecular reactions using coherent light. *Chem. Phys. Lett.*, 126(6):541–546, 1986.

[5] Warren S. Warren, Herschel Rabitz, and Mohammed Dahleh. Coherent control of quantum dynamics: The dream is alive. *Science*, 259:1581–1589, 1993.

[6] Paul W. Brumer and Moshe Shapiro. *Principles of the Quantum Control of Molecular Processes*. Wiley-Interscience, Hoboken, NJ, 2003.

[7] R.J. Levis, G.M. Menkir, and H. Rabitz. Selective bond dissociation and rearrangement with optimally tailored, strong-field laser pulses. *Science*, 292:709, 2001.

[8] R.S. Judson and H. Rabitz. Teaching lasers to control molecules. *Phys. Rev. Lett.*, 68:1500, 1992.

[9] D. Goswami. Optical pulse shaping approaches to coherent control. *Physics Reports*, 374:385, 2003.

[10] Doron Meshulach and Yaron Silberberg. Coherent quantum control of two-photon transitions by a femtosecond laser pulse. *Nature*, 396:239–242, 1998.

[11] Doron Meshulach and Yaron Silberberg. Coherent quantum control of multiphoton transitions by shaped ultrashort optical pulses. *Phys. Rev. A*, 60(2):1287–1292, 1999.

[12] A. Präkelt, M. Wollenhaupt, C. Sarpe-Tudoran, and T. Baumert. Phase control of a two-photon transition with shaped femtosecond laser-pulse sequences. *Phys. Rev. A*, 70:063407, 2004.

[13] Jon H. Shirley. Solution of the schrödinger equation with a hamiltonian periodic in time. *Phys. Rev.*, 138:B979, 1965.

[14] A. S. Davydov. *Quantum Mechanics*. Pergamon Press, 1976.

[15] F. H. M. Faisal. *Theory of Multiphoton Processes*. Plenum, New York, 1987.

[16] Nirit Dudovich, Barak Dayan, Sarah M. Gallagher-Faeder, and Yaron Silberberg. Transform-limited pulses are not optimal for resonant multiphoton transitions. *Phys. Rev. Lett.*, 86(1):000047, 2001.

[17] Andrey Gandman, Lev Chuntonov, Leonid Rybak, and Zohar Amitay. Coherent phase control of resonance-mediated (2+1) three-photon absorption. *Phys. Rev. A*, 75:031401, 2007.

[18] S. A. Hosseini and D. Goswami. Coherent control of multiphoton transitions with femtosecond pulse shaping. *Physics Review A.*, 64:033410, 2001.

[19] George N. Gibson. Extreme multiphoton coupling in molecular systems. *Phys. Rev. A.*, 67:043401, 2003.

[20] N. Dudovich, T. Polack, A. Pe'er, and Y. Silberberg. Simple route to strong-field coherent control. *Phys. Rev. Lett.*, 94:083002, 2005.

[21] C.E. Otis and P.M. Johnson. The ac stark effect in molecular multiphoton ionization spectroscopy. *Chem. Phys. Lett.*, 83:73, 1981.

[22] B. Girard, N. Billy, J. Vigué, and J.C. Lehmann. Evidence for a dynamical stark effect in co(a1?) two-photon excitation. *Chem. Phys. Lett.*, 102:168, 1983.

[23] W.M. Huo, K.P. Gross, and R.L. McKenzie. Optical stark effect in the two-photon spectrum of no. *Phys. Rev. Lett.*, 54:1012, 1985.

[24] B. Girard, G.O. Sitz, N. Billy, J. Vigué, and R.N. Zare. Polarization dependence of the ac stark effect in multiphoton transitions of diatomic molecules. *J. Chem. Phys.*, 97:26, 1992.

[25] R. R. Freeman, P. H. Bucksbaum, H. Milchberg, S. Darack, D. Schumacher, and M. E. Geusic. Above-threshold ionization with subpicosecond laser pulses. *Phys. Rev. Lett.*, 59:1092, 1987.

[26] B. Walker, M. Kaluza, B. Sheehy amd P. Agostini, and L. F. DiMauro. Observation of continuum-continuum autler-townes splitting. *Phys. Rev. Lett.*, 75:633, 1995.

[27] K Burnett, V. C. Reed, and P. L. Knight. Atoms in ultra-intense laser fields. *J. of Phys. B*, 26:561, 1993.

[28] R. B. López-Martens, T. W. Schmidt, and G. Roberts. Time-resolved stark effect in rapidly varying fields. *Appl. Phys. B*, 74:577, 2002.

[29] R. R. Jones. Interference effects in the multiphoton ionization of sodium. *Phys. Rev. Lett.*, 74(7):1091, 1995.

[30] R. R. Jones. Multiphoton ionization enhancement using two phase-coherent laser pulses. *Phys. Rev. Lett.*, 75(8):1491, 1995.

[31] C. Trallero-Herrero, D. Cardoza, T. C. Weinacht, and J. L. Cohen. Coherent control of strong field multiphoton absorption in the presence of dynamic stark shifts. *Phys. Rev. A*, 71:013423, 2005.

[32] Carlos Trallero-Herrero and Thomas C. Weinacht. Transition from weak to strong field coherent control. *Phys. Rev. A*, 75, 2007.

[33] C. Trallero-Herrero, J. L. Cohen, and T. C. Weinacht. Strong-field atomic phase matching. *Phys. Rev. Lett.*, 96:063603, 2006.

[34] Carlos A. Trallero-Herrero, Michael Spanner, and Thomas C. Weinacht. Understanding strong-field coherent control: Measuring single-atom versus collective dynamics. *Phys. Rev. A.*, 74:051403, 2006.

[35] Ronnie Kosloff, Audrey Dell Hammerich, and David Tannor. Excitation without demolition: Radiative excitation of ground-surface vibrations by impulsive stimulated raman scattering with damage control. *Physics Review Letters.*, 69:2172, 1992.

[36] Vladimir S. Malinovsky, Christoph Meier, and David Tannor. Optical paralysis in electronically congested systems: application to large amplitude vibrational motion of ground state na_2. *Chemical Physics.*, 221:67, 1997.

[37] Vladimir S. Malinovsky and David Tannor. Simple and robust extension of the stimulated raman adiabatic passage technique to n -level systems. *Physical Review A.*, 56:4929, 1997.

[38] M. Sugawara. General formulation of locally designed coherent control theory for quantum systems. *J. Chem. Phys.*, 118:6784, 2003.

[39] Patrick Henning Nürnberger and T. C. Weinacht. *Design and Construction of an Apparatus for the Neutral Dissociation and Ionization of Molecules in an Intense Laser Field.* PhD thesis, Stony Brook University, 2003.

[40] D. C. Cardoza and T. C. Weinacht. *Understanding and Applying Learning Control to Molecular Fragmentation.* PhD thesis, Stony Brook University, 2006.

[41] Daniel Arthur Flickinger and T. C. Weinacht. *Design and construction of system for ultrafast ultraviolet-blue pump-probe exposure of biological samples.* PhD thesis, Stony Brook University, 2005.

[42] Sterling Backus, Charles G. Durfee III, Margaret M. Murnane, and Henry C. Kapteyn. High power ultrafast lasers. *Review of Scientific Instruments*, 69(3):1207–1223, 1998.

[43] Rick Trebino, Kenneth W. DeLong, David N. Fittinghoff, John N. Sweetser, Marco A. Krumbugel, Bruce A. Richman, and Daniel J. Kane. Measuring ultrashort laser pulses in the time-frequency domain using frequency-resolved optical gating. *Rev. Sci. Instrum.*, 68(9):3277–3295, 1997.

[44] A. M. Weiner. Femtosecond optical pulse shaping and processing. *Prog. Quant. Electr.*, 19:161–237, 1995.

[45] J. X. Tull, M. A. Dugan, and W. S. Warren. High resolution, ultrafast laser pulse shaping and its applications. *Adv. Magn. Opt. Res.*, 20:1–50, 1997.

[46] D. Zeidler, S. Frey, K.-L. Kompa, D. Proch, and M. Motzkus. Evolutionary algorithms and their application to optimal control studies. *Phys. Rev. A*, 64:023420, 2001.

[47] T. C. Weinacht and P. H. Bucksbaum. Using feedback for coherent control of quantum systems. *J. Optics B*, 4:R35–R52, 2002.

[48] L. Davis. *A Handbook of Genetic Algorithms*. van Nostrand Reinhold, 1991.

[49] F. Langhojer, D. Cardoza, M. Baertschy, and T. C. Weinacht. Gaining mechanistic insight from closed loop learning control: The importance of basis in searching the phase space. *J. Chem. Phys.*, 122:01402, 2005.

[50] D. Cardoza, C. Trallero-Herrero, H. Rabitz, and T.C. Weinacht. Transformations to diagonal bases in closed-loop quantum learning control experiments. *J. Chem. Phys.*, 122:124306, 2005.

[51] Herschel A. Rabitz, Michael M. Hsieh, and Carey M. Rosenthal. Quantum optimally controlled transition landscapes. *Science*, 303:1998, 2004.

[52] G. M. Grover, T. P. Cotter, and G. F. Erickson. Structures of very high thermal conductance. *J. Appl. Phys. A.*, 35:1990, 1964.

[53] C. R. Vidal and J. Cooper. Heat-pipe oven: A new, well-defined metal vapor device for spectroscopic measurements. *J. Appl. Phys.*, 40:3370, 1969.

[54] Martha Bacal and Walter Reichelt. Metal apor confinement in vacuum. *Rev. Sci. Instrum.*, 45:769, 1974.

[55] S Demianiuk and K Kolwas. Dynamics of spontaneous growth of light-induced sodium droplets from the vapour phase. *J. Phys. B.*, 34:1651, 2001.

[56] A. N. Nesmeyanov. *Vapor Pressure of the Chemical Elements*. Elsevier, Amsterdam, 1963.

[57] Daniel A. Steck. Sodium d line data. Theoretical Division (T-8), MS B285, Los Alamos National Laboratory, Los Alamos, NM 87545, May 2000. http://steck.us/alkalidata.

[58] Constantine E. Theodosiou. Lifetimes of alkali-metalatom rydberg states. *Phys. Rev. A*, 30:2881, 1984.

[59] P. W. Miloni and J. H. Eberly. *Lasers*. Wiley, 1988.

[60] Dan Flickinger, Ryan Coffee, George Gibson, and Thomas Weinacht. Bichromatic, phase compensating interferometer based on prism pair compressors. *Appl. Opt.*, 45(24):6187, 2006.

[61] Robert W. Boyd. *Nonlinear Optics*. Academic Press, San Diego, 2002.

[62] H. J. Metcalf and R. van der Straten. *Laser Cooling and Trapping*. Springer, New York, 1999.

[63] P. Meystre and M. Sargent. *Elements of Quantum Optics 3rd Ed.* Springer-Verlag, 1991.

[64] D. Cardoza, M. Baertschy, and T. C. Weinacht. Understanding learning control of molecular fragmentation. *Chem. Phys. Lett.*, 411:311, 2005.

[65] D. Cardoza, M. Baertschy, and T. C. Weinacht. Interpreting closed-loop learning control of molecular fragmentation in terms of wave-packet dynamics and enhanced molecular ionization. *J. Chem. Phys.*, 123:074315, 2005.

[66] J.M. Geremia, E. Weiss, and H. Rabitz. Achieving the laboratory control of quantum dynamics phenomena using nonlinear functional maps. *Chem. Phys.*, 267:209, 2001.

[67] Michael Spanner and Paul Brumer. Mechanisms for the control of two-mode transient stimulated raman scattering in liquids. *Phys. Rev. A*, 73: 023809, 2006.

[68] Michael Spanner and Paul Brumer. Two-pulse control of raman scattering in liquid methanol: The dominance of classical nonlinear optical effects. *Phys. Rev. A*, 73:023810, 2006.

[69] A. Paul, R. A. Bartels, R. Tobey, H. Green, S. Weiman, I. P. Christov, M. M. Murnane, H. C. Kapteyn, and S. Backus. Quasi-phase-matched generation of coherent extreme-ultraviolet light. *Nature*, 421:51, 2003.

[70] B. J. Pearson and P. H. Bucksbaum. Control of raman lasing in the nonimpulsive regime. *Phys. Rev. Lett.*, 92:243003, 2004.

[71] G. Vogt, G. Krampert, P. Niklaus, P. Nuernberger, and G. Gerber. Optimal control of photoisomerization. *Phys. Rev. Lett.*, 94:068305, 2005.

[72] R. A. Bartels, S. Backus, S. R. Leone, M. M. Murnane, and H. C. Kapteyn. Impulsive stimulated raman scattering of molecular vibrations using nonlinear pulse shaping. *Chem. Phys. Lett.*, 374:326–333, 2003.

[73] Kunihito Hoki and Paul Brumer. Mechanisms in adaptive feedback control: Photoisomerization in a liquid. *Phys. Rev. Lett.*, 95:168305, 2005.

[74] Takashi Nakajima. Influence of ac stark shifts on the propagation of phase-controlled lasers in a two level medium. *J. Opt. Soc. Am. B*, 19: 261, 2002.

[75] M. G. Raymer and J. Mostowski. Stimulated raman scattering: Unified treatment of spontaneous initiation and spatial propagation. *Phys. Rev. A*, 24:1980, 1981.

[76] M. Lewenstein. Fluctuations in the nonlinear regime of stimulated Raman scattering. *Z. Phys. B: Condens. Matter*.

[77] Fritz Haake, Joseph Haus, Haraid King, and Guntram Schröder. Delay-time statistics and inhomogeneous line broadening in superfluorescence. *Phys. Rev. Lett.*, 45:558, 1980.

[78] G. Gibson, T. S. Luk, A. McPherson, and C. K. Rhodes. Generation of coherent extreme-ultraviolet and infrared radiation using six-wave mixing in argon. *Phys. Rev. A.*, 43:000371, 1991.

[79] R. Bonifacio and L. A. Lugiato. Cooperative radiation processes in two-level systems: Superfluorescence. *Phys. Rev. A*, 11(5):1507, 1975.

[80] M. F. H. Schuurmans and D. Polder. Superfluorescence and amplified spontaneous emission: A unified theory. *Phys. Lett. A*, 72:306, 1979.

[81] Michelle S. Malcuit, Jeffery J. Maki, David J. Simkin, and Robert W. Boyd. Transition from superfluorescence to amplified spontaneous emission. *Phys. Rev. Lett.*, 59:1189, 1987.

[82] J. H. Brownell, X. Lu, and S.R. Hartmann. Yoked superfluorescence. *Phys. Rev. Lett.*, 75:3265, 1995.

[83] D. Cardoza, F. Langhojer, C. Trallero-Herrero, O. L. A. Monti, and T. C. Weinacht. Changing pulse-shape basis for molecular learning control. *Phys. Rev. A*, 70:053406, 2004.

[84] C. Hubrich and F. Stuhl. Ultraviolet absorption of some halogenated methanes and ethanes of atmospheric interest. *J. Photochem.*, 12:93, 1980.

[85] K.W.D. Ledingham and R. P. Singhal. *International Journal of Mass Spectrometry and Ion Processes*, 163:149, 1997.

[86] J. R. Kuklinski, U. Gaubatz, F. T. Hioe, and K. Bergmann. Adiabatic population transfer in a three-level system driven by delayed laser pulses. *Phys. Rev. A.*, 40:6741, 1989.

[87] K. Bergmann, H. Theuer, and B. W. Shore. Coherent population transfer among quantum states of atoms and molecules. *Rev. Mod. Phys.*, 70:1003, 1998.

[88] David Tannor. *Introduction to Quantum Mechanics: A Time-Dependent Perspective*. University Science Books, Herndon, VA, 2005.

[89] L. Allen and J. H. Eberly. *Optical Resonance and Two-Level Atoms*. Dover, New York, 1987.